Plane Front Stability and Cellular Solidification in Fiber Reinforced Aluminum-Copper Alloys

by

Nancy Frier Dean

B.S.E., Metallurgical Engineering, University of Michigan, 1985

Submitted to the Department of
Materials Science and Engineering
in Partial Fulfillment of the Requirements for the Degree of

DOCTOR OF PHILOSOPHY

at the

MASSACHUSETTS INSTITUTE OF TECHNOLOGY

June 1992

Signature of author_____
Department of Materials Science and Engineering
May 1, 1992

Certified by_____
Andreas Mortensen
Thesis Supervisor

Certified by_____
Merton C. Flemings
Thesis Supervisor

Accepted by_____
Linn W. Hobbs, Chairman
Departmental Committee on Graduate Students
Department of Materials Science and Engineering

Plane Front Stability and Cellular Solidification in Fiber Reinforced Aluminum-Copper Alloys

by

Nancy Frier Dean

Abstract

An investigation is made of the transition from plane front to cellular solidification, and of cellular solidification, in aluminum-4.5 wt% copper and aluminum-1.0 wt% copper alloys reinforced with parallel, continuous, closely spaced alumina fibers.

Specimens were designed to have a central reinforced region surrounded by unreinforced metal of the composite matrix composition. Each was produced by pressure infiltration, subsequently remelted and directionally solidified in a vertical Bridgman furnace and quenched to reveal the liquid-solid metal interface. Both unreinforced and composite sections were characterized to determine solidification front morphology and degree of microsegregation.

Measured cell tip undercoolings in the unreinforced metal agree with the Bower-Brody-Flemings model. Microsegregation during solidification of cylindrically symmetric cells is predicted by a finite difference model, assuming Bower-Brody-Flemings cell tip undercoolings. Model predictions agree with experimental measurements of fraction eutectic in the unreinforced metal. The matrix of the solid composite is essentially free of microsegregation for all solidification conditions investigated, also in agreement with theory.

The shape of the liquid/solid metal interface near the fibers indicates a lower fiber/liquid metal interfacial energy than fiber/solid metal interfacial energy. In the composite, a pseudo-planar to cellular morphological transition takes place for solidification conditions past the onset of plane front instability in the unreinforced metal. The location of this transition agrees with a direct application of linear morphological stability theory for cells geometrically constrained to grow within narrow fiber interstices. This indicates the enhanced stability of planar fronts in the composite results from the influence of finite liquid/solid metal interfacial energy. Comparison of cell heights with predictions for unreinforced cells indicates that cell tip undercooling is increased in the composite.

Thesis Supervisor: Prof. Andreas Mortensen
Title: Associate Professor of Metallurgy

Thesis Supervisor: Prof. Merton C. Flemings
Title: Toyota Professor of Materials Processing
Head, Department of Materials Science and Engineering

Table of Contents

List of Figures

List of Tables

Acknowledgements

I would like to thank the many people who have contributed in one way or another to the successful completion of this work.

First of all, I wish to express my gratitude to my advisors, Professor Andreas Mortensen and Professor Merton Flemings, who gave generously of their time, offering much guidance and support

I also thank the other members of my thesis committee: Professor Ken Russell both for his support and help at the beginning of my studies, and for being there at the end when I needed his help. Professor Carl Thompson's many useful comments and suggestions were very helpful.

My office mates: Tami Jonas, who always had time to listen and lend suggestions or a sympathetic ear, Toshihiko Koseki, who offered keen insight and excellent suggestions during our many discussions, and Jared Sommer all enhanced my stay on both personal and technical levels.

Professor Heather Lechtman's support and encouragement, particularly during this last year, were comforting and very much appreciated.

I would also like to thank Allison Hubel for her help and friendship in the lab, as well as for her useful suggestions to improve this thesis.

I also appreciate the assistance of all the members of the Metal Matrix Composites and Solidification groups. Jackie Isaacs, David Dunand, Robert Calhoun, Tom Fitzgerald and Tom Piccone assisted me with various aspects of this work. I would particularly like to thank Liz Earhart for helping me with the image analysis and for showing extreme patience when I needed "just one more file" from the computer she was using.

I would also like to thank my sister, Karen, who always seemed to know the right time to call and lift my spirits, and my parents, Judy and Bruce, for their continual support and encouragement.

Last, but certainly not least, I would like to thank my husband, Mike. His unfailing support, love, faith, help and encouragement (not to mention computer cycles) were instrumental to the completion of this thesis.

Nancy F. Dean

Cambridge, MA

February, 1992

Chapter 1

Introduction

As technical and commercial interest in metal matrix composites increases, much attention is being paid to casting as a primary composite fabrication technique. Liquid metal fabrication methods are attractive as they offer low cost and adaptability to existing commercial metals processing practices. As in unreinforced materials, solidification plays a major role in determining the microstructure, and hence the properties, of a cast metal matrix composite. Optimizing those properties requires that relationships between solidification conditions and matrix microstructure be known.

In metal matrix composites, the matrix must solidify within the geometric constraints imposed by an inert and, often, immobile reinforcing phase. The reinforcement spacing therefore effectively places an upper limit on the microstructural scale of the matrix. Microstructural features of cast metals are often significantly larger than typical reinforcement interstices. In these cases a reinforcement modifies the matrix solidification behavior, making direct application of conventional microstructure-processing relationships inappropriate for solidification of reinforced materials.

The presence of a fiber reinforcement has been shown to alter matrix microstructure in a dendritically solidified metal matrix composite. Two other principal solidification modes, planar and cellular solidification, have received comparatively less attention in the context of metal matrix composites and are the focus of this thesis. More specifically, this work places focus on the planar to cellular transition, on cell morphology and on microsegregation, in a dilute binary alloy geometrically constrained by

parallel continuous fibers. By directionally solidifying the composites parallel to the fibers, steady state solidification conditions similar to ones used in investigations of plane front and cellular solidification of unreinforced alloys are obtained.

The next section provides a brief review of literature on the planar to cellular solidification transition and on cellular solidification in unreinforced metals, followed by a summary of the work to date pertinent to plane front and cellular solidification in metal matrix composites with an immobile reinforcement. The theory section addresses plane front stability and cellular solidification in fiber composites. Experimental procedures are then outlined, and results are presented, followed by a discussion of experimental results in light of theory.

Chapter 2

Literature Survey

2.1 The Planar to Cellular Transition

Plane front solidification of a binary alloy is easily described by simple analytical solutions for the thermal and solutal fields in front of and behind the liquid-solid interface. This solidification mode is, however, seldom observed in practice with non-dilute metal alloys, because the planar front configuration is often unstable against perturbations. At small deviations from growth conditions yielding a stable plane front, cells, which are regular and smooth corrugations of the solidification front, develop. There exist well defined criteria for predicting this transition, and to a lesser extent the periodicity of a nonplanar interface. An excellent review of the planar to cellular transition and cellular solidification is given by Coriell, McFadden and Sekerka [1].

2.1.1 Constitutional Supercooling

It has been known for many years that as the growth rate, V, of a dilute binary alloy is increased, the liquid-solid interface morphology changes from a planar front to cells and finally to dendrites [2-4]. This phenomenon was first explained qualitatively by Rutter and Chalmers [5] and then quantitatively by Tiller, et al, [6] with the constitutional supercooling criterion, enabling the prediction of the planar to cellular transition during directional solidification of a dilute alloy.

When a dilute alloy freezes, solute rejected at the liquid-solid interface (which occurs when the solute concentration in the solid is lower than that in

the liquid) must be removed by diffusion into the liquid. The resulting concentration gradient presents a gradient in freezing point, or liquidus temperature. At all points in front of an interface, the local temperature, T, must be greater than the liquidus temperature, T_L, for that interface to be stable. This condition is satisfied when the temperature gradient, G_L, in the liquid is greater than the liquidus, or freezing point, gradient at the interface:

$$G_L \geq m_L G_C \,. \tag{2.1}$$

Here m_L is the phase diagram liquidus slope and G_C is the concentration gradient at the liquid-solid interface, equal to:

$$G_C = \frac{\partial C_L}{\partial z} = -\frac{V}{D_L} C_0 \frac{(1-k)}{k} \,, \tag{2.2}$$

for a planar interface, where V is the growth velocity, D_L the liquid solute diffusivity, C_0 is the average composition and k is the equilibrium solute partition ratio. Thus the constitutional supercooling criterion for stability of a planar interface is:

$$G_L \geq \frac{m_L V C_0 (k-1)}{D_L k} \,. \tag{2.3}$$

2.1.2 Linear Morphological Stability Analyses

Constitutional supercooling predicts which phase, solid or liquid, is thermodynamically stable in front of the interface. Morphological stability analyses can provide a more rigorous approach to the breakdown of a planar

front by taking into account additional phenomena, such as interfacial energy and heat transfer.

Mullins and Sekerka [7] and Voronkov [8] were the first to perform a linear stability analysis of plane front solidification. Mullins and Sekerka analyzed temperature distributions in both liquid and solid as well as the solute distribution in the liquid, using steady state fields. Conservation of mass and heat, continuity of temperature and thermodynamic equilibrium at the interface were assumed. The major departure from the constitutional supercooling criterion was the use of the Gibbs-Thomson equation to determine the temperature at the interface. This equation,

$$T = T_M + m_L C_0 + \Gamma \kappa \ , \tag{2.4}$$

where T_M is the melting point of pure solvent, Γ is the Gibbs-Thomson or capillary coefficient and κ is the radius of curvature of the interface, incorporates the effects of curvature in determining the interface temperature. Kinetic undercooling was ignored.

Mullins and Sekerka assumed an arbitrary sinusoidal perturbation of a flat interface, to determine which wavelengths, if any, can grow. Their result is an expression for the growth rate of a sinusoidal perturbation with wave number ω normalized by the perturbation's height δ:

$$\frac{\dot{\delta}}{\delta} = \frac{V\omega \{ -2T_M\Gamma\omega^2 \ (\omega^* - \frac{V}{D_L} p) - (G_s + G_l) (\omega^* - \frac{V}{D_L} p) + 2m_L G_c \ (\omega^* - \frac{V}{D_L}) \}}{(G_s - G_l) (\omega^* - \frac{V}{D_L} p) + 2\omega m_L G_c} \ . \tag{2.5}$$

Here p = 1 - k, $\mathcal{G}_S$ and $\mathcal{G}_l$ are conductivity-weighted thermal gradients defined by:

$$\mathcal{G}_S = \frac{2K_S}{K_S + K_L} G_S \ , \tag{2.6}$$

and

$$\mathcal{G}_L = \frac{2K_L}{K_S + K_L} G_L \ , \tag{2.7}$$

K_S and K_L are the thermal conductivities of the solid and liquid, respectively, and

$$\omega^* = \frac{V}{2D_L} + \left\{ \left(\frac{V}{2D_l} \right)^2 + \omega^2 \right\}^{\frac{1}{2}} \ . \tag{2.8}$$

The plane front is stable when perturbations of all wavelengths decay, i.e., when $\dot{\delta}/\delta < 0$ for all ω.

Direct determination of the stability of a planar interface through the use of equation 2.5 involves the solution of a cubic equation in ω. Sekerka [9] facilitated this task by developing a stability function, S, which allows the Mullins-Sekerka stability criterion to be explicitly evaluated. S is a function of the partition ratio, k and a dimensionless parameter, A, given by:

$$A = \frac{k^2}{1-k} \frac{\Gamma V}{D_L} \frac{T_M V}{(-m_L)C_0} \ . \tag{2.9}$$

Values for S are tabulated or presented graphically, as shown in Figure 2.1, to be used in a revised plane front stability criterion:

$$\frac{G^*}{S} \geq m_L G_C \ , \qquad (2.10)$$

where G* is the effective, conductivity weighted thermal gradient:

$$G^* = \frac{(G_S + G_l)}{2} = \frac{2K_L}{K_S + K_L}\left(G_L + \frac{L}{2K_L} V\right) , \qquad (2.11)$$

and L is the latent heat of fusion.

Inclusion of surface energy and consideration of a conductivity-weighted thermal gradient in the linear stability criterion lead to the possibility that an interface may be constitutionally supercooled, yet still solidify with a stable planar front. The stabilizing effect of the surface energy manifests itself in equation 2.10 by a deviation of S from unity. This deviation is typically small. If the thermal conductivity of the solid and liquid differ significantly, or the latent heat of fusion, L, is large, the ratio G^*/G_L will depart appreciably from unity, resulting in measurable differences between the constitutional supercooling and morphological stability criteria.

When a plane front is unstable, it is not unstable with respect to all perturbation wavelengths. Short wavelengths are stabilized by capillary effects, while long wavelengths are stabilized by the long lateral diffusion paths relative to the plane front diffusion boundary layer. This is illustrated in Figure 2.2 which shows a series of $\dot{\delta}/\delta$ plots for increasing growth velocity, past the critical value for plane front instability. The wavelength spectrum of destabilizing perturbations initially increases as the interface velocity increases past its critical value. For sufficiently high velocities, this range decreases again, leading to Absolute Stability, where all perturbations are again stabilized. The growth rates for absolute stability are many orders of

magnitude larger than those for initial breakdown of a plane front due to constitutional supercooling, and are typically encountered only in rapid solidification processes.

One of the more questionable assumptions in the Mullins-Sekerka analysis is its use of a steady state diffusion equation to examine the time dependent amplitude of a perturbation. Sekerka [10] and Delves [11] reworked the problem, including a time-dependent diffusion equation to prove that the influence of time dependent terms is weak near the critical point.

Coriell and co-workers have extended the linear stability analysis to include a wider range of conditions, such as consideration of the effect of convective flow in the liquid [12], the effect of concentration dependence of liquidus slope, m_L and partition ratio k [13], multicomponent alloys [14], buoyancy effects [15], electric field effects [16] and anisotropic thermal conductivity [17]. Coriell and Sekerka considered the influence of curvature at a grain boundary on morphological stability . Performing a stability analysis on a pure material [18], and a binary alloy [19] they found that curvature induced at a grain boundary did not alter the stability criterion, only provided an initial site for perturbations to develop.

Other authors have examined the effects of lateral heat transport in thin samples [20], heat of mixing [21] and the Soret effect [22] on linear morphological stability theory. Caroli, Caroli and Roulet [23] performed a linear stability analysis to determine the effect of the contact angle, θ, at the junction of a confining wall and the liquid-solid interface, on stability of a planar front in thin samples. Contact angles not equal to 90° induce interface curvature in the thickness direction of these samples. Considering small deviations from 90° in θ, they found that the critical velocity at the onset of instability is dependent upon sample thickness, being lower for thin samples

than a three dimensionally infinite system. The geometry analyzed, that of a liquid confined to a narrow gap between two flat plates, where there is no upper limit to the perturbation wavelength along the width, is commonly used in directional solidification experiments involving transparent organics.

2.1.3 Experimental Confirmation of Stability Criteria

Experimental measurements of the onset of plane front instability have been reviewed by several authors [1, 24, 25]. Many studies have shown general agreement between experiment and the constitutional supercooling criterion, for example [26-29]. Typically these experiments involved decanting liquid from a solidifying sample, thereby interrupting solidification and allowing examination of the sample's free surface for corrugations. Whether a sample had a planar morphology was often a subjective judgement because a thin film of liquid would adhere to the interface, obscuring small or shallow features. Since precise measurements were beyond the scope of these experiments, the approach usually taken was to deduce a liquid solute diffusivity, D_L by assuming the constitutional supercooling criteria is valid, and taking a reasonable value substantiate the constitutional supercooling criterion. Within this framework, these studies showed a good qualitative agreement between predicted and observed breakdown of the planar front.

Because constitutional supercooling and morphological stability differ little at low growth velocities for most materials, uncertainty in thermophysical properties of materials has precluded a distinction from being made between the two criteria in the interpretation of data from all but a small number of experimental studies.

Sato, Ohiro and coworkers performed such a series of experiments [30-32] on aluminum alloys, measuring in separate experiments all thermophysical

properties necessary to test linear stability theory. For these alloys, the ratio of the effective temperature gradient to the liquid temperature gradient, $G^*/ G_L \approx 0.6$, large enough for the two stability criteria to differ noticeably. For Al-Cr alloys, scatter in their data is too large to distinguish between linear stability theory and constitutional supercooling. For Al-Zn, Al-Ti and Al-Cu alloys the conditions for the onset of instability are in better agreement with Mullins and Sekerka's stability theory. The wavenumber of perturbations varied significantly, and does not correspond to the predicted critical wavenumber at the onset of instability, ω_c. Jamgotchian, Billia and Capella [33], measured the onset of instability during Bridgman solidification of dilute Bi-Sb alloys. In these experiments, capillarity exerted a significant stabilizing influence, with S ranging from 0.61 to 0.86. Their results agree well with the linear stability criterion.

Other authors have studied the influence of spatial constraints on stability of plane front solidification. Ayers and Schaefer [34] examined the morphological stability at a grain boundary groove in high purity succinonitrile. A parametric fit of their data yielded a value for the solid liquid surface energy that was approximately two thirds of the accepted value. This discrepancy was attributed to linear theory inadequately treating the contact angle observed in the experiments. deCheveigné, Guthman and LeBrun [35], in a series of solidification experiments with CBr_4, show that the critical growth rate for the onset of instability decreases with the thickness of the sample. In these experiments, the liquid exists between two parallel plates, so that there is no constraint on the perturbation wavelength in the transverse direction. Their measurement of this meniscus effect are in reasonable agreement with the theoretical work of Caroli, et al [23].

2.2 Cellular Solidification

Linear stability theory predicts the critical conditions for the onset of plane front instability and can provide some insight on wavelength selection for conditions just beyond the onset of instability. However, since perturbations are expected to grow exponentially, nonlinear terms quickly gain significance and must be incorporated in analyses of non-planar interfaces.

Nonlinear stability work on classes of hydrodynamic problems, such as Bénard convection, can be adapted to analyze cellular solidification. First to do this were Wollkind and Segel [36] with a two dimensional, weakly nonlinear analysis, in which the wavenumber of a perturbation was fixed, and perturbation growth was examined near the critical point. Their major result was to show that the interface could be unstable to finite amplitude disturbances when linear theory predicts stability to infinitesimal disturbances. For a dilute tin-lead alloy, a cell spacing of 57μm was computed and compared to observed cell diameters of 60 to 90μm [37]. While this analysis does give an approximate estimate of the cell spacing, it cannot accurately predict cellular spacings at steady state.

Nonlinear stability analysis has recently been extended to consider other physical effects. Caroli, Caroli and Roulet [38] include solute diffusion in the solid, McFadden et al [39] include surface tension anisotropy in a three dimensional weakly nonlinear analysis, and Young, Davis and Brattkus [40] predict that cells may grow tilted with respect to the growth direction due to anisotropic interface kinetics.

If interested only in the dynamics of the interface or the interface shape, the full free boundary solidification problem can be mapped or projected into one involving only the interface shape using Green's functions, to yield an integro-differential equation for the interface displacement from the planar

state. The number of variables in the problem is then significantly reduced, but the resulting equation is still analytically intractable. Approximate solutions are obtained by assuming small interface perturbations and by including a small number of terms in the Fourier expansion of the interface shape. The first researchers to take this approach were Langer and Turski [41], examining a stationary, isothermal, planar liquid-solid interface subject to instabilities caused by solute gradients. This type of analysis has been extended to many simplified solidification models, such as a symmetric model (which neglects latent heat, and assumes thermal and solutal diffusivities are the same in both phases) with constant miscibility gap [42] and a one-sided model (which allows thermal diffusivities to vary, but neglects solute diffusion in the solid) [43]. A benefit of this type of analysis is that solutions can be tested for stability with respect to wavelength modulation. Perturbations unstable to wavelength modulation may be eliminated from the range of possible equilibrium wavelengths.

Dee, using a symmetric model, [44] developed an expression for critical velocity at the onset of instability considering a finite system size. By incorporating wavelength limitations, but not contact angle, or meniscus effects, the critical velocity, V_c, for the onset of instability was predicted to increase dramatically when the system size, L, is smaller than 10 diffusion lengths (which equal D/V, D being the diffusion coefficient), as shown in Figure 2.3.

McFadden and Coriell [45] use finite-difference methods to examine a steady state two-dimensional model in which equal thermal properties in the liquid and solid are assumed. Ungar and Brown use finite element techniques combined with curve tracking to consider development of two dimensional cells from an initially planar interface, using a one-sided model

[46]. Ungar and Brown restrict composition or velocity so that the cell groove depth is similar in size to the cell spacing, and track families of solutions for a single perturbation wavelength, obtaining results in agreement with those of Wollkind and Segel. Ungar and Brown's earlier calculations are extended to examine the effect of grain boundary grooves [47], the effect of heat transfer and solute diffusivity [48], and the formation of deep cells [49] . Considering curvature induced at a grain boundary junction in a binary alloy and grain boundary angles marginally greater than 90°, the interface deflection increases dramatically, a pseudo planar-cellular transition, at a temperature gradient greater than the critical gradient in bulk materials. For larger contact angles, a continuous series of solutions from shallow to deep cells was found, starting again at higher temperature gradients, which signifies a destabilizing effect on a planar solidification front. Ungar, Bennett and Brown [48] also show interface deflection is retarded by higher values of the Stefan number, $S_t = L/\rho\, c_p\, T_M$, where L is the latent heat of fusion, ρ is the density, c_p is the specific heat and T_M is the melting point.

McCartney and Hunt use a finite difference method to treat steady state growth of a single cell within a cellular array [50]. Neglecting solute diffusion in the solid, they solve heat and solute flow equations and conservation equations at the interface, including the effects of curvature and interface kinetics on the equilibrium interface temperature. They obtain self-consistent solutions for a range of imposed cell widths, and examine the effect of imposed cell width, kinetic and curvature undercooling constants on tip curvature, tip concentration and tip temperature. The kinetic undercooling constant has little effect on stabilization of a growing cell, while the curvature undercooling constant affects minimum undercooling. Decreasing cell radii to approximately half experimentally observed values causes cell tip

undercoolings to increase only slightly. No attempt is made to analyze time-dependent cell growth, however, they propose that natural cell spacings fall between those which give minimum tip undercooling and the largest spacing for which self-consistent shapes are found.

Hunt and McCartney [51 , 52] and Hunt [53] extend their earlier analysis to include solid state diffusion. Again, they find self consistent solutions for a range of wavelengths. As cell spacings become larger, the cell tips flatten, indicating tip splitting should occur. The lowest stable wavelength, determined by the lack of a convergent interface shape, is unchanged from their previous analysis.

Several simpler models have been proposed for the prediction of the temperature and composition at the tip of cells. Bower, Brody and Flemings [54] propose that the main cause for cell tip undercooling is the longitudinal solute gradient in the intercellular liquid that results from local equilibrium at the liquid/solid interface in a temperature gradient. The liquid tip composition is then:

$$C_t = C_0 (1 - a) \ , \tag{2.12}$$

and the tip temperature is:

$$T_t = T_M + m_L C_0 (1 - a) \ . \tag{2.13}$$

where

$$a = \frac{D_L G_L}{m_L V C_0} \ . \tag{2.14}$$

Several authors have, since, proposed more complex calculations of cell tip temperature based on the assumption that the solute distribution near the cell tips can be derived from models for growth of a sphere or a paraboloidal needle into an infinite liquid bath [55 , 56]. These, and the results of numerical models by McCartney and Hunt [51-53] all predict values for tip temperature and composition that are close to those predicted by the Bower-Brody-Flemings model in the cellular growth range. Theoretical predictions agree with experimental measurements of tip temperatures [57-59].

2.3 Microsegregation

In alloys which are nominally single phase, concentration gradients and nonequilibrium second phases may result from a low rate of diffusion in the solid state during solidification. Termed microsegregation, this can have a significant impact on the mechanical properties of a material. The first quantitatively description of microsegregation was the nonequilibrium lever rule, or Scheil equation [60-62]:

$$C_S^* = k\, C_0\, (1 - f_S)^{(k-1)} \quad , \tag{2.15}$$

where C_S^* is the interface composition of the solid (in wt percent) when the weight fraction solid is f_S. Assumptions in developing this equation include constant partition ratio, complete solute diffusion in the liquid, no solute diffusion in the solid, no undercooling at the cell tips and no convection.

Bower, Brody and Flemings [54] (BBF) derived a local solute redistribution equation for cellular solidification based on their analysis of cell tip undercooling and assuming no diffusion in the solid:

$$C_s^* = k C_0 \left\{ \frac{a}{k-1} + \left(1 - \frac{ak}{k-1}\right) (1 - f_s)^{(k-1)} \right\}, \qquad (2.16)$$

Flemings et al. [63 , 64] also present a local solute redistribution equation in an analysis of macrosegregation induced by flow of solute rich liquid to feed solidification shrinkage. Other researchers have allowed for the effects of limited liquid diffusion [6], or convection on local solute redistribution.

Microsegregation predicted by models described above, which assume no solid state diffusion, is generally greater than found experimentally. Using a finite difference analysis of solute redistribution, Brody and Flemings [65] addressed the effect of back-diffusion in the solid for dendritic solidification. In this, and in later models [66 , 67], parabolic or constant dendrite thickening rates were assumed. Kirkwood and Evans [68] first treated the problem as a free boundary one by specifying the rate of heat removal during solidification for plate dendrites.

Brody and Flemings [65] also developed approximate solute redistribution equations which include the effect of solid state diffusion for linear and parabolic thickening of the dendrite. These expressions are upper bounds on the extent of diffusion and are explicitely acknowledged to be incorrect unless solid state diffusion is very limited. Clyne and Kurz [69] have proposed a modification of the Brody-Flemings equation, which is quantitatively correct in the limits but, as Kirkwood [70] points out, is essentially a mathematical manipulation with no physical basis. Kobayashi [71] proved that Clyne and Kurz's model overestimates the extent of diffusion in the solid and derived an exact analytical solution for solidification with parabolic growth, given by an infinite series expansion. However, the number of expansion terms necessary to obtain an accurate solution is extremely large when either the

partition ratio, k or the diffusion Fourier number, $\alpha = D_s\, t\, \lambda^{-2}$ (where D_s is the solid solute diffusivity, t is local solidification time and λ is the distance over which diffusion occurs) is small.

The desirability of an analytical expression for anything more than an approximation of the degree of microsegregation is questionable, however, as many thermophysical parameters, in particular D_s, are strong functions of temperature. In comparison, finite difference methods, as used by Brody and Flemings and later by others [66-68 , 70, 72-74] allow temperature dependences to be easily incorporated.

If, at the other extreme, solute diffusion in the solid is complete, analytical solutions can also be proposed. In particular, when there is no tip undercooling, solidification follows the phase diagram according to the equilibrium lever rule. The solid composition C_S^* is then given by:

$$C_S^* = \frac{k\, C_0}{1 - f_s\,(1-k)} \tag{2.17}$$

2.4 Solidification With Geometric Constraints

Solidification with geometric constraints, in particular solidification within a metal matrix composite, has recently been reviewed by Mortensen [75] and Mortensen and Jin [76]. When the reinforcement is immobile, as is the case with a fiber or reticular foam-reinforced metal, particle pushing effects are absent, and the reinforcement essentially constitutes a geometric constraint on the growing solid metal.

A small system size can significantly influence the liquid-solid interface morphology. Aspects of this problem have been addressed theoretically for plane front and cellular growth by Caroli, Caroli and Roulet [23], Coriell and

Sekerka [18], Ungar and Brown [47], Dee [44] and with small deviations from unrestricted cell spacings by McCartney and Hunt [50 , 52], as outlined above.

Sekhar and Trivedi [77] and Trivedi, Han and Sekhar [78] examine solidification of a dilute succinonitrile-acetone alloy in narrow channels and observe that the liquid-solid interface temperature is somewhat lower in a small channel when solidification modes are the same in large and small channels, and that the interface morphology changes from dendritic to cellular to a nearly planar front as channel width decreases They note that curvature induced by the contact angle, θ, at the liquid-solid-wall junction prohibits a true planar front from forming, and may enhance the stability of a cellular interface for very narrow channels. To illustrate these effects, Trivedi, Han and Sekhar [78], present an interface morphology map for interface velocity V and relative channel size d/λ where d is channel width and λ the primary dendrite arm spacing, as shown in Figure 2.4. When $d/\lambda = 1$, the channel wall replaces a zero flux boundary between cells or dendrites, and the interface exhibits its unconstrained morphology. Geometric constraint exerts a somewhat less intuitive effect on solidification morphology when d/λ is marginally greater than one, causing cells to become unstable with respect to side branch formation, a cellular-dendritic transition. When $d/\lambda < 1$, curvature at the constraint destabilizes a planar front.

In similar experimental fashion, Fabietti and Sekhar [79] examine the effects of the solid-reinforcement interface energy on the liquid-solid interface morphology in the succinonitrile-acetone system. When the solid phase wets the reinforcement, half cell or half dendrite morphologies are observed within narrow channels. When the solidifying material does not wet the restraint, cells or dendrites centered in the channel are occasionally observed,

however, due to misorientation effects, non steady half cells and dendrites are also observed.

Shangguan and Hunt [80] studied the solidification of succinonitrile-acetone within a circular capillary tube to simulate cellular solidification within a fiber interstice of a metal matrix composite. The onset of instability of the planar front occurred simultaneously inside and outside the capillary tube, which contained only one cell. Capillarity-induced plane front stabilization was not observed, since the capillary tube diameter was greater than the unconstrained cell spacing. Side branch instability was observed earlier inside the capillary than in the bulk material, consistent with the observations and microstructure map of Trivedi, et al. [78].

McCartney and Hunt [50 , 52] calculated interface shapes for cylindrical cells with wavelengths near experimentally observed spacings. They observed that the tip undercooling increases slightly (by about 1 K for an aluminum alloy) as the cell radius is reduced to half its unconstrained spacing. This is in overall agreement with experimental data on dendritic solidification of Al- 4.5 % Cu/SiC fiber composites by Mortensen, Cornie and Flemings [74], who report no visible difference between tip temperature for geometrically constrained and unconstrained dendrites, the interstice width varying between 15 to 50% of the unconstrained primary dendrite arm spacing. Calculations for severe limitations of the cell size were not performed by McCartney and Hunt, but extrapolation of their results would be in good agreement with calculations by Trivedi et al. for undercooling when the cell width is decreased by an order of magnitude [78].

Small channel widths may also significantly decrease microsegregation because the upper limit on diffusion distances facilitates solid state diffusion during solidification. This phenomenon has been observed and analyzed by

Mortensen et al., [74] for SiC fiber reinforced Al-4.5% Cu, and Gungor [81-83] and Li, McCartney and Walker [84] for the same alloy reinforced with Al_2O_3 fibers.

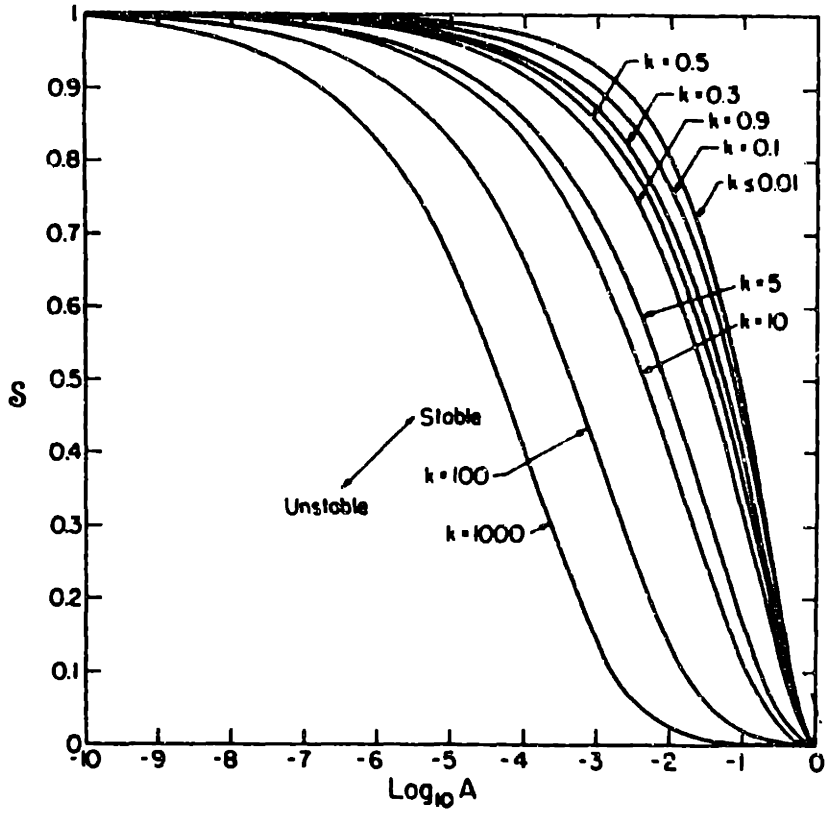

Figure 2.1. Graph of Sekerka's stability function, S, as a function of the solid-liquid partition ratio, k, and the stability parameter, A, defined in equation 2.9, from Sekerka [9].

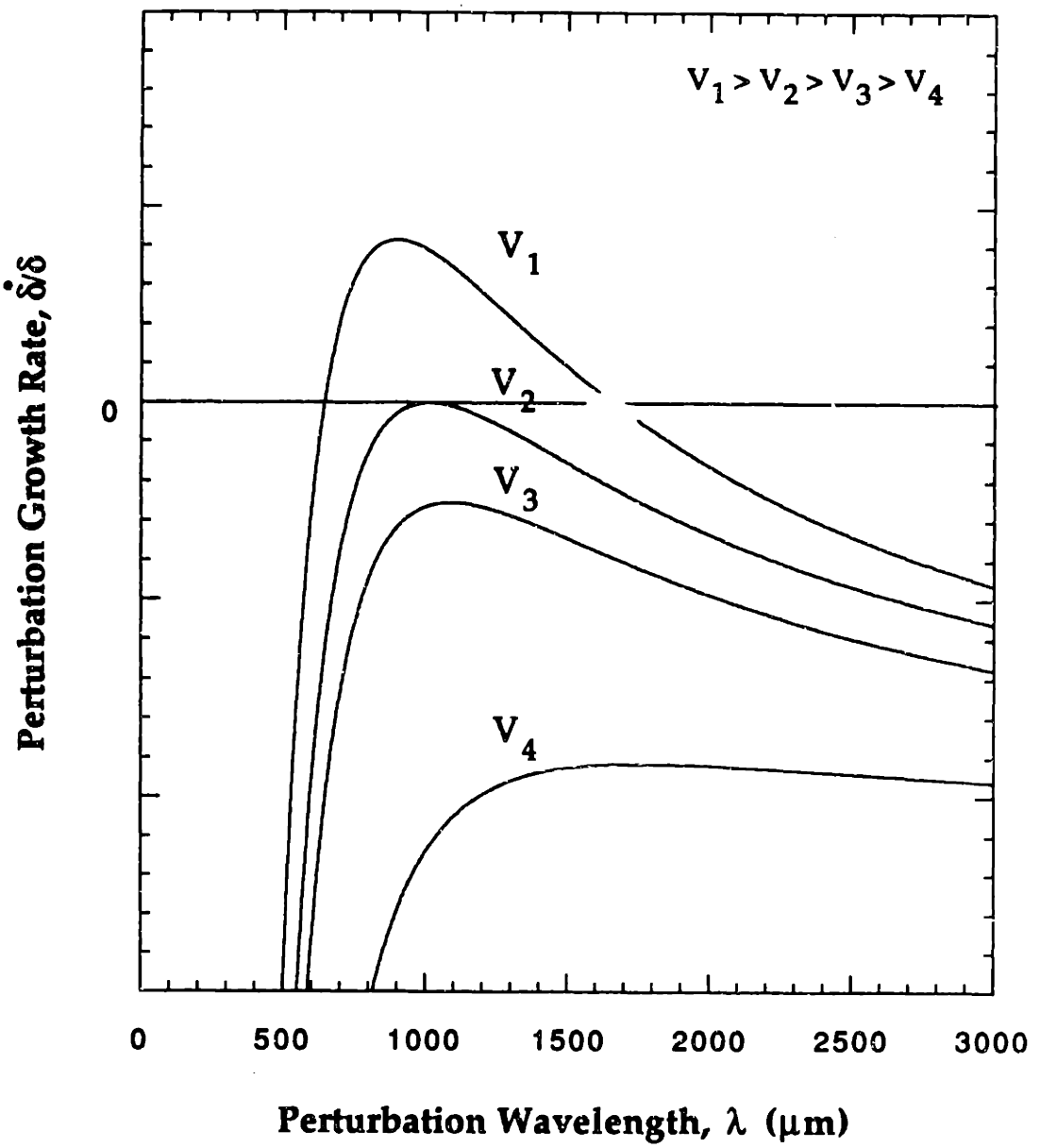

Figure 2.2 Perturbation growth rate, $\dot{\delta}/\delta$, for increasing interface velocity, V, according to the Mullins and Sekerka linear stability criterion (equation 2.5). A planar interface is stable for $V < V_2$.

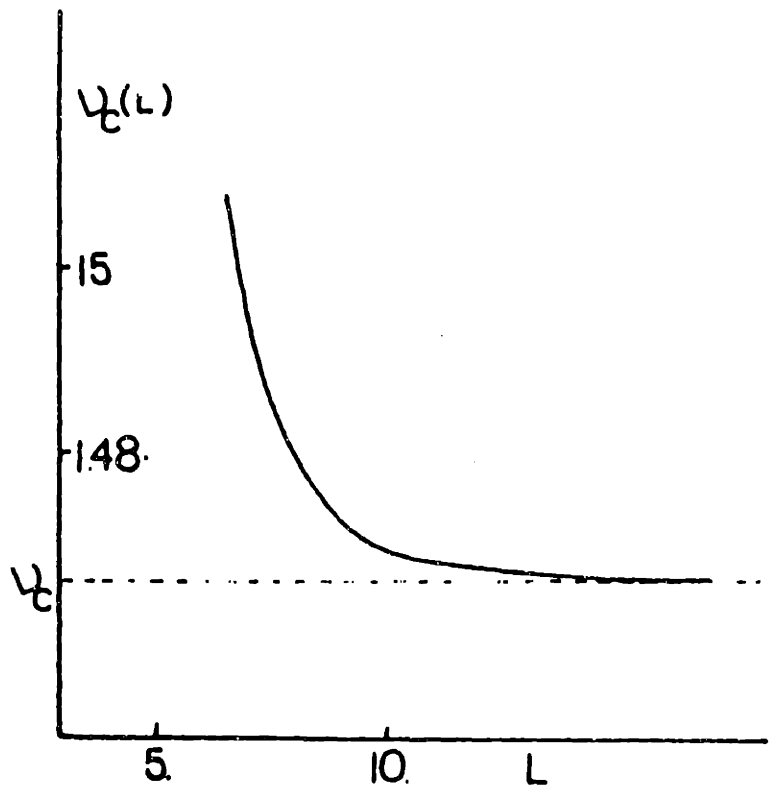

Figure 2.3 The critical velocity, V_c, for the onset of plane front instability increases dramatically when the system size, L, is smaller than 10 diffusion lengths (which equal D/V, D being the diffusion coefficient), for a symmetric model analyzed using Green's functions techniques. From Dee [44].

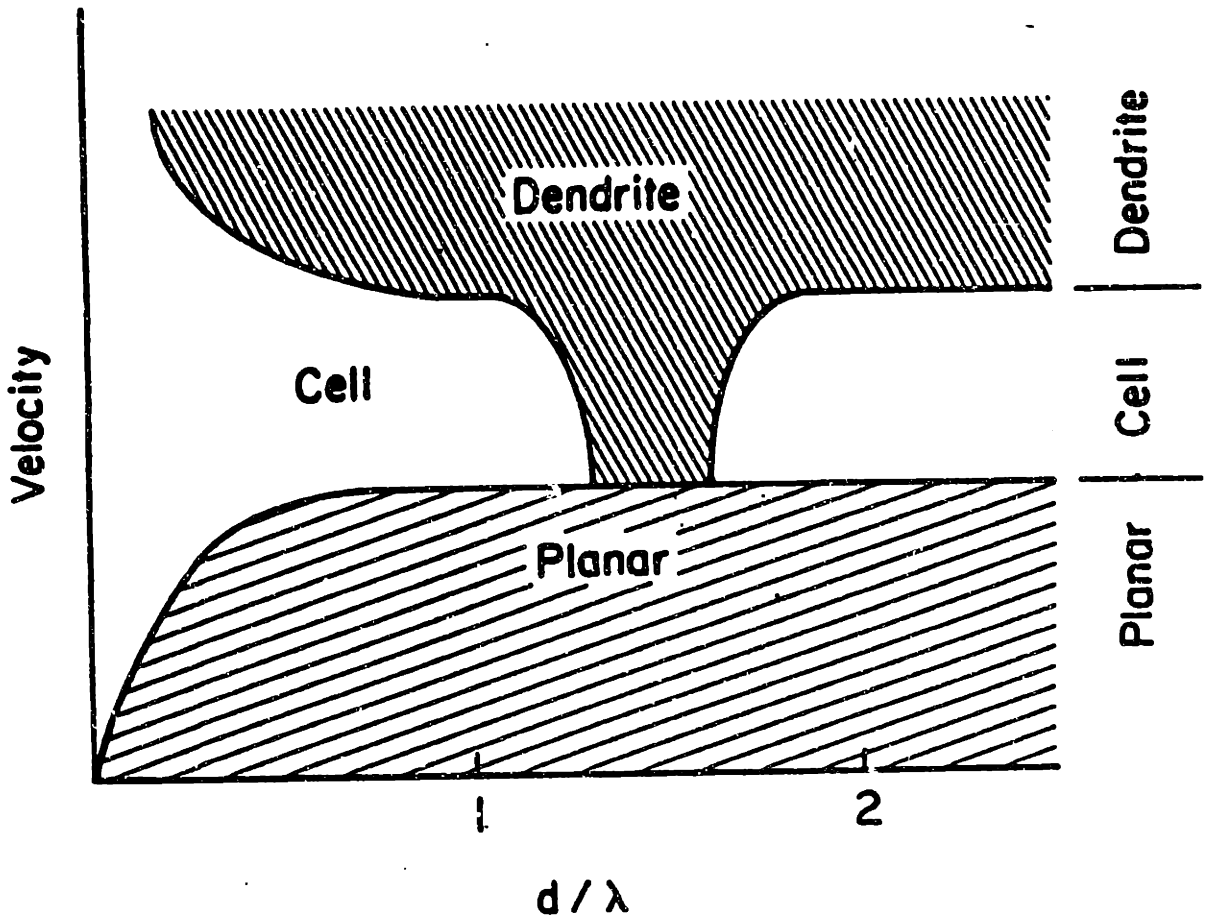

Figure 2.4 Schematic interface morphology map for velocity, V as a function of the ratio of channel size, d, to unconstrained interface periodicity, λ. A plane front is predicted to be unstable at low d/λ due to curvature at the liquid-solid-wall boundary. At low d/λ dendritic side branch instabilities are inhibited, while at d/λ slightly greater cells are unstable with respect to side branch formation, leading to a cellular-dendritic transformation. From Trivedi, Han and Sekhar [78].

Chapter 3

Theory

In much of solidification work to date, the sample cross-section is assumed to be infinite, or at least very large compared to the microstructural scale. This assumption allows a planar front to be considered unstable if any perturbation wavelength has a positive growth rate, and enables wall effects to be ignored. While this approach should be valid for unreinforced materials, it may break down when considering solidification within the geometrically constrained environment of a metal matrix composite. As discussed in the literature review, a reinforcing phase may interfere with matrix solidification in two manners. First, geometric constraints can limit a perturbation's size and present a physical barrier to diffusion. Secondly, mechanical equilibrium imposes the value of a finite contact angle, θ, at the junction of the liquid, solid and reinforcing phases, which when not equal to 90° induces curvature of the liquid-solid interface at a reinforcement. These effects are examined below.

3.1 Capillary Effects

A planar interface may be stabilized if the system, or interstice, size is smaller than the smallest stable perturbation. Table 3.1 lists calculated wavelengths at the onset of instability, λ_c, according to Mullins and Sekerka's [7] perturbation growth rate expression, (equation 2.5), for typical solidification conditions used in this investigation. These large critical wavelengths are geometrically excluded from occurring within typical reinforcement interstices. For solidification conditions near the onset of plane front

instability in unconstrained material, therefore, the liquid-solid interface morphology must be affected by a composite's reinforcement.

Table 3.1

Perturbation Wavelength at the Onset of Planar Front Instability

Alloy (wt. pct.)	Velocity (μm/s)	Gradient G^* (K/m)	Critical Wavelength λ_c (μm)
Al - 4.5% Cu	1.0	23300	870
Al - 4.5% Cu	2.0	46500	550
Al - 1.0% Cu	1.0	5230	1430
Al - 1.0% Cu	5.0	26000	490
Al - 1.0% Cu	10.0	51700	306

The effective wavenumber, ω_{eff}, of a three dimensional perturbation when $\lambda_x = \lambda_y = \lambda$, and the z direction denotes perturbation height, is given by:

$$\omega_{eff} = \frac{2\pi}{\sqrt{\lambda_x^2 + \lambda_y^2}} = \frac{\sqrt{2}\,\pi}{\lambda} \quad . \tag{3.1}$$

When considering a fiber interstice, λ is the average interstice diameter and ω_{eff} characterizes the smallest geometrically possible perturbation wavenumber (largest wavelength that will fit within that interstice).

As a first approximation of the geometric stabilizing influence on plane or pseudo-plane front matrix solidification, it is assumed that cellular solidification is impeded by a reinforcement if all perturbations with wavenumbers ω larger than the effective interstice wavenumber, ω_{eff}, decay according to linear stability analysis. By inspection of equation 2.5, a perturbation's growth rate is zero (perturbations are marginally stable) when

$$- T_M \Gamma \omega^2 - G^* + m_L G_c \left(\frac{\omega^* - V/D_L}{\omega^* - Vp/D_L} \right) = 0 \quad , \qquad (3.2)$$

where G_c, and ω^* are given by equations 2.2 and 2.8, respectively, and $p = 1 - k$. A Taylor series expansion of ω^*, when $2\omega D_L/V >> 1$ (which is generally true near the onset of plane front instability for ω larger than the critical wavenumber, ω_c) gives:

$$\frac{\omega^* D_L}{V} = \frac{1}{2} \left[1 + \sqrt{1 + (2\omega D_L/V)^2} \right] \approx \frac{1}{2} \left[1 + \frac{2\omega D_L}{V} \right] . \qquad (3.3)$$

Therefore, a perturbation of wavenumber ω_{eff} is unstable when:

$$- T_M \Gamma \omega_{eff}^2 - G^* + m_L G_c \left[\frac{\frac{2\omega_{eff} D_L}{V} - 1}{\frac{2\omega_{eff} D_L}{V} - 1 + 2k} \right] \leq 0 \quad . \qquad (3.4)$$

Equation 3.4 is linear in the conductivity weighted gradient, G^*, and quadratic in interface velocity, V, however roots of this quadratic equation do not have a compact analytical form. This equation is easily simplified for a typical eutectic system, since for $\lambda < \lambda_c$ ($\omega_{eff} > \omega_{eff,c}$):

$$(2\omega_{eff}D_L/V - 1) >> 2k \quad , \tag{3.5}$$

making the term within the brackets of equation 3.4 approximately one. After substituting the value for the concentration gradient from equation 2.2, equation 3.4 then becomes:

$$- T_M \Gamma \omega_{eff}^2 \; - G^* - m_L \frac{V C_0 (1-k)}{D_L k} \leq 0 \quad . \tag{3.6}$$

Solving for the interface velocity, V, for marginal stability of a perturbation with wavenumber ω_{eff} yields:

$$V = - \frac{D_L k (G^* + T_M \Gamma \omega_{eff}^2)}{C_0 m_L (1-k)} = V_{const.\ supercooling} - \frac{T_M \Gamma \omega_{eff}^2 D_L k}{C_0 m_L (1-k)} , \tag{3.7}$$

or in terms of the wavelength or cell diameter, λ:

$$V = V_{const.\ supercooling} - \frac{2\pi^2 T_M \Gamma D_L k}{\lambda^2 C_0 m_L (1-k)} . \tag{3.8}$$

Since $m_L < 0$, the critical velocity for the onset of instability increases when geometric constraints force the perturbation wavelength, λ, to be less than the critical wavelength, λ_c. The magnitude of this increase, defined as ΔV_{geom} is:

$$\Delta V_{geom} = - \frac{2\pi^2 T_M \Gamma D_L k}{\lambda^2 C_0 m_L (1-k)} . \tag{3.9}$$

Note that ΔV_{geom} is independent of temperature gradient, G. This implies that the slope of a line separating plane front and cellular growth conditions remains unchanged when geometric constraint enhances the stability of a planar interface. Critical solidification conditions for plane front instability when geometric constraints limit the maximum wavelength are shown in Figure 3.1 for Al-4.5 wt% Cu. Since ΔV_{geom} is inversely proportional to λ^2, the critical velocity for the onset of plane front instability will increase rapidly as λ becomes small, as seen in figure 3.2.

In a similar manner, equation 3.6 may be solved for the critical conductivity-weighted temperature gradient G*, at fixed interface velocity V and cell wavelength, λ:

$$G^* = m_L G_c - \frac{T_M \Gamma 2 \pi^2}{\lambda^2} , \qquad (3.10)$$

where $m_L G_c$ is the critical temperature gradient for stability of a plane front according to the constitutional supercooling criterion, equation 2.3. Equation (3.10) shows that G* must fall below a lower threshold before a plane front becomes unstable when perturbations are geometrically constrained to be smaller than λ_c (equation 3.6 is only valid for $\lambda < \lambda_c$ as indicated above). For Al-4.5 wt% Cu, the critical gradient for breakdown of a planar interface as a function of wavelength is presented in Figure 3.3.

Dee [44] found a similar relation between system size and the critical velocity for the breakdown of a planar front using Green's function techniques and assuming thermophysical properties were the same for both phases, as shown in Figure 2.2. His critical system size, defined as the size at which the critical growth rate for the breakdown of a planar interface

increases rapidly, seems rather large, on the order of one centimeter, for aluminum-copper alloys, compared to typical observed cell spacings which are one to two orders of magnitude less. However, the symmetric model is invalid for metal alloys, where $D_S << D_L$. The general trend of critical velocity increasing when very small cell spacings are imposed is consistent with the linear stability approach.

3.2 Cellular Equilibrium Solidification

We now consider the case where the composition of the solid phase at any given temperature is uniform, a case which we define as equilibrium cellular solidification. Assuming local interfacial equilibrium, the solid composition has the equilibrium solidus composition, given as a function of temperature, T, by the phase diagram. Because there is axial diffusion of solute in the liquid phase, cell tips are undercooled and when $m_L < 0$, the average composition along the cell decreases from C_t at the cell tips, to the nominal composition, C_0, at the cell root. Since overall composition is not uniform, this case differs from that of phase diagram equilibrium, or lever law, solidification.

Following a procedure similar to that of Bower, Brody and Flemings [54] (BBF) for the case of no solid phase diffusion, we can derive the fraction solidified, f_S, as a function of local temperature, T, or, equivalently, liquid composition C_L. As in the derivation of the BBF equation, we assume that liquidus slope, m_L (<0) and partition ratio, k (<1) are constant, that the liquid composition at any given temperature below the alloy liquidus is uniformly equal to the liquidus composition, that there is no cell undercooling due to curvature or kinetic effects along the cell surface and that the density of both phases are equal and independent of temperature and composition.

Considering a transverse slice of the cell of thickness dx, in which incremental solidification, df_s, occurs, a mass balance yields:

$$f_S\, dC_S + f_L\, dC_L + C_L\,(1\text{-}k)\, df_L = -D_L \frac{\partial C_L}{\partial x} \frac{dt}{dx}\, df_L \quad , \qquad (3.11)$$

where

$$dC_S = k\, dC_L \quad . \qquad (3.12)$$

Substituting and rearranging yields:

$$[k + f_L\,(1\text{-}k)]\; dC_L = -\left[C_L\,(1\text{-}k) + \frac{D_L G_L}{m_L V}\right] df_L \quad . \qquad (3.13)$$

Integrating from $C_L' = C_t$ at the cell tips to some point along the cell $C_L' = C_L$:

$$\int_{C_t}^{C_L} \frac{dC_L'}{C_L'\,(1\text{-}k) + \frac{D_L G_L}{m_L V}} = -\int_{1}^{f_L} \frac{df_L'}{k + f_L'\,(1\text{-}k)} \qquad (3.14)$$

So that,

$$C_L = \frac{C_t + (1 - f_L)\frac{D_L G_L}{m_L V}}{k + f_L\,(1\text{-}k)} \qquad (3.15)$$

If we assume that the cell tip composition is given by the BBF expression (equation 2.12), this reduces to:

$$C_L = C_0 \left[\frac{1 - a\,(1-f_s)}{1 - f_s\,(1-k)} \right] \quad , \tag{3.16}$$

or

$$f_s = \frac{C_L - C_0 + aC_0}{C_L - C_s + aC_0} \quad , \tag{3.17}$$

where a is the Bower, Brody and Flemings [54] cell tip undercooling parameter given by equation 2.14. In Figure 3.4, temperature versus fraction solid in Al - 4.5% Cu is plotted for the limiting cases of the BBF model, which considers no diffusion in the solid (equation 2.16) and equilibrium cellular solidification, given by equation 3.17.

3.3 Finite Difference Cellular Solidification Model

The two models considered above, namely of no and complete diffusion in the solid phase at temperature T, are limiting cases. Predicting the solute distribution and shape of growing cells is a three-dimensional free boundary problem that requires a numerical approach for its solution. While several models, reviewed in the literature survey, exist to date for cellular growth, no model has been found which could be used to predict the microsegregation that results from cellular solidification of the alloys explored in this work.

We have, therefore, expanded the finite difference model of Mortensen et al. [74] to include the effect of a cell tip undercooling, which we assumed is described by the BBF expression (equation 2.13), and density-driven convection in the intercellular liquid. Use of the BBF expression for tip undercooling and geometrical assumptions of the model render it incapable of predicting cell geometry near its tip; however, while relatively simple

compared to other models, it is expected to predict microsegregation in the later stages of solidification with adequate precision.

3.3.1 General Problem

The solid is modelled to be growing at steady state within a cylinder of radius r_T, which closely approximates an element of the hexagonal array typically observed during cellular solidification. The radial symmetry of the diffusion field translates the three-dimensional problem into a two-dimensional one. The solid phase is assumed to grow with circular symmetry in the center of this cylinder. To model growth within a fiber interstice, r_T is chosen such that the cylinder cross sectional area is identical to that of the interstice.

3.3.2 Assumptions

Principal assumptions in this model are:

1). Isotherms are flat and perpendicular to the growth direction.

2). Complete mixing of liquid in the radial direction. The intercellular liquid is assumed to have a uniform composition, C_L, equal to the liquidus composition at the local temperature. This is justified since the liquid solute diffusion coefficient is four orders of magnitude larger than the solid state diffusion coefficient, and intercellular channels are narrow. This assumption breaks down somewhat near the cell tip, but has been shown by finite element calculations to be valid for regions behind the tip [48, 50 , 52].

3). Constant m_L and k. The Al-rich corner of the of the Al-Cu phase diagram is well approximated by straight lines, validating this assumption. Liquid and solid compositions are then linear functions of temperature.

4). Constant density of the primary solid. The volume change associated with temperature and compositional changes within the primary solid are ignored, since density variations in the primary solid are not significant compared to the density variation over the allowable liquid composition range.

5). No undercooling due to interface curvature. The Gibbs-Thomson, or curvature, undercooling constant is 2.41×10^{-7} Km [85] indicating curvature undercooling will not be significant unless the radius of curvature is less than 1μm. Cell tip radii are much larger than this.

6) No significant kinetic undercooling.

3.3.3 Governing Equations

Assuming constant thermal gradient G_L (>0) and growth rate V, the local temperature, T, is given by:

$$T = T_t - G_L V t \quad , \tag{3.18}$$

where T_t is the cell tip temperature, and t is the local solidification time.

Diffusion in the solid obeys Fick's Second Law:

$$\frac{\partial C_s}{\partial t} = \nabla \cdot (D_s \nabla C_s) \quad , \tag{3.19}$$

where C_s is solid composition and D_s is the solid solute diffusion coefficient. The liquid-solid interface is located at $r^* \leq r_T$. Assuming that the diffusion coefficient is independent of composition and neglecting diffusion along the cylinder axis, Fick's second law becomes:

$$\frac{\partial C_s}{\partial t} = D_s\left(\frac{\partial^2 C_s}{\partial r^2} + \frac{1}{r}\frac{\partial C_s}{\partial r}\right) \quad , \tag{3.20}$$

subject to the boundary conditions:

$$\frac{\partial C_s}{\partial r} = 0 \qquad \text{at} \quad r = 0 \quad , \tag{3.21}$$

$$C_s = k C_L^* \qquad \text{at} \quad r = r^* \quad , \tag{3.22}$$

where C_L^* is the liquid composition at the interface and k is the equilibrium partition ratio. The initial condition is

$$r^* = 0 \qquad T = T_t \; . \tag{3.23}$$

Fick's second law in the intercellular liquid comprises an additional term for convective mass transport:

$$\frac{\partial C_L}{\partial t} = \nabla \cdot (D_L \nabla C_L) - \vartheta_L \cdot \nabla C_L \quad , \tag{3.24}$$

where ϑ_L is the intercellular liquid velocity. Since it is assumed the liquid is of uniform composition at any temperature and that the isotherms are flat, the gradient in liquid composition has only an axial component. Assuming the liquid solute diffusivity is independent of temperature and composition:

$$\frac{\partial C_L}{\partial t} = D_L \frac{\partial^2 C_L}{\partial z^2} - \vartheta_L \frac{\partial C_L}{\partial z} \quad . \tag{3.25}$$

The far field boundary condition is:

$$C_L = C_0 \quad . \qquad \text{as } z \rightarrow \infty \quad (3.26)$$

The liquid composition and temperature are coupled at the interface by the phase diagram:

$$T = T_M + m_L C_L \quad . \qquad (3.27)$$

where T_M is the melting point of pure solvent and m_L is the phase diagram liquidus slope. Differentiating this expression with respect to z, the cell axis, yields the liquid composition gradient for all points behind the cell tips,

$$\frac{\partial C_L}{\partial z} = \frac{1}{m_L}\frac{\partial T_L}{\partial z} = \frac{G_L}{m_L} \quad . \qquad (3.28)$$

The Bower, Brody and Flemings model for tip undercooling [54] , which is consistent with our previous assumptions gives the initial condition, or tip liquid composition C_t:

$$C_t = C_0 (1 - a) \quad , \qquad (3.29)$$

where a is the BBF parameter, defined in equation 2.14.

Continuity of matter dictates:

$$\frac{\partial \rho_L}{\partial t} = \nabla \cdot (\rho_L \vartheta_L) \quad , \qquad (3.30)$$

where ρ_L is the liquid density and ϑ_L the intercellular liquid velocity. Since the liquid is assumed to have uniform composition for any isotherm, which is assumed to be flat, the velocity and density gradients have only axial components. Thus,

$$\frac{\partial \rho_L}{\partial t} = \frac{\partial (\rho_L \vartheta_L)}{\partial z} \quad . \tag{3.31}$$

Conservation of matter at the cell root dictates:

$$\vartheta_L = \left(\frac{\rho_{L\,root} - \rho_{s\,root}}{\rho_{L\,root}} \right) V \qquad \text{at} \quad z = 0 \ , \tag{3.32}$$

where $\rho_{L\,root}$ and $\rho_{s\,root}$ are the liquid and solid densities at the cell root, respectively. Depending on the cell root temperature, $\rho_{s\,root}$ may be the density of the primary solid, or eutectic solid metal. The liquid density, ρ_L is considered to vary with composition and, hence, with temperature and axial position, following experimental data for Al-Cu alloys reviewed in Appendix B.

Finally, a solute mass balance at the liquid-solid interface couples the composition, intercellular liquid velocity and interface position:

$$C_L \rho_L (1-k) df_s - f_L \, d(C_L \rho_L) - D_s \rho_s \left(\frac{\partial C_s}{\partial r} \right)_{r = r^*} \frac{2 r^* \, dr^*}{r_T^{\,2}} \frac{dt}{dz} =$$

$$-D_L \frac{\partial (\rho_L C_L)}{\partial z} \frac{dt}{dz} \, df_L + \frac{\partial (f_L C_L \rho_L \vartheta_L)}{\partial z} \, dt \ , \tag{3.33}$$

where

$$f_S = \left(\frac{r^*}{r_T} \right)^2 \quad . \tag{3.34}$$

so:

$$df_S = - df_L = \frac{2\, r^*\, dr^*}{r_T^{\,2}} \quad . \tag{3.35}$$

Since this is a free boundary problem, a self consistent interface shape must be found simultaneously with the composition and intercellular liquid velocity profiles. A computer based finite difference program, detailed in Appendix C, was used to solve this problem.

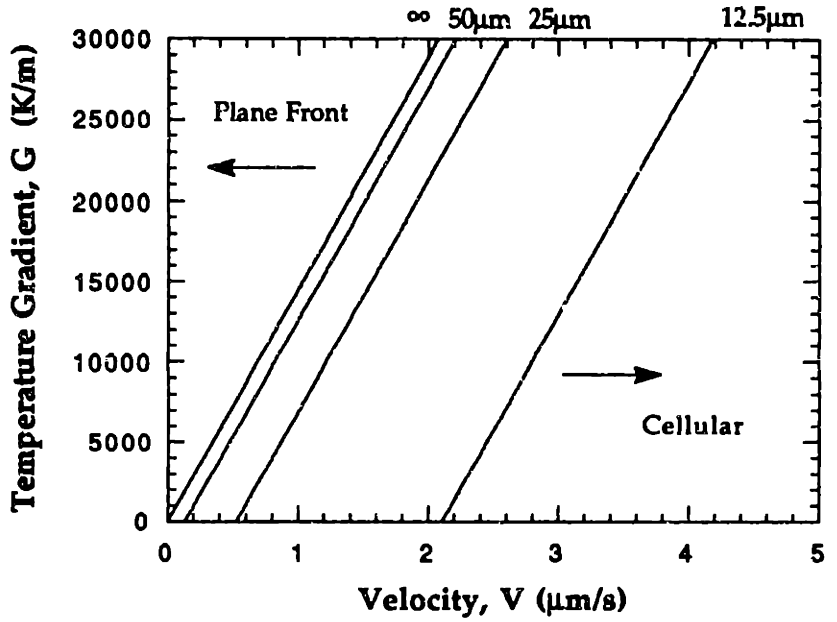

(a)

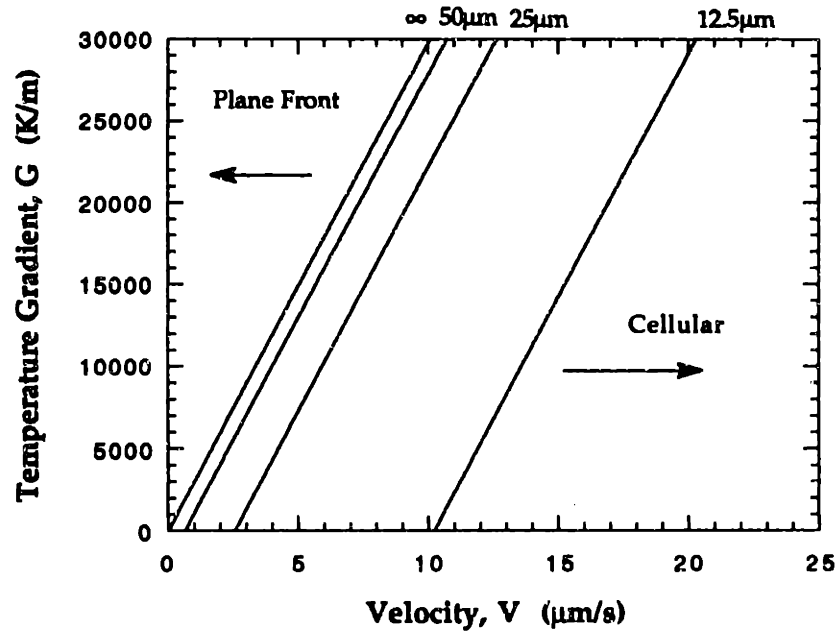

(b)

Figure 3.1 Plane front to cellular transition for geometrically constrained solidification of a) aluminum 4.5 % copper and b) aluminum - 1.0% copper as a function of the temperature gradient, G, and interface velocity, V, according linear stability theory. Labels denote the maximum perturbation wavelength.

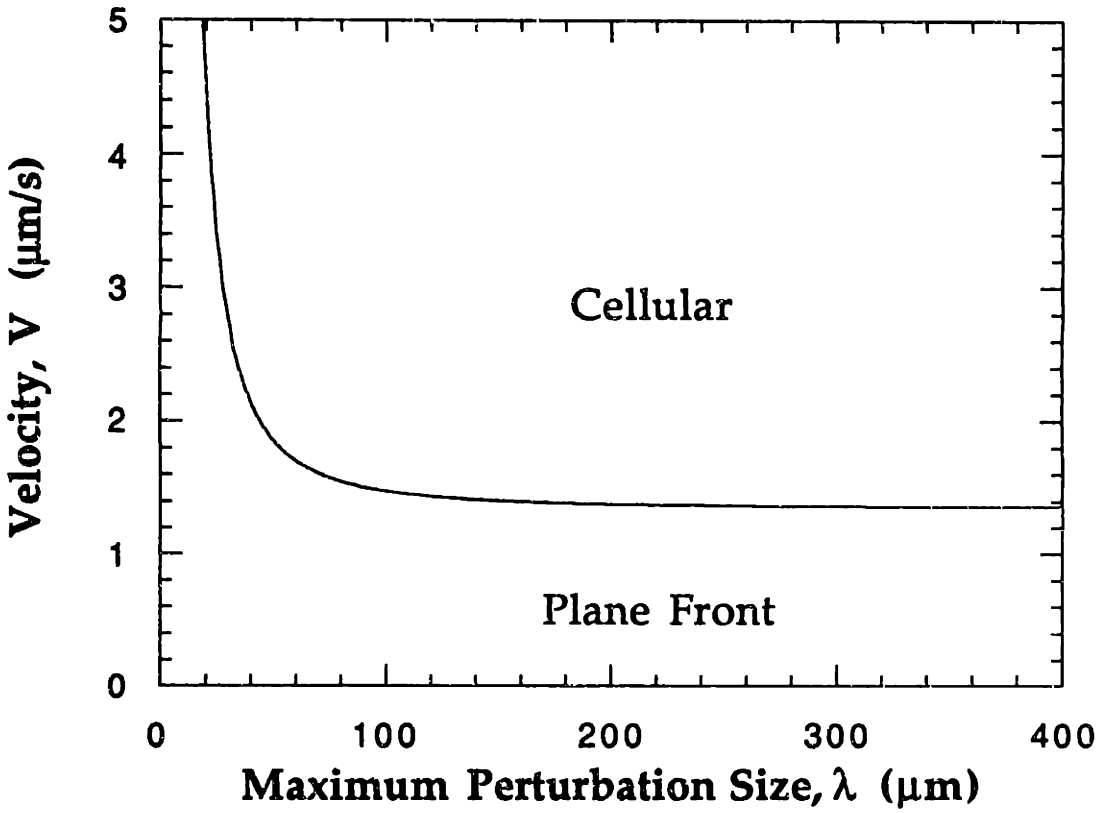

Figure 3.2 Critical velocity, V, for the onset of plane front instability as a function of maximum perturbation wavelength, λ, according to equation 3.10. Aluminum - 4.5% copper, $G^* = 20000$ K/m.

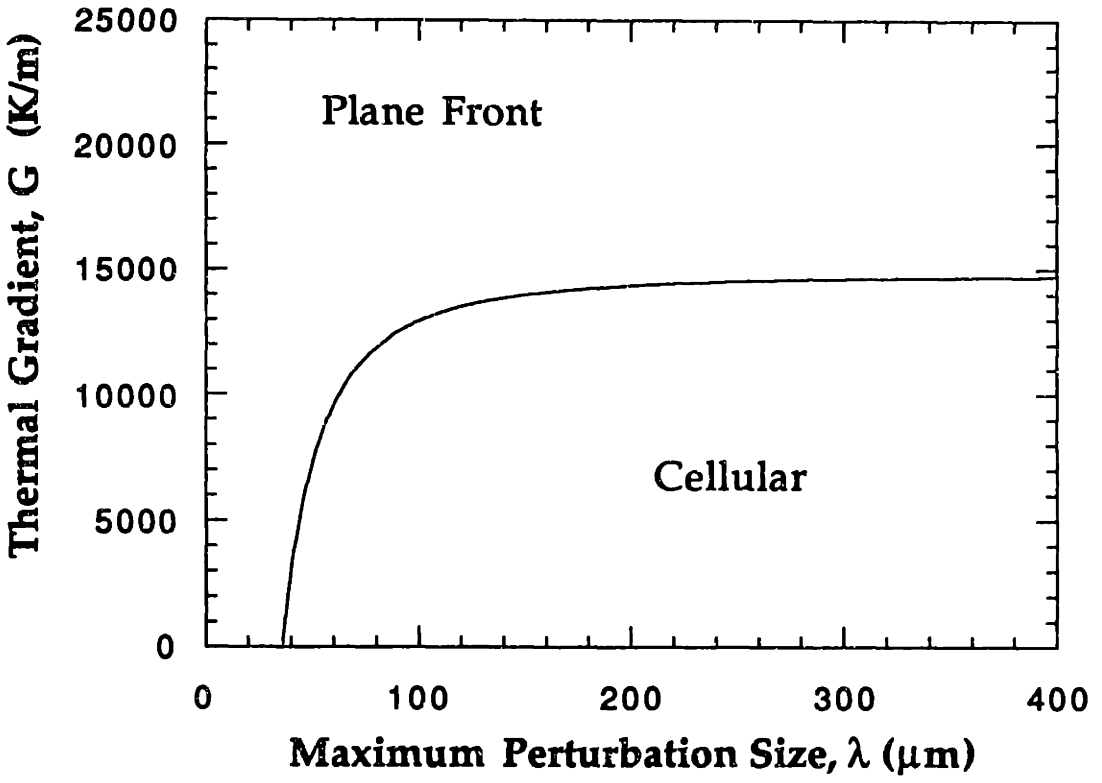

Figure 3.3 Critical effective temperature gradient, G*, for the onset of planar front instability as a function of the maximum allowed perturbation wavelength, λ, according to equation 3.7. Aluminum 4.5 % Copper, V = 2.0 μm/s.

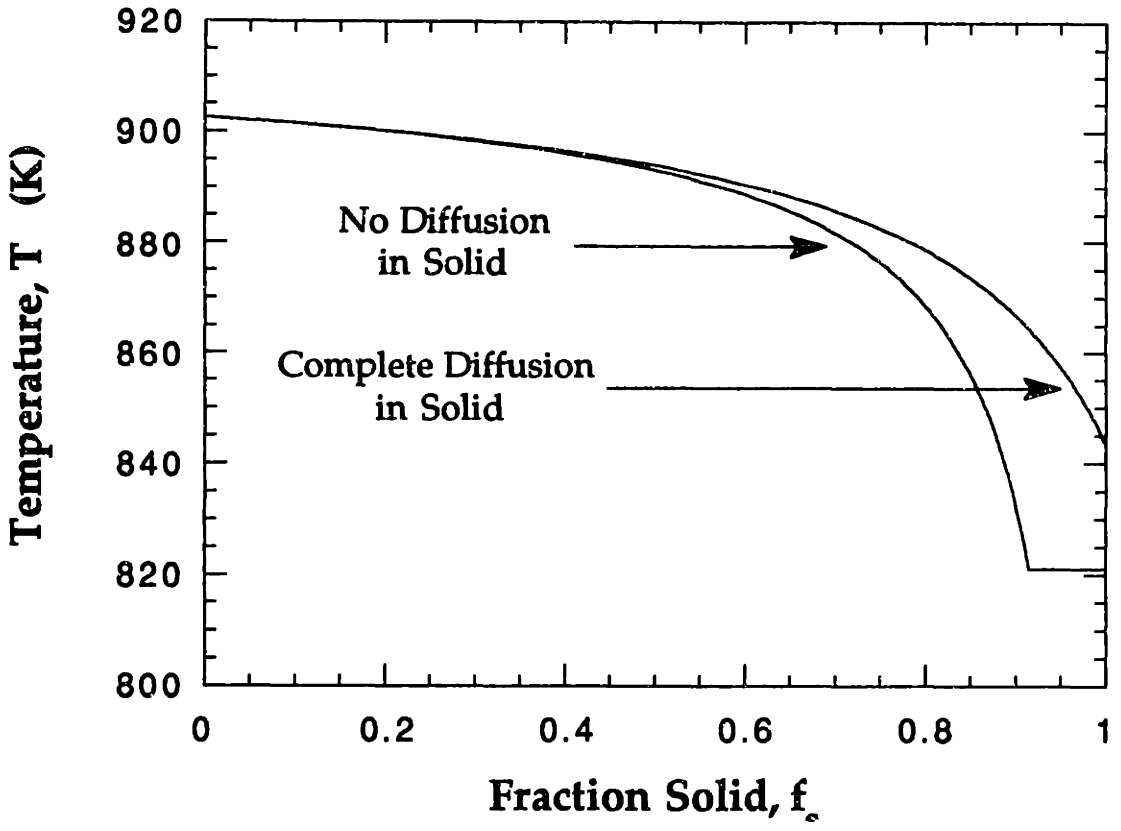

Figure 3.4 Fraction solid as a function of distance from the cell tips for the limiting cases of no diffusion in the solid and complete diffusion in the solid. Aluminum 4.5 % copper, a = -1.

Chapter 4

Experimental Procedure

4.1 Materials

Two alloy/fiber combinations were used in this investigation: Al-4.5%Cu/Fiber FP™ and Al-1.0% Cu/Fiber FP™. The aluminum rich portion of the aluminum-copper system is well characterized, featuring a eutectic reaction and a liquidus and solidus which are well approximated by straight lines, as discussed in Appendix B. Fiber FP™ is a 20μm diameter α-Al_2O_3 fiber manufactured by DuPont (Wilmington, Delaware), known to be chemically inert in Al-Cu alloys [82].

Transverse slices of Al-4.5% Cu (99.9%), or high purity aluminum (99.999%) were cut far from the ends of large ingots to avoid fluctuations in composition caused by macrosegregation. Enough metal to make 700 grams of alloy was sectioned and cleaned in a NaOH solution, then scrubbed with soap and water using a nylon brush.

To produce the Al-1.0% Cu alloy, the Al-4.5% Cu master alloy was diluted in pure aluminum. Alloys were melted in a pure graphite crucible. After reaching 100K superheat, the melt was stirred for seven minutes using a graphite stirrer (Figure 4.1), moving at a rate of 30 strokes per minute to push upwards solute rich liquid at the bottom of the crucible. A copper-colored liquid was observed breaking the surface at the beginning of stirring, while at the end a uniform alloy color was obtained, indicating effective mixing had occurred.

After stirring, argon was bubbled through the melt for one minute and the melt surface was skimmed. The sample ingots were cast by drawing liquid metal into pyrex tubes and immediately quenching in water. Ingots were easily removed from the glass tubes, indicating that no chemical reaction had occurred between tube and metal. The surface of each small ingot was cleaned by grinding, then ultrasonically cleaning for three minutes, soaking in a NaOH solution for three minutes and scrubbing with soap, water and a nylon brush. Chemical and microstructural analyses were done on samples from the beginning, middle and end of each alloying and casting session.

4.2 Composite Sample Preparation

4.2.1 Crucible Fabrication

Composite materials were fabricated using pressure infiltration in small sealed-end alumina tubes, following a procedure described by Isaacs et al. [86]. Extruded alumina tubes, sealed at one end to form crucibles, were used in preference to alumina crucibles cast with one end closed because the cast crucibles usually cracked while in the Bridgman furnace, presumably due to thermal cycling. Sealing of the alumina tubes (3.96 mm OD, 2.39 mm ID, McDanel Corp.) was accomplished by slowly placing one end of a rotating tube into an oxy-acetylene flame; as the alumina melted, the tube sealed by capillary action. To ensure they were impermeable to pressurized gas, the seals were tested for leaks in soapy water then coated with Aremco Ceramabind™ 503 or 569 alumina cement (Aremco Products, Ossissing, NY) and cured. Tubes exhibiting cracks in the cement layer were recoated.

4.2.2 Fiber Packing

1.6 g of FP™, corresponding to a composite containing 50-60 volume percent fiber, were soaked in distilled water, aligned and trimmed to a length of five inches. The fiber bundle was then compressed radially and pushed into the sealed crucible with minimal shearing at the circumference of the preform. Water from the fibers was driven off by heating the crucibles to 250°C for five or more hours.

4.2.3 Infiltration of Fiber Preforms

An alloy ingot was placed in the crucible above the dried fibers. Several crucibles were loaded into a crucible holder (a 1" x 12" steel tube with a flat bottom) which was placed into a pressure infiltration apparatus described in Ref. [86]. Casting procedure was essentially similar to that described previously, casting temperature was 700°C, infiltration pressure 5 to 7 MPa and sample solidification took place under an applied pressure of 5 MPa.

After cooling, the crucible was sectioned 4.75 inches from the bottom, preserving most of the composite, yet allowing a portion to be inspected for infiltration quality. In early experiments, the crucible was centered radially and cemented into a 0.250" OD, 0.187"ID (McDanel) alumina tube. In later experiments, the composite was removed from its crucible before being cemented into a similar larger tube.

A large ingot was placed above the composite in the larger crucible, which was placed in the same pressure infiltration machine, to force molten aluminum alloy around the composite sample. An applied gas pressure of 2 MPa was used. Preheated thermocouples encased in alumina protection tubes were inserted into the sample tubes and the sample/crucible assemblies were solidified under pressure.

Thermocouple protection tubes were chosen to have the same cross-sectional area as the combination of fibers and inner crucible (if present) to ensure the bulk longitudinal thermal conductivity was uniform along the sample. Scaled drawings of the final samples are shown in Figure 4.2. Note that fibers are aligned with the crucible axis, so that steady state, directional solidification will occur within fiber interstices, as shown schematically in Figure 4.3.

4.3 Directional Solidification

Samples were directionally solidified using the Bridgman furnace depicted in Figures 4.4 and 4.5. The quench tank consisted of a flowing cold water bath with O-ring seals. The two-part hot zone used resistance heating elements; the lower measured 1.25 inches in diameter and two inches in length, while the upper heating element had the same diameter but a 4 inch length. Upper and lower heating elements were governed by Omega model 300 and CN5001 controllers, respectively. The sample was driven through the temperature gradient by a shunt wound motor in line with an 11:1 reducing gear box and a nut/threaded rod. Sample withdrawal rate could be varied from 1 to 50 μm/s. Speeds below 1 μm/s were achievable in practice, but were not used as the thermal fluctuations of the apparatus, measured to be on the order of 1K per 3 minutes, would cause interface movement of that produced by translation.

Samples were raised into the furnace until their thermocouple registered 100-140 K above the alloy liquidus. Temperature was allowed to stabilize before withdrawing the crucible at a selected constant rate, V. Sample and furnace temperatures were recorded every ten seconds with a Digistrip II (Kaye Instruments) connected to an Apple Macintosh™. After solidifying

approximately three centimeters of composite, the crucible was released and the sample pulled rapidly into the quench tank to freeze remaining liquid, allowing metallographic analysis of the liquid-solid interface. At the time of quench, about four inches of composite with a liquid matrix was present above the liquid-solid interface. This ensured that end effects were absent at the time of quench, as characteristic distances for heat and solute diffusion are less than this value. The distance solidified within each composite was at least two times the charactersitic length of the initial transient during plane front solidification [87]. It is reasonable to assume, therefore, that steady-state solidification conditions were approached.

The growth velocity, V, was measured in several ways. The time for the motor to make 11 revolutions, corresponding to one revolution on the threaded shaft, was measured. Since the distance between threads was known, the speed was easily determined. The value for the growth velocity was confirmed with marks indicating total distance travelled by the crucible during the run. Translation rate was periodically calibrated by correlating motor rotation speed with vertical displacement using a machinist's indicator with 1 inch of travel.

Thermal gradients in the liquid and the solid were computed from plots of measured temperature versus time and hence distance, an example of which is given in Figure 4.6.

4.4 Metallographic Preparation

After removal from its crucible, a bevel was ground into each sample and the position of the liquid-solid interface revealed using Keller's etch. The sample was then sectioned with a low-speed diamond saw and mounted in bakelite. The grinding and polishing sequence was as follows:

1) Grinding by hand on 400 grit and 600 grit SiC paper.

2) Rough polishing with 15μm diamond slurry on a MetLab™ 10 spiral platen using a Minimet™ set at load = 1/2 maximum and polisher speed = 4, until a flat surface was obtained.

3) Intermediate polishing using 6μm diamond paste on Texmet™ cloth for 10 minutes with the load = 1/2 and speed = 4.

4) For the Al-1%Cu/FP™ samples an additional polishing step using 1μm diamond paste on Texmet™ cloth was used. Polishing time was 10 minutes with the load = 1/2 and speed = 4.

5) Final polishing with Mastermet™, a colloidal silica solution, on Chemomet™ cloth for 15-20 minutes at load = 1/2 and speed = 2. The colloidal silica solution required special handling. If not properly cleaned, the silica crystallized, leaving a thin film on the sample's surface. This film would inhibit observation of the microstructure as well as prevent etching. To avoid crystallization, the Mastermet™ was heavily diluted with distilled water during the last minute of polishing, and the sample was washed with copious amounts of distilled water. The polishing cloth was thoroughly rinsed and stored under distilled water. (Minimet™, Metlap™, Texmet™, Mastermet™, and Chemomet™ are trademarks of Buehler, Lake Bluffs , Indiana.)

At the end of each polishing step, the samples were rinsed and ultrasonically cleaned in distilled water. Immediately after polishing, the samples were etched with Keller's Etch or with an etchant consisting of 4g $KMnO_4$ and 2g NaOH dissolved in a liter of water to reveal coring patterns in the primary solid [88].

4.5 Microstructural Characterization

Relating solidification microstructure to processing conditions is the major focus of this work. While character of the interface morphology in the ureinforced sections was clear, the impact of a non-planar interface on final solidification microstructure, and hence properties, depends on both microstructural scale and degree of microsegregation. Characterization of the microstructure will bediscussed in this section, while microsegregation measurements are discussed in the following section. Cellular interfaces can be characterized by the average cell spacing or diameter, λ, and the distance from the cell tips (where the volume fraction solid, g_s, is zero) to the cell roots (where $g_s = 1$). This distance is defined as the cell height, ΔX. Within a composite, solidification under conditions of geometric constraint implies that the average cell diameter is fixed by the reinforcement geometry, so the cell height, ΔX, becomes the primary means of characterization.

At the eutectic temperature any remaining liquid transforms to eutectic solid, and hence the volume fraction solid, g_s, becomes one. When a clear eutectic front was present, the distance between cell tips and the eutectic front, which is ΔX, was measured. In the absence of a eutectic front, however, there is uncertainty in the point where a specimen is fully solid (g_s reaches one), especially for the composite samples where the volume fraction solid appears to increase rapidly with distance behind the cell tips,and then assymptotically aproaches one. For this reason, the distance between the cell tips and the location where measured volume fraction solid, g_s, reached 0.95, defined as $\Delta X_{0.95}$, was used as a measure of cell height. $\Delta X_{0.95}$ was determined from plots of g_s versus distance, as shown in figure 4.7.

The volume fraction of solid, g_s, was measured as a function of distance from the cell tips for all composite sections and those unreinforced sections

which exhibited cellular interface morphologies. Measurements on unreinforced samples with a fine equiaxed dendritic structure for the quenched liquid (dendrite arm spacings less than 10 μm) were made using the image processing method detailed below. Four composite samples, solidified under conditions far removed from the onset of instability of the unreinforced matrix were examined with this image processing method as well. All other samples were measured by manual point counting.

Digital images for automated analysis were produced by either electronically capturing an image from a light microscope or scanning photomicrographs. Image processing was done with IPLab™ (Signal Analytics Corporation, Vienna, VA) on an Apple Macintosh™ IIci. Fine equiaxed dendrites and a fine eutectic structure are microstructural features that were liquid at the time of the quench. Dendrites in the quenched liquid were mathematically closed (essentially blurring the dendritic structure), making phase contrast high enough to separate all phases by color or grey scale intensities. Pixel intensity was reassigned so that each phase was uniformly colored. Phase proportions, and thus fraction solid, were calculated by counting the number of pixels corresponding to primary solid, liquid and fiber in isothermal bands. This sequence is illustrated in Figure 4.8. Several images for each sample were analyzed. The Macintosh™ screen had a resolution of 640 x 480 pixels.

Cell spacings, λ, were measured via light microscopy. Since morphological cells are usually arranged in hexagonal arrays, measurments of cell spacing are best done on sections that transverse the growth direction. In this work, however, longitudinal sections were of greater interest for determining interface morphology. If the hexagonal array is approximated by an array of cylinders, a correction factor of $4/\pi$ [89] can be used to calculate

true cell diameter using the average measured cell width. This correction factor accounts for the polished section not coinciding with cell axes, and hence not revealing true cell diameters. Average cell widths are also shoqn schematically in figure 4.7.

Since the fibers were not regularly arranged, an average interstice diameter, corresponding to the average cell diameter, must be measured on samples where the growing cells are delineated by a thin film of liquid. Transverse metallographic sections, corresponding to regions which were partially solid at the time of the quench were etched to reveal areas which had been liquid. The volume fraction of fiber, number of fibers and number of cells were measured on these sections. The average cell radius in the composite is given by:

$$r_{interstice} = r_{cell,\ reinforced} = r_{fiber}\sqrt{\frac{1-V_f}{V_f}\frac{\#fibers}{\#cells}}\ , \qquad (4.1)$$

where V_f is the volume fraction fiber in the composite sample, and the number of fibers (# fibers) and number of cells (# cells) are counted over the same cross sectional area of composite. Fiber volume fraction was also measured on longitudinal sections of the solidified composites while determining the volume fraction of primary solid.

4.6 Microsegregation Analysis

Volume fraction eutectic, g_E, was measured on all samples. Where a clear eutectic transition was visible, the volume fraction of theta phase (Al_2Cu), was measured at the eutectic front. From this value, the volume fraction of eutectic solid, with composition given by:

$$C_{SE} = C_E + a\,C_0 \quad , \tag{4.2}$$

where C_{SE} is the eutectic solid composition, C_E is the eutectic composition, C_0 is the nominal compositiona and a is the Bower-Brody-Flemings parameter, defined in equation 2.14, could be determined. Where a clear eutectic transition was not visible, the volume fraction of quenched liquid (represented by a fine lamellar structure) was measured near the expected eutectic isotherm. Since liquid transforms to eutectic solid at the eutectic temperature, this measurement corresponds to a volume fracton eutectic.

Transverse composition profiles across fiber interstices within two composite samples (Samples 209 and 218) were measured with a JEOL Superprobe 733 scanning electron beam x-ray microprobe equipped with a wavelength dispersive spectrometer. Samples were metallographically prepared as above, but not etched. Because the alumina fibers are not conductive, the samples required a thin (~100 Å) carbon coating to prevent electron charging. Pure aluminum and copper were used as standards, as in similar experimental work [82 , 88]. The beam acceleration voltage was 15 kV and the beam current was 10 nA. The sample was tilted 40° with respect to the electron beam. Al K_α and Cu K_α peaks were used and a ZAF correction was automatically performed.

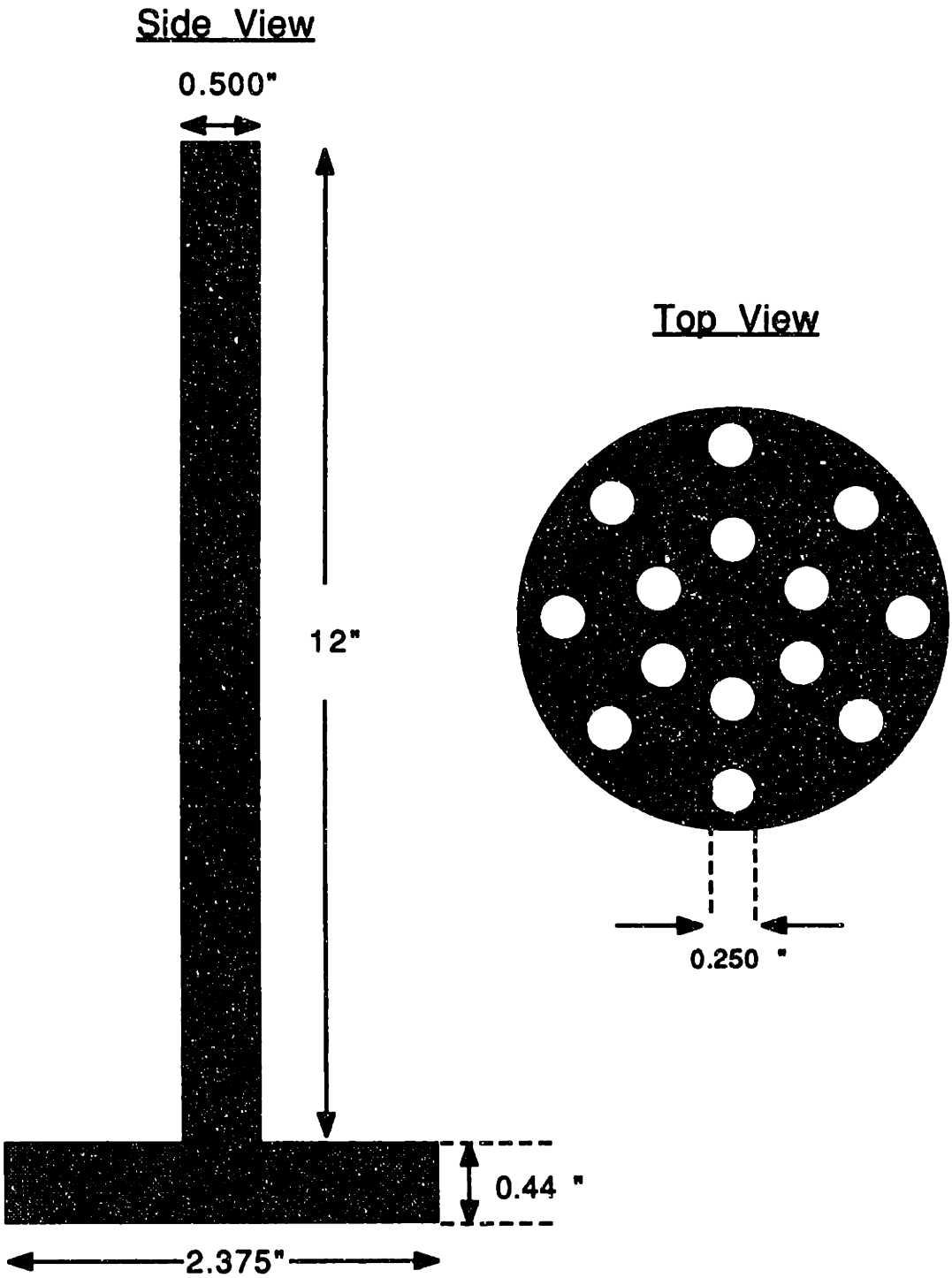

Figure 4.1 Graphite stirrer used in casting metal ingots. Stirrer has a close fit with the graphite crucible, forcing liquid metal to be exuded upwards when the melt is stirred with vertical strokes.

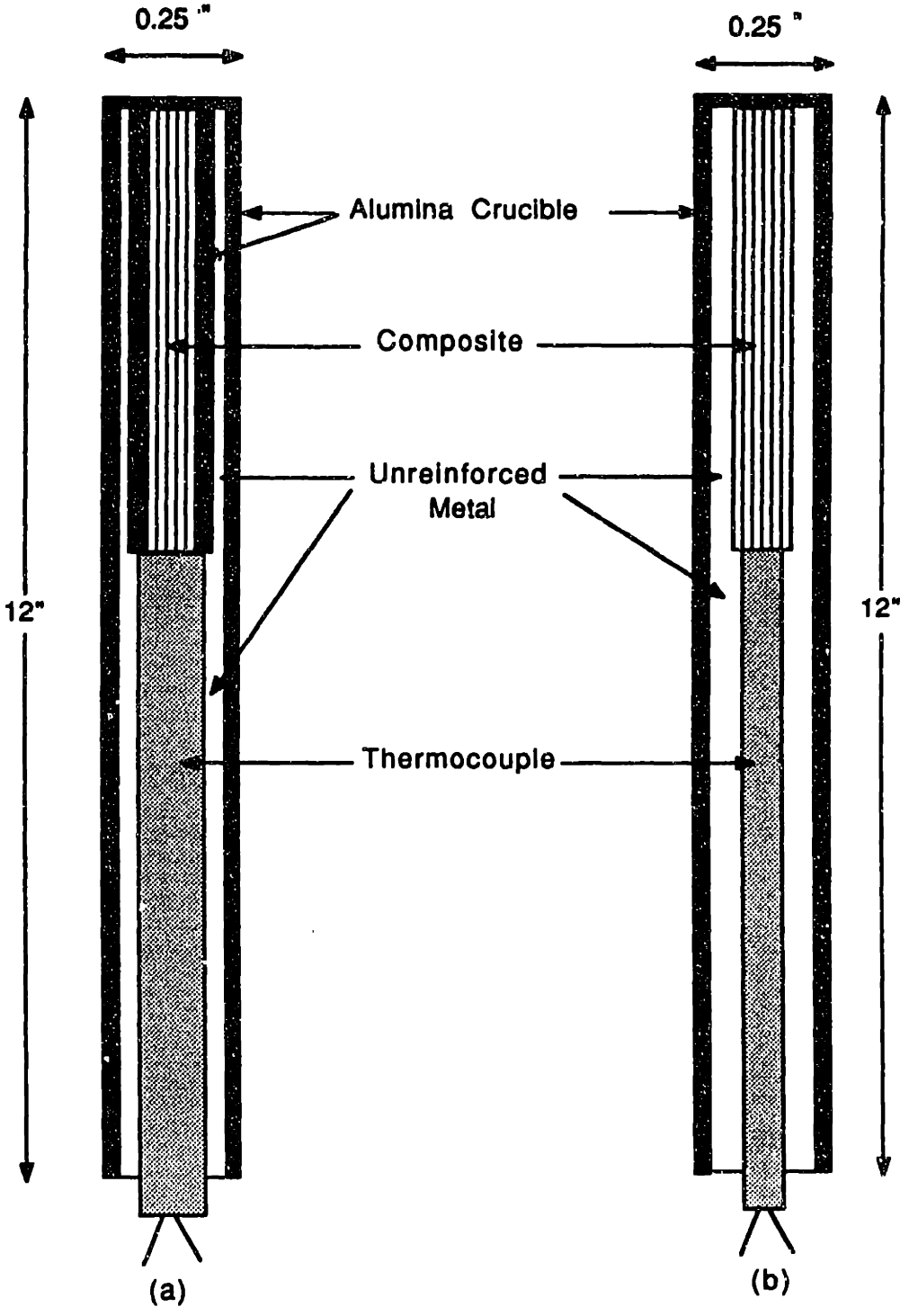

Figure 4.2 Cross section through hybrid or "composite" sample used for directional solidification experiments. A central reinforced region is surrounded by unreinforced material with the composite's matrix composition. (a) earlier version, (b) later version, without inner crucible separating unreinforced and composite regions. Scale markers are given. For clarity, however, vertical and horizontal scales differ.

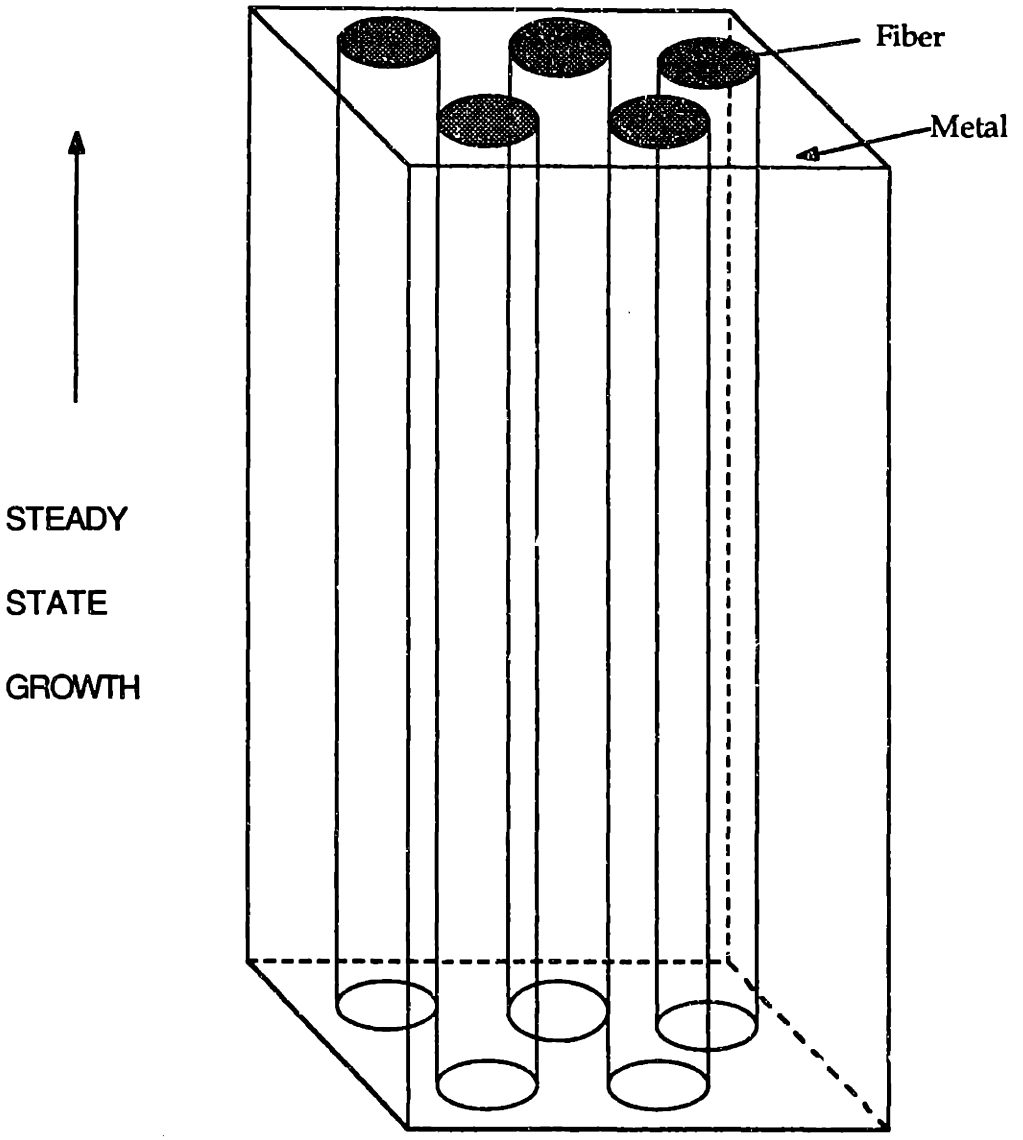

Figure 4.3 Schematic illustration of solidification direction within interstices of an aligned, fibrous composite.

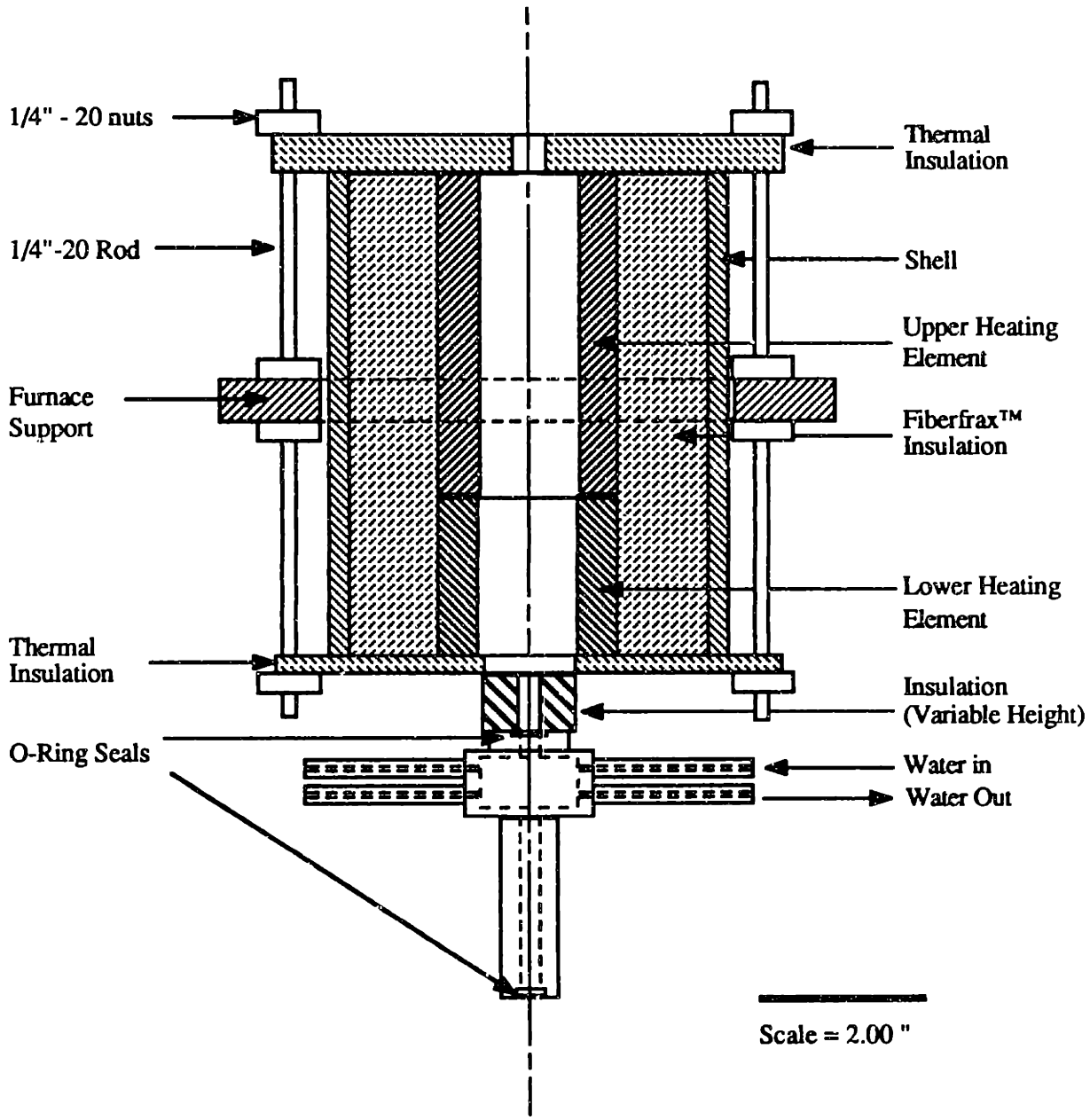

Figure 4.4 Crossectional cut through Bridgman furnace, described in text.

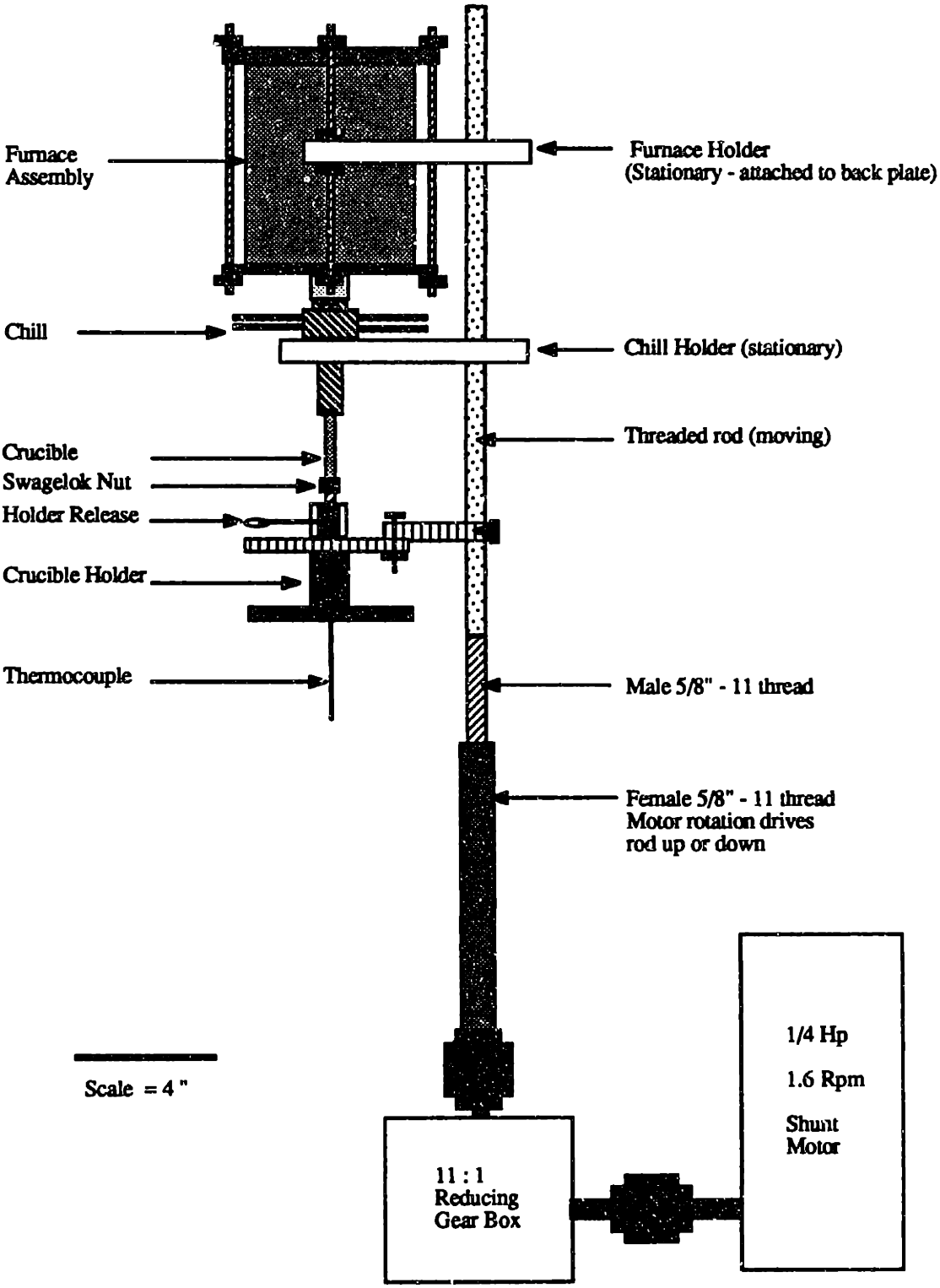

Figure 4.5 Schematic of directional solidification apparatus.

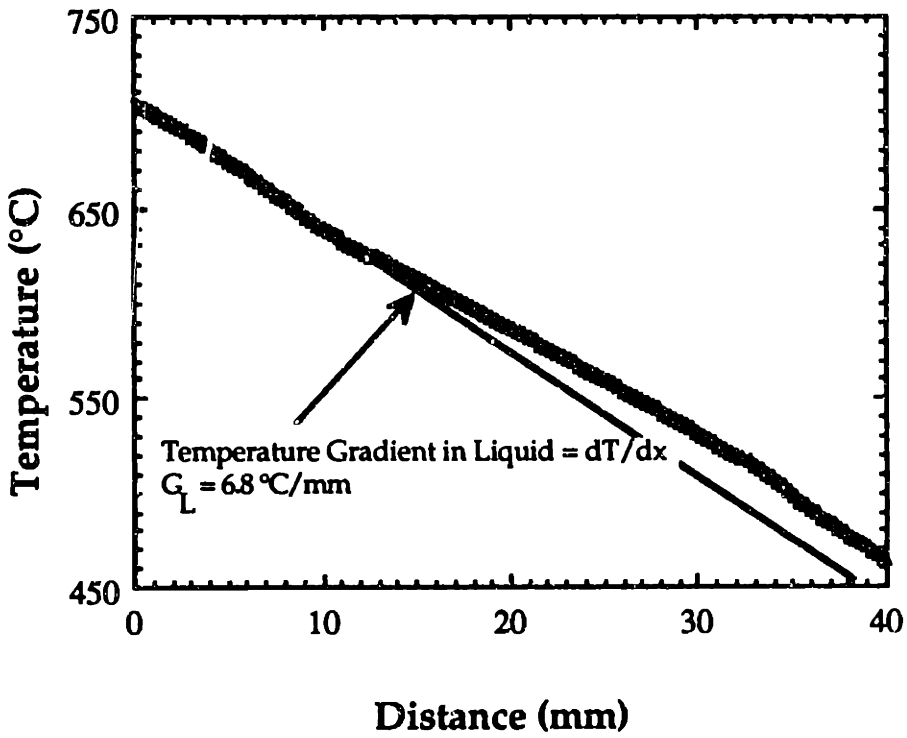

Figure 4.6 Typical temperature profile used to determine the thermal gradients during directional solidification. Temperature gradient, G_L, is the slope of temperature versus distance plots in the liquid at the liquid-solid interface. (Sample 216, G_L = 6800 K/m). At the liquid-solid interface there is a change in slope as the thermal conductivities of the two phases are unequal.

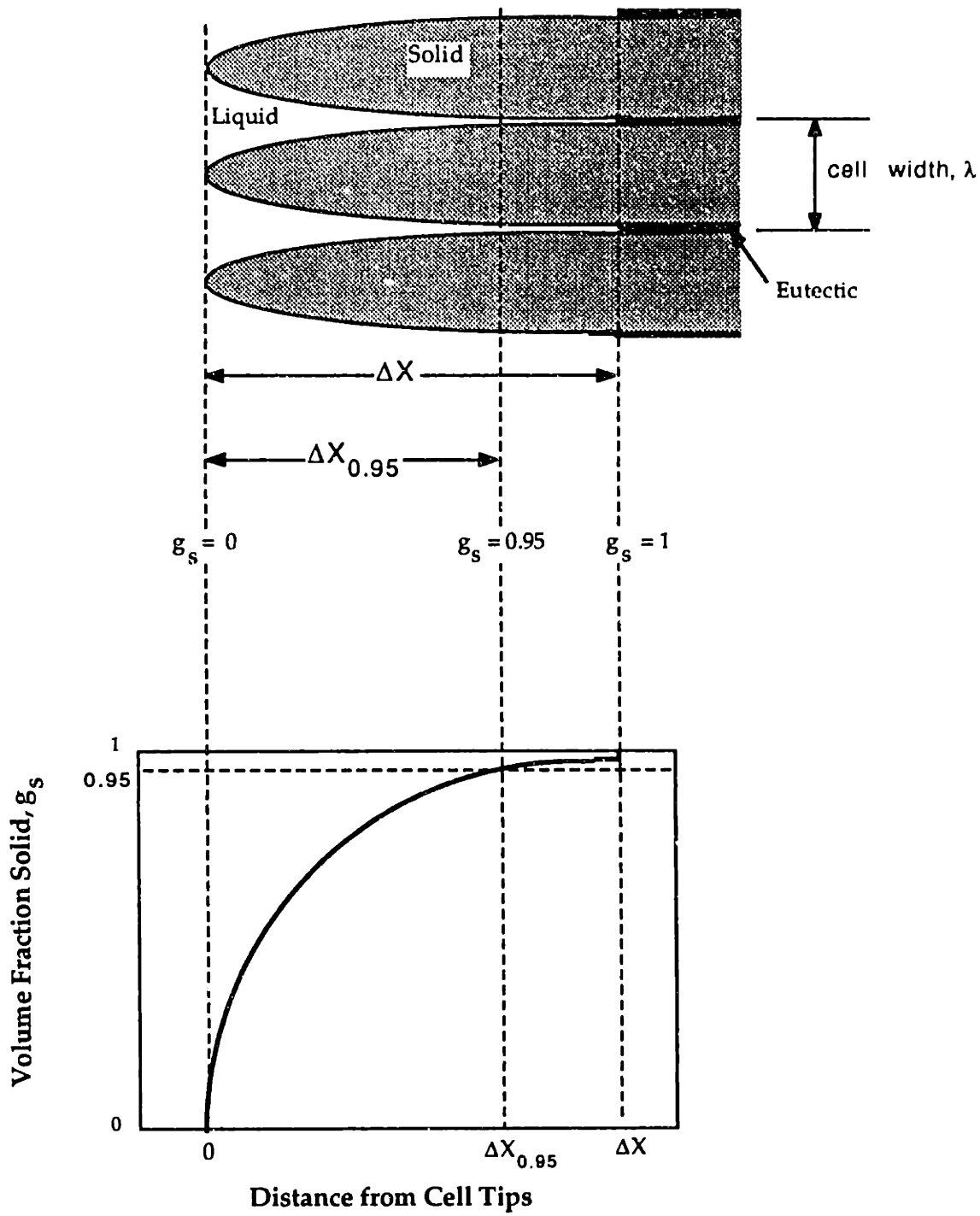

Figure 4.7 Measurement of fraction solid versus distance from cell tips. The distance for 95% volume percent solid, $\Delta X_{0.95}$ is also schematically shown. If a eutectic front is present, ΔX, the distance from the cell tips at which the material is fully solid, is easily determined. Cell width, λ, is also shown.

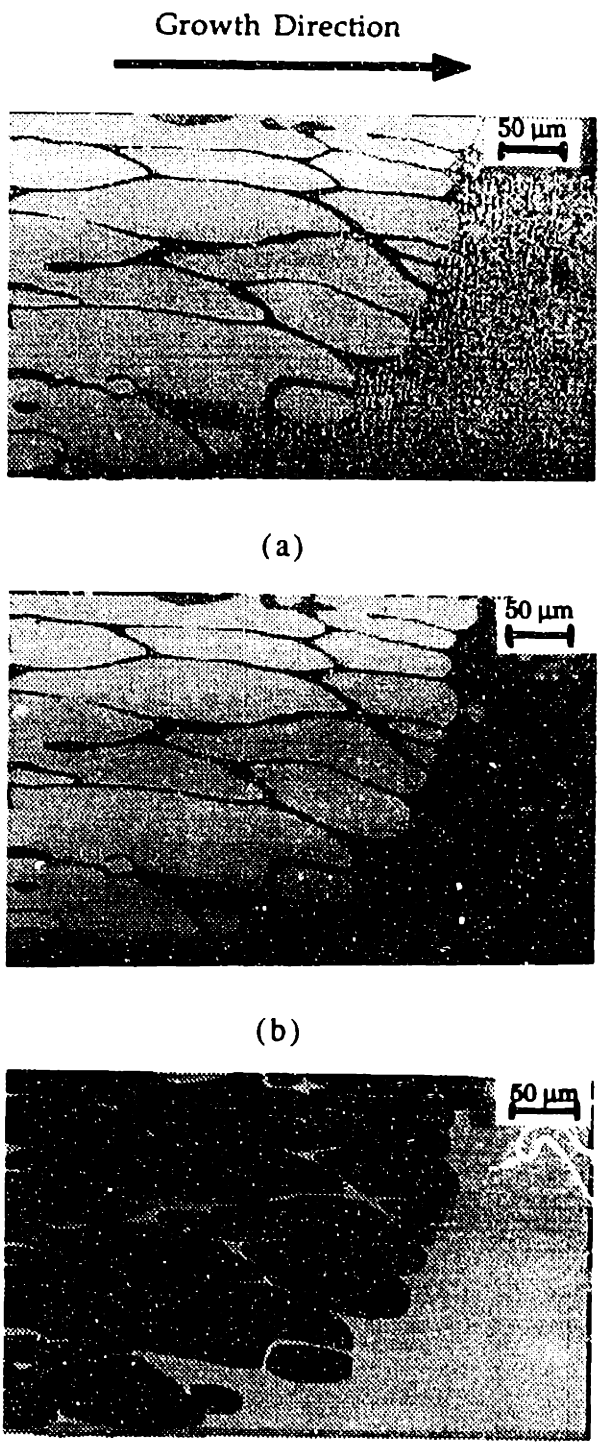

Figure 4.8 Image processing sequence. a). original image. b). dendrite arms in quenched liquid "closed off". c) solid and liquid portions are uniformly colored. The number of light and dark pixels in vertical bands, which correspond to isotherms, are counted. Sample 209.

Chapter 5

Experimental Results

5.1 Al - 4.5% Cu / Fiber FP™

Solidification parameters for all Al - 4.5% Cu / Fiber FP™ samples are given in Table 5.1. Average cell spacings in the unreinforced portions of the samples are also given in this table along with the measured volume fraction eutectic in the unreinforced and reinforced sections. Longitudinal metallographic cross sections for Samples 202, 207 and 210 are given in Figures 5.1 - 5.3. While the fibers are parallel and continuous, the longitudinal metallographic section does not coincide with the fiber axes, but rather cuts the fibers at an angle, causing them to appear as elongated ovals.

Measured plots of g_s versus distance from the liquid-solid interface are given in Figures 5.4 - 5.7. Where eutectic was found, the eutectic temperature isotherm could be detected metallographically in several samples as the transition from a coarse lamellar or divorced structure (formed during slow growth) to a very fine lamellar structure (solidified during the quench), an example of which is shown in Figure 5.8. This allowed computation of the full cell height, ΔX, in the unreinforced portion of Samples 207 to 219, as reported in Table 5.1. Within the remaining samples, which were apparently fully solid prior to the eutectic temperature, the distance from the cell tips at which theta phase disappears on the metallographic section is reported as the true cell height. Because of the lower precision in the location of $g_s = 1$ in the absence of eutectic formation, ΔX has a greater uncertainty for these samples.

Compared to the unreinforced metal, the volume fraction solid increases more rapidly in the composite, and then approaches 1 gradually. Measurement of ΔX was deemed too imprecise, so cell height was characterized with $\Delta X_{0.95}$, the distance from the cell tips at which 0.95 volume fraction solid was reached, instead. This value was determined by the distance from the cell tips at which a best fit line drawn through the experimental points crossed the $g_s = 0.95$ threshold. $\Delta X_{0.95}$ is reported for all unreinforced samples as well in Table 5.1 as well. As there is scatter in volume fraction solid versus distance plots, there is an uncertainty in the measurement of $\Delta X_{0.95}$. The distance from the interface at which an experimental g_s was greater than 0.95 and the distance at which the last point was less than 0.95 was measured. Deviation for all samples in each class (eg Al - 4.5 % Cu /FP) were averaged and compared to the average $\Delta X_{0.95}$ to get the percentage error in the measurements. Since the liquid film surrounding each solid cell often becomes discontinuous the fraction solid increases, apparent volume fraction solid can approach one in several of the narrow bands used in point counting, while the actual volume fraction solid is significantly less. This problem is minimized by making measurments over a large number of cells, however this was not possible for many of the experimental samples. Thus the possible error in $\Delta X_{0.95}$ is not symmetric, since the first appearance of a point with $g_s > 0.95$ is further from the value obtained by curve fitting than is the last point for which $g_s < 0.95$. The average percentage error in $\Delta X_{0.95}$ was approximately equal for all samples. The average values for the error are $\Delta X_{0.95}$ (-41%, + 15%).

In the composites, the primary phase was observed to grow from within the interfiber interstices toward the fibers. Near the fiber surface, where a triple point of solid and liquid matrix and fiber was found, the contact angle θ

of the solid against the fiber measured through the solid metal was greater than 90 °, as shown in Figure 5.9. Toward the end of solidification, where g_s approaches 1, remaining liquid was found to be situated as pendular rings between contacting fibers.

No eutectic was found in the matrix of any fully solidified composite samples. The etchant consisting of 4g $KMnO_4$ and 2g NaOH in water, which revealed equiconcentration contours in the unreinforced matrix, produced no contrast in the matrix of the composites. To ascertain that, as in refs. [74, 82], this corresponds to an absence of microsegregation in the matrix of the composites, matrix composition profiles across interfiber interstices within Samples 209 and 218 were measured using the electron microprobe, to yield the curves given in Figures 5.10 - 5.11. Model predictions of the composition profiles for these interstices are also shown on these plots.

Table 5.1
Experimental Results of Aluminum 4.5% Copper/FP™ experiments

Sample	G (K/m)	V (μm/s)	Unreinforced				Composite	
			Cell Spacing (μm)	$\Delta X_{0.95}$ (μm)	ΔX (μm)	$g_{eutectic}$	$\Delta X_{0.95}$ (μm)	$g_{eutectic}$
201	14000	0.84	Planar	0	0	0	35	0
202	14000	1.15	Planar	0	0	0	50	0
203	13300	1.58	64	2260	2500	0	260	0
204	17600	1.21	153	200	300	0	30	0
205	16500	2.07	99	1200	1700	0	960	0
207	17400	2.69	126	3160	3500	0.029	520	0
209	21300	3.4	95	2900	4000	0.019	1220	0
210	19000	4.15	88	4500	4500	0.080	1260	0
211	17000	2.84	162	3300	3900	0.038	1060	0
212	9800	1.51	286	4500	5200	0.038	350	0
214	6500	1.62	204	–	13200	0.021	770	0
215	8000	1.95	174	10600	11000	0.040	*	–
216	6800	2.50	140	5600	14400	0.011	2500	0
217	13000	2.50	113	4500	6500	0.014	*	–
218	6200	2.08	137	7260	13100	0.005	2900	0
219	8600	2.19	113	8840	11200	0.002	3080	0

* No reinforced area in this sample.

5.2 Al - 1.0% Cu / Fiber FP™

Microstructures in these samples were qualitatively similar to those found with Al -4.5 wt % Cu matrix composites, except that no eutectic was found in the fully solidified portions of any of these samples. Typical microstructures are given in Figures 5.12 - 5.14; experimental parameters and measured variables are reported for these samples in Table 5.2. Examples of primary solid fraction in the quenched samples as a function of distance behind the cell tips are given in Figure 5.15.

5.3 Determination of Equivalent Interstice Radii

Because the fibers were packed using the same procedure with all samples, the fiber distribution was assumed to be equivalent for all samples. The average cell radius in the composite region of three samples, 210, 214 and 218, was measured from transverse metallographic sections through a partially solid region and computed using equation (4.1). An example of such a transverse section is given in Fig. 5.16, in which material that was liquid prior to the quench delineates each cell. Table 5.3 gives the measured equivalent cell radii, for three different locations within samples 210, 214 and 218. The average cell, or interstice radii are similar for all three samples. Differences in measurements within each sample are due to inhomogeneous fiber distribution. The average equivalent interstice diameter of 25 μm was used for all samples.

Table 5.2
Experimental Results of Aluminum 1.0% Copper/FP™ experiments

Sample	G (K/m)	V (μm/s)	Unreinforced Cell Spacing (μm)	Unreinforced $\Delta X_{0.95}$ (μm)	Composite $\Delta X_{0.95}$ (μm)
401	15000	5.3	178	420	30
402	15400	3.0	Planar	0	75
403	15900	6.3	80	750	300
404	12600	7.9	92	1030	200
405	5200	4.9	191	1150	100
406	5000	4.2	229	500	120
407	5000	7.7	84	*	*
408	8500	3.1	Planar	0	120
409	7900	5.9	175	900	580
411	6000	12.0	119	1350	750
412	5200	10.4	125	1540	650
413	5500	18.8	129	1730	810
414	7400	11.6	99	1500	760
415	7250	16.7	83	2070	830
417	8300	21.0	75	1700	900
418	14800	13.2	81	1200	500
419	15000	10.5	105	1130	400

* Poor sample quench. Measurement was not made.

Table 5.3

Measurement of Equivalent Cell Radii

Sample	V_{fibers}	# fibers	#cells	$r_{interstice}$ (μm)
210	0.62	42	20	11.8
210	0.62	44	24	10.5
210	0.53	38	15	14.9
214	0.57	40	17	13.3
214	0.54	38	20	12.7
214	0.61	43	19	12.0
218	0.66	46	19	11.1
218	0.57	40	17	13.3
218	0.50	35	13	15.1
Average Interstice Radius				12.7
Standard Deviation				1.6

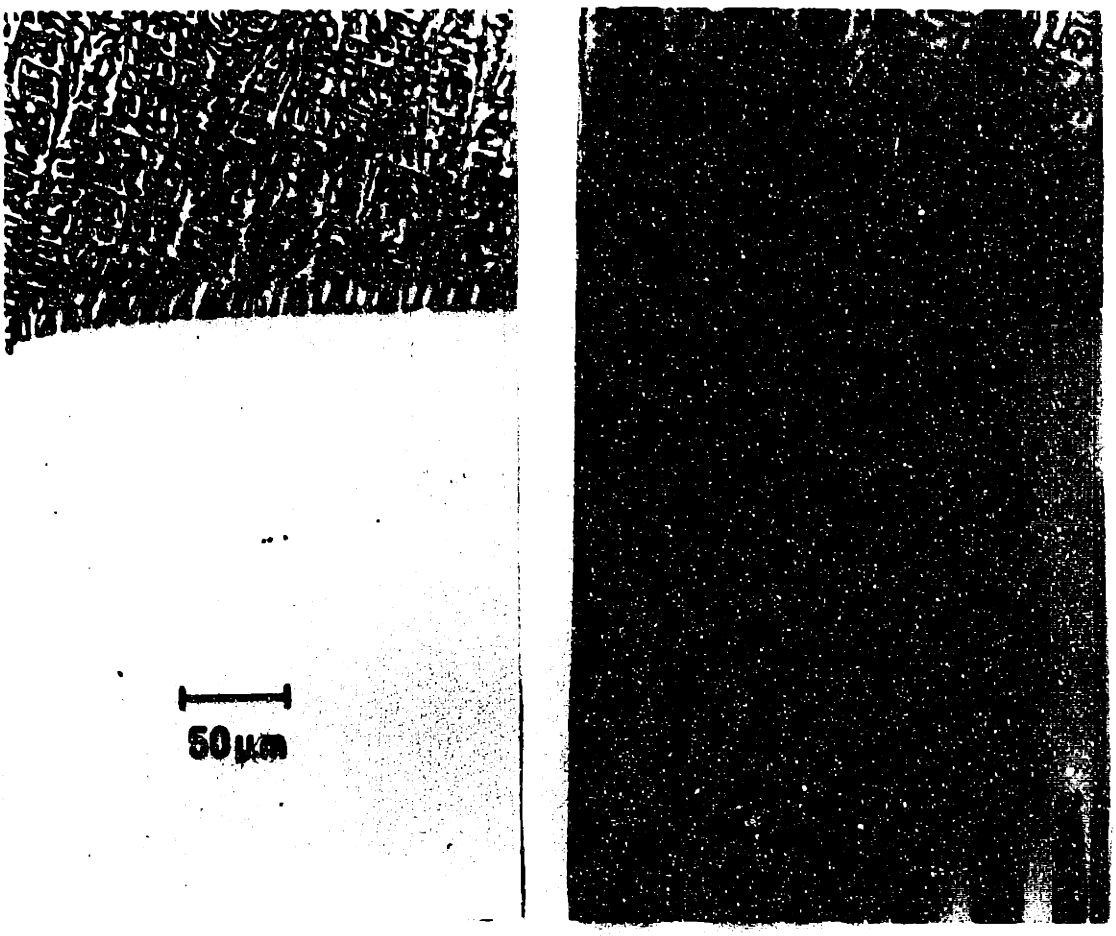

Figure 5.1 Longitudinal section through quenched liquid-solid interface of sample 201. G = 14000 K/m, V = 1.15 µm/s, Al - 4.5 wt% Cu. a). unreinforced region, which exhibits a planar interface morphology. b). composite.

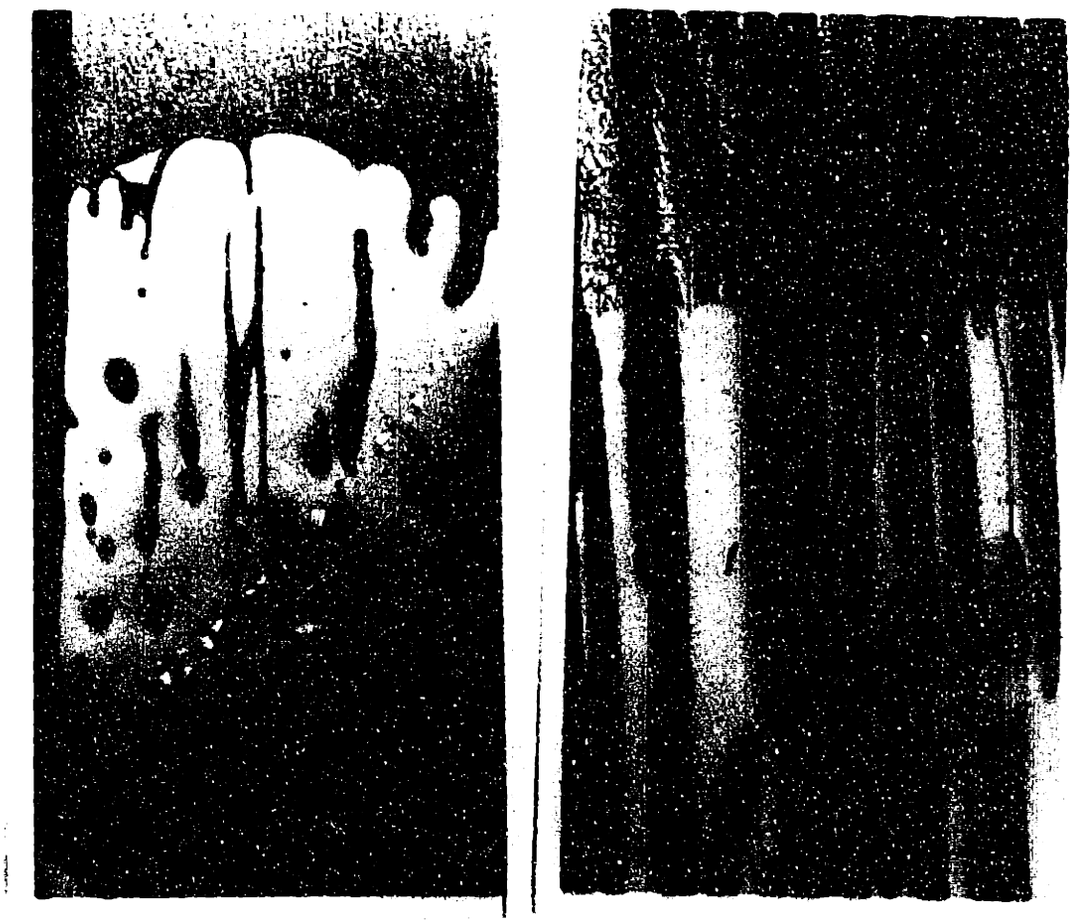

Figure 5.2 Longitudinal section through quenched liquid-solid interface of sample 207. G = 17400 K/m, V = 2.69 μm/s, Al - 4.5 wt% Cu. a). unreinforced region, which exhibits a cellular interface morphology. b). composite. Note that interface morphology in the composite is similar to that shown in Figure 5.1.

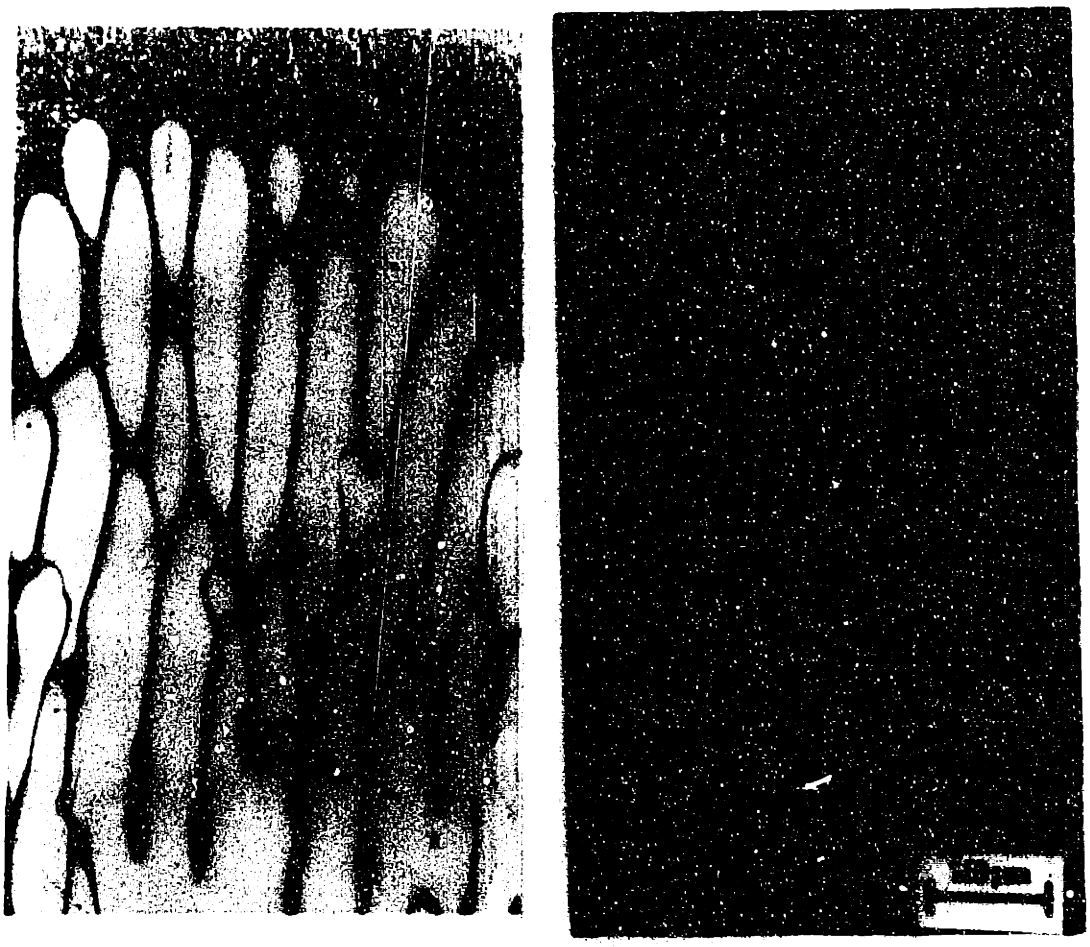

Figure 5.3 Longitudinal section through quenched liquid-solid interface of sample 210. G = 19000 K/m, V = 4.15 μm/s, Al - 4.5 wt% Cu. a). unreinforced region, which exhibits a cellular interface morphology. b). composite. Note that interface character in the composite has changed from figure 5.2, while the unreinforced morphologies are similar in character.

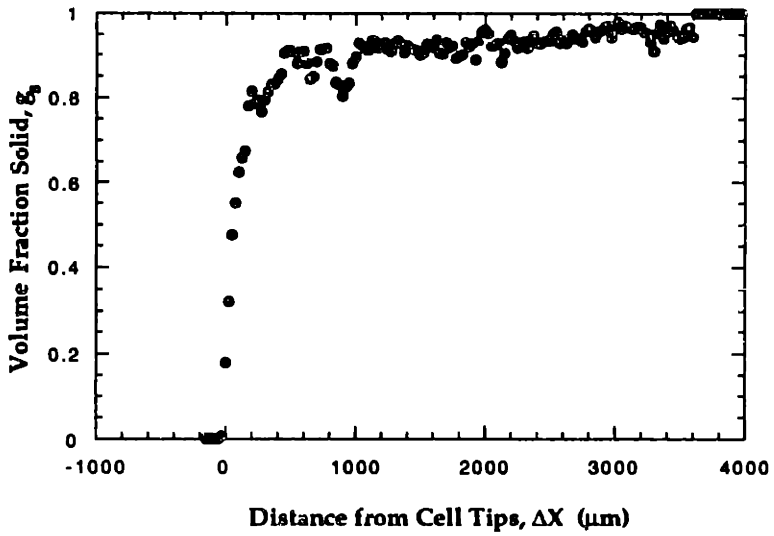

(a)

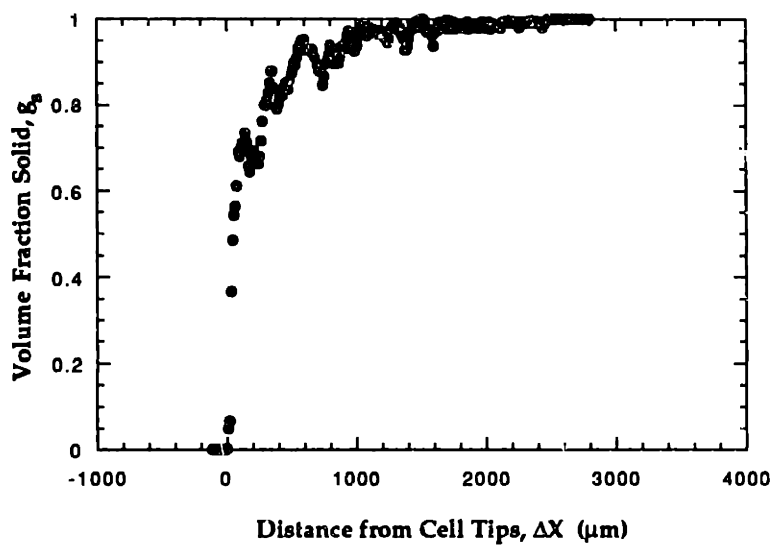

(b)

Figure 5.4 Volume fraction primary solid versus distance from liquid-solid interface for sample 209: G = 21300 K/m, V = 3.4 μm/s, λ_{cell} = 95μm. (a) unreinforced (b) composite. Measurements for both unreinforced and composite sections were made using the automated image processing method.

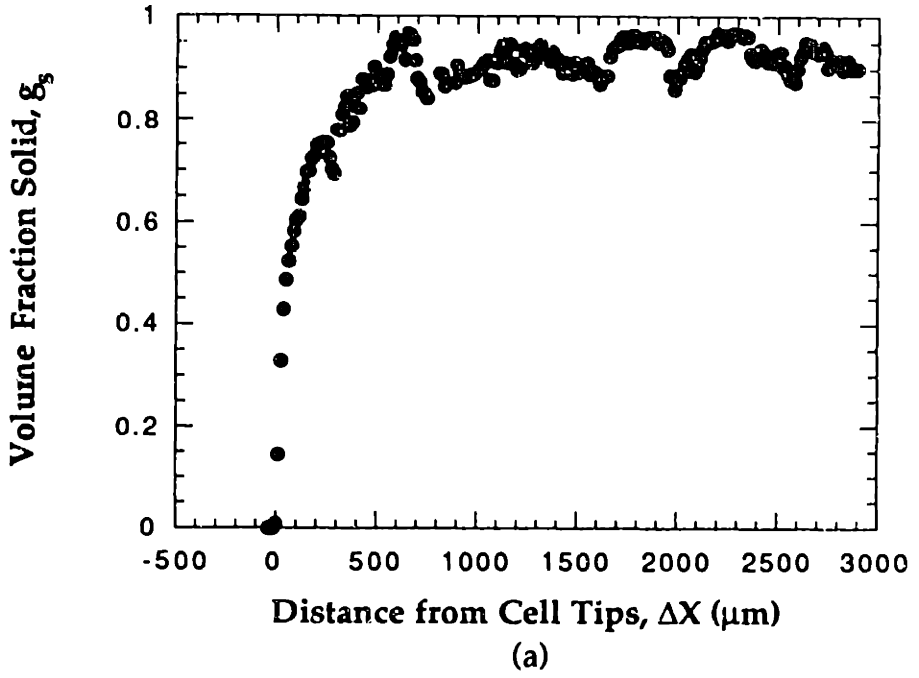

(a)

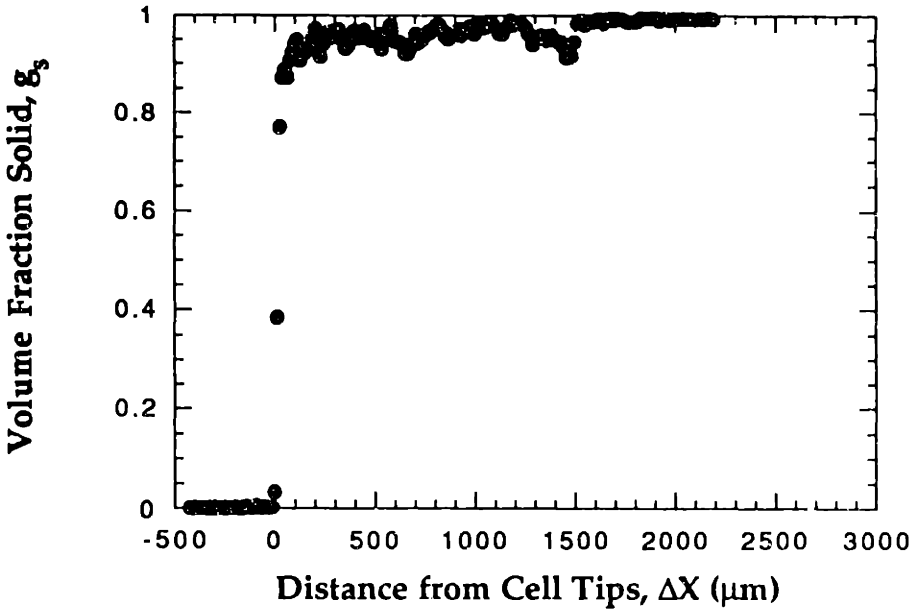

(b)

Figure 5.5 Volume fraction primary solid versus distance from liquid-solid interface for sample 211: G = 17000 K/m, V = 2.84μm/s, λ_{cell} = 162 μm. (a) unreinforced (b) composite. Measurements for both unreinforced and composite sections were made using the automated image processing method.

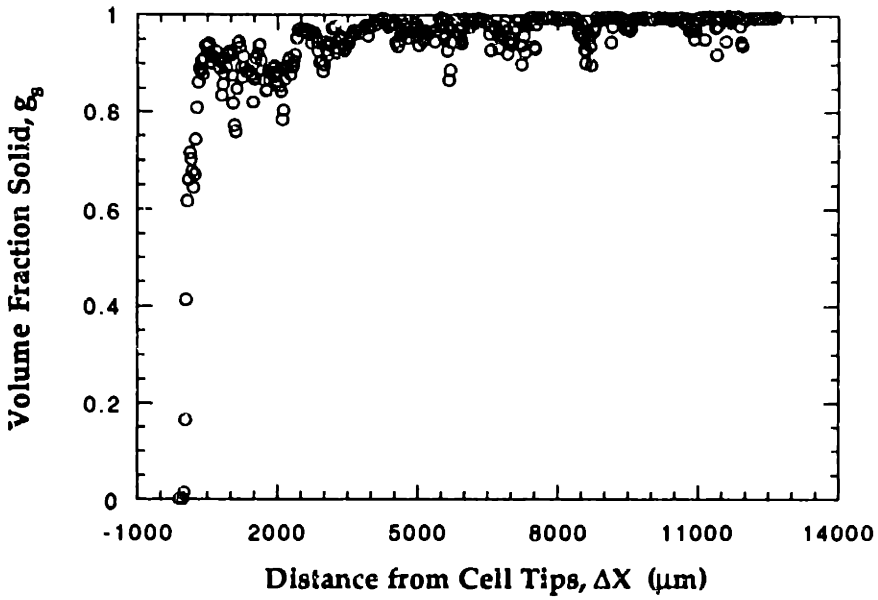

(a)

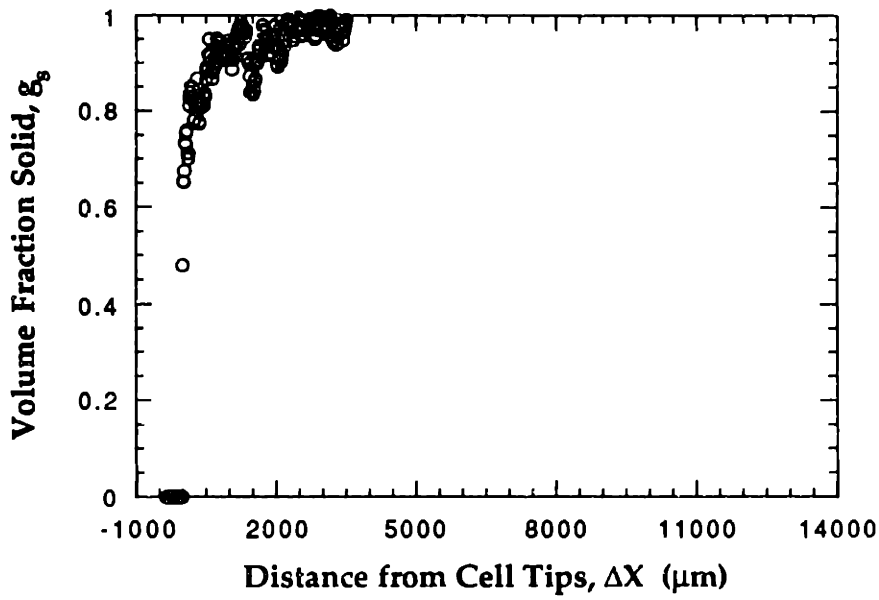

(b)

Figure 5.6 Volume fraction primary solid versus distance from liquid-solid interface for sample 216: G = 6800 K/m, V = 2.5 μm/s, λ_{cell} = 140 μm. (a) unreinforced (b) composite. Measurements for both unreinforced and composite sections were made using the automated image processing method.

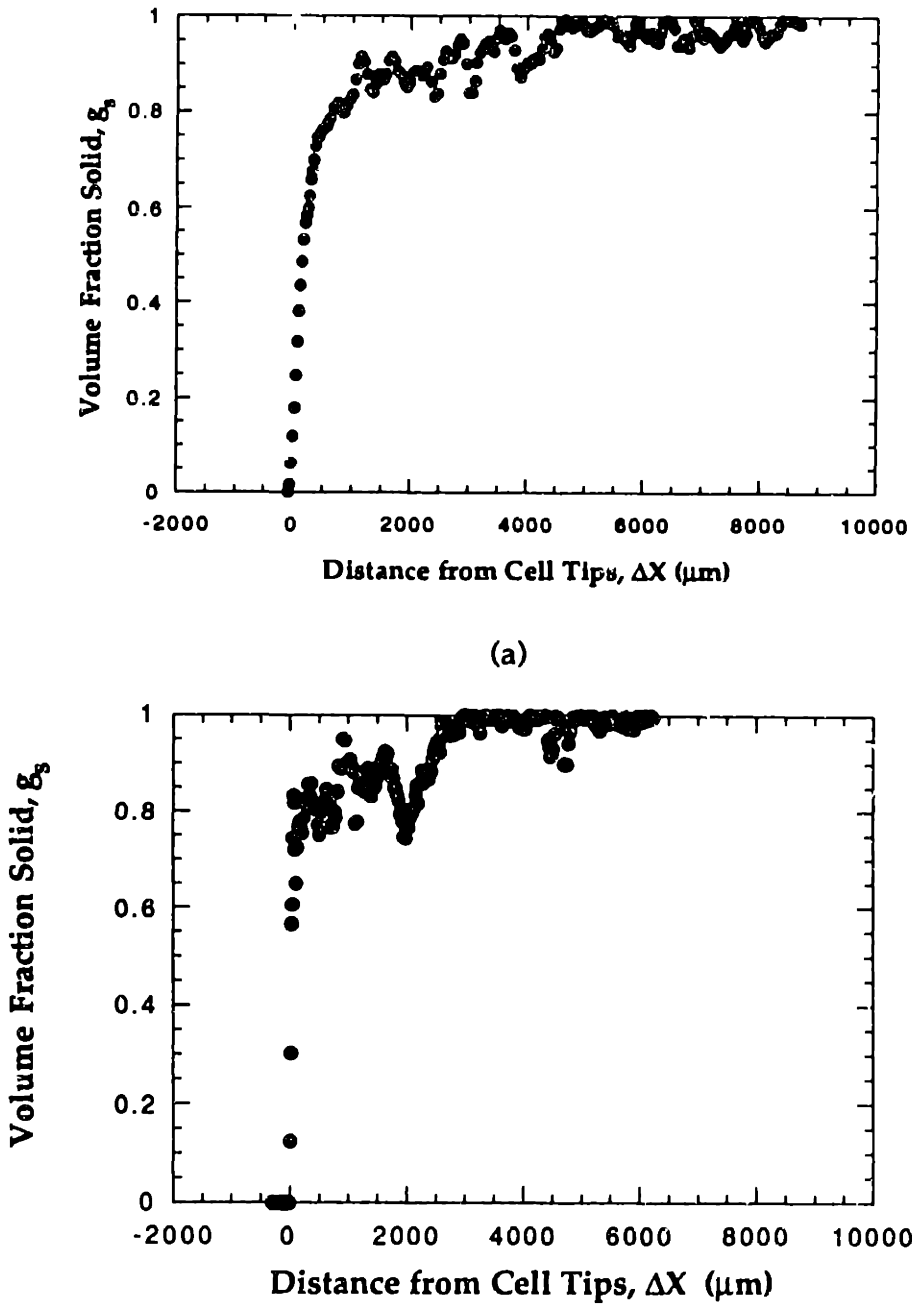

Figure 5.7 Volume fraction primary solid versus distance from liquid-solid interface for sample 218: G = 6200 K/m, V = 2.08 μm/s, λ_{cell} = 137 μm. (a) unreinforced (b) composite. Measurements for both unreinforced and composite sections were made using the automated image processing method.

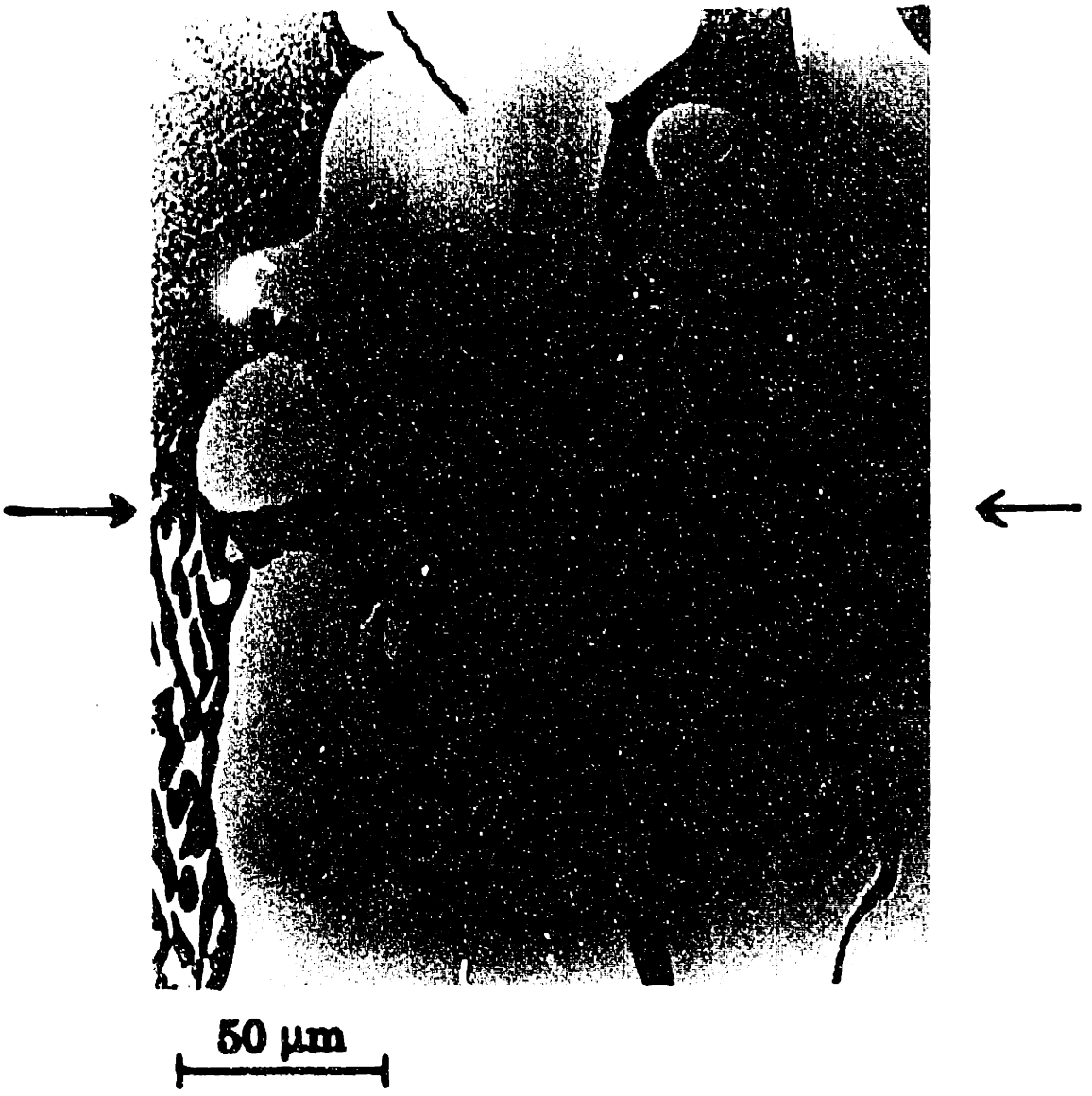

Figure 5.8 Microstructural transition from coarse eutectic formed during slow directional growth to very fine lamellar structure formed upon quenching. Sample 210. The eutectic front is marked by arrows.

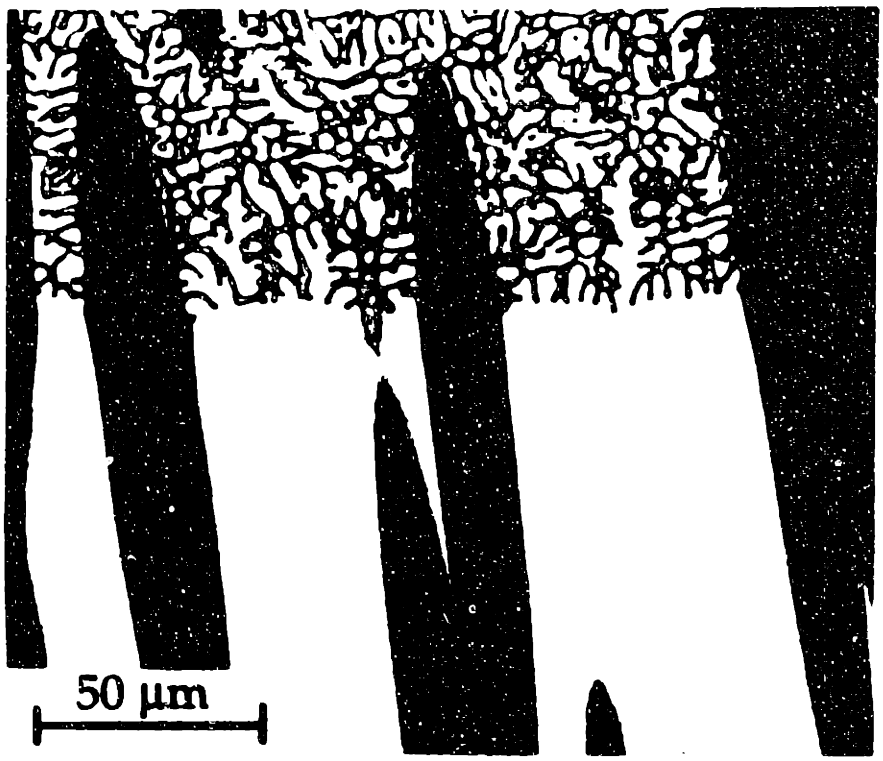

(a)

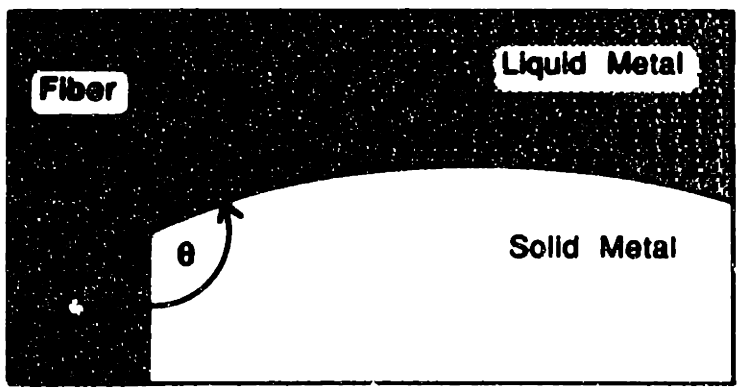

(b)

Figure 5.9 (a) Liquid-solid reinforcement triple point in composite. The contact angle, which is defined by the macroscopic curvature of the interface near the reinforcement (as shown in (b)), not the intruding liquid which may be a quench artifact, is greater than 90°. Sample 207.

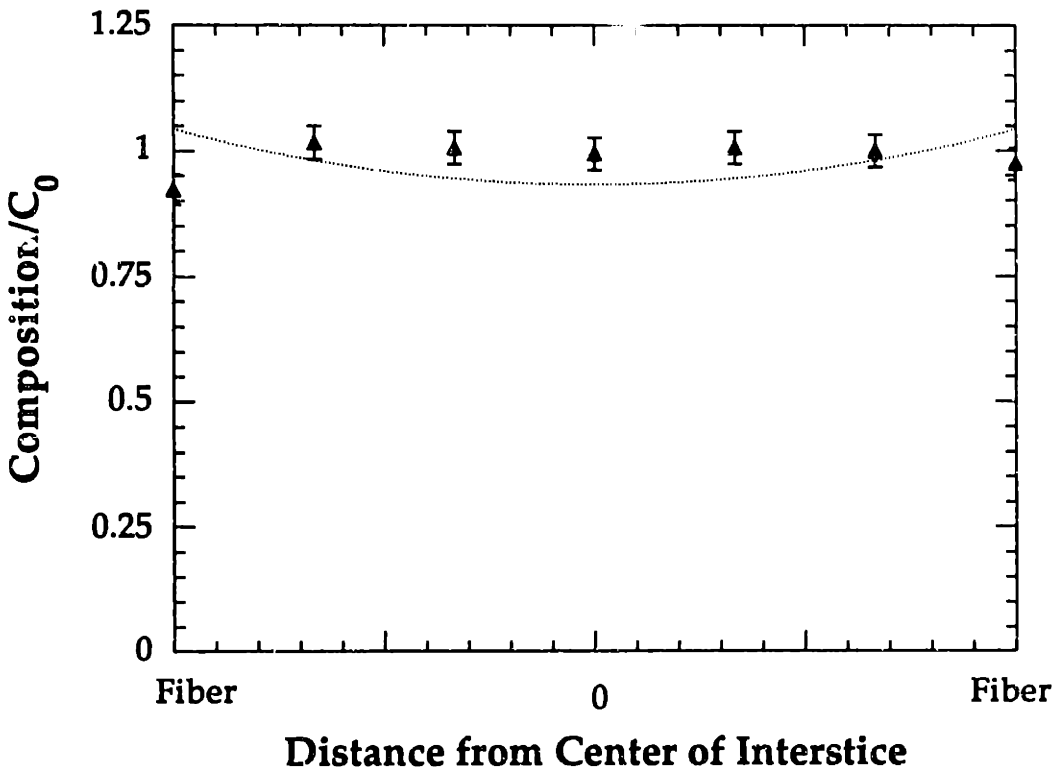

Figure 5.10 Compositional variation across an interstice in transverse section of fully solidified sample 209, determined from a microprobe trace. Composition is normalized by the average composition, and distances are given from the center of the interstice. Finite-difference model prediction for an interstice of this size is also shown.

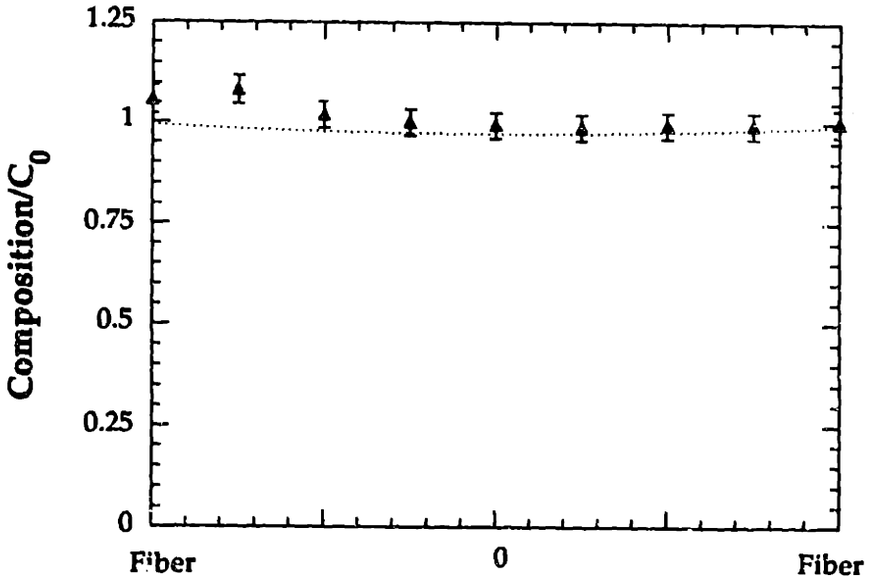

(a)

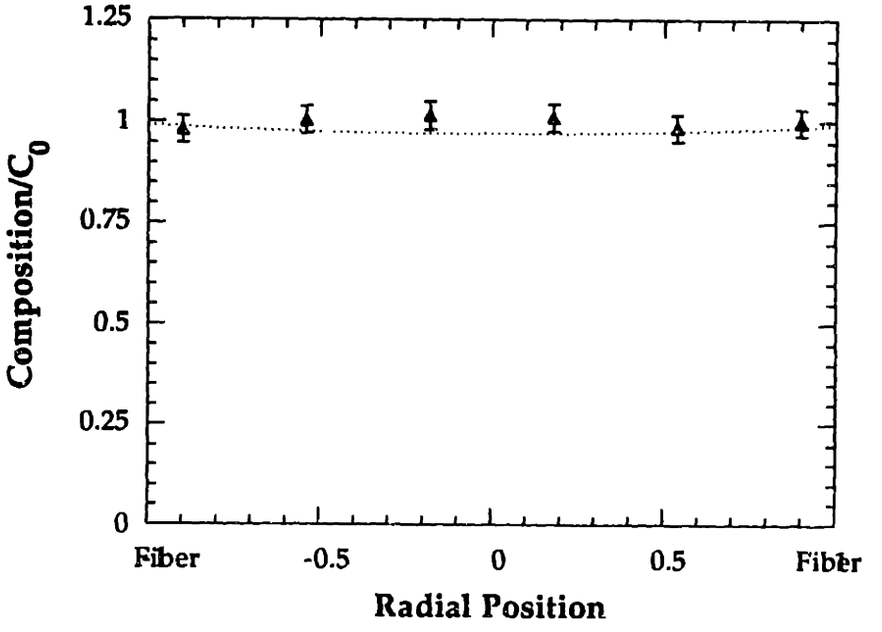

(b)

Figure 5.11 Compositional variations across two interstices in transverse section of fully solidified Al - 4.5 wt% Cu, sample 218, determined from microprobe traces. Composition is normalized by the average composition, and distances are given from the center of the interstice. Finite-difference model predictions for these interstices are also shown.

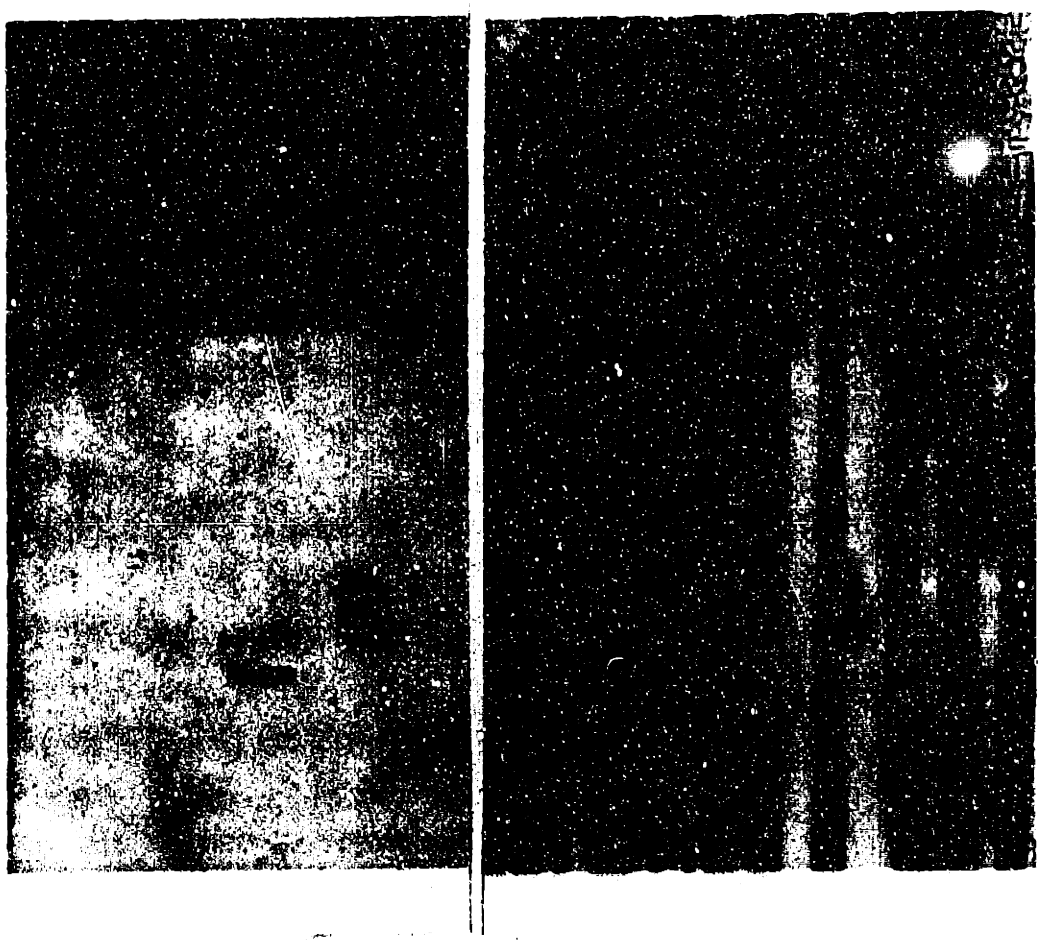

(a) (b)

Figure 5.12 Longitudinal section through quenched liquid-solid interface of sample 402, G = 15400 K/m, V = 3.0 μm/s, Al - 1.0wt% Cu. a). unreinforced region, which exhibits a planar interface morphology. b). composite.

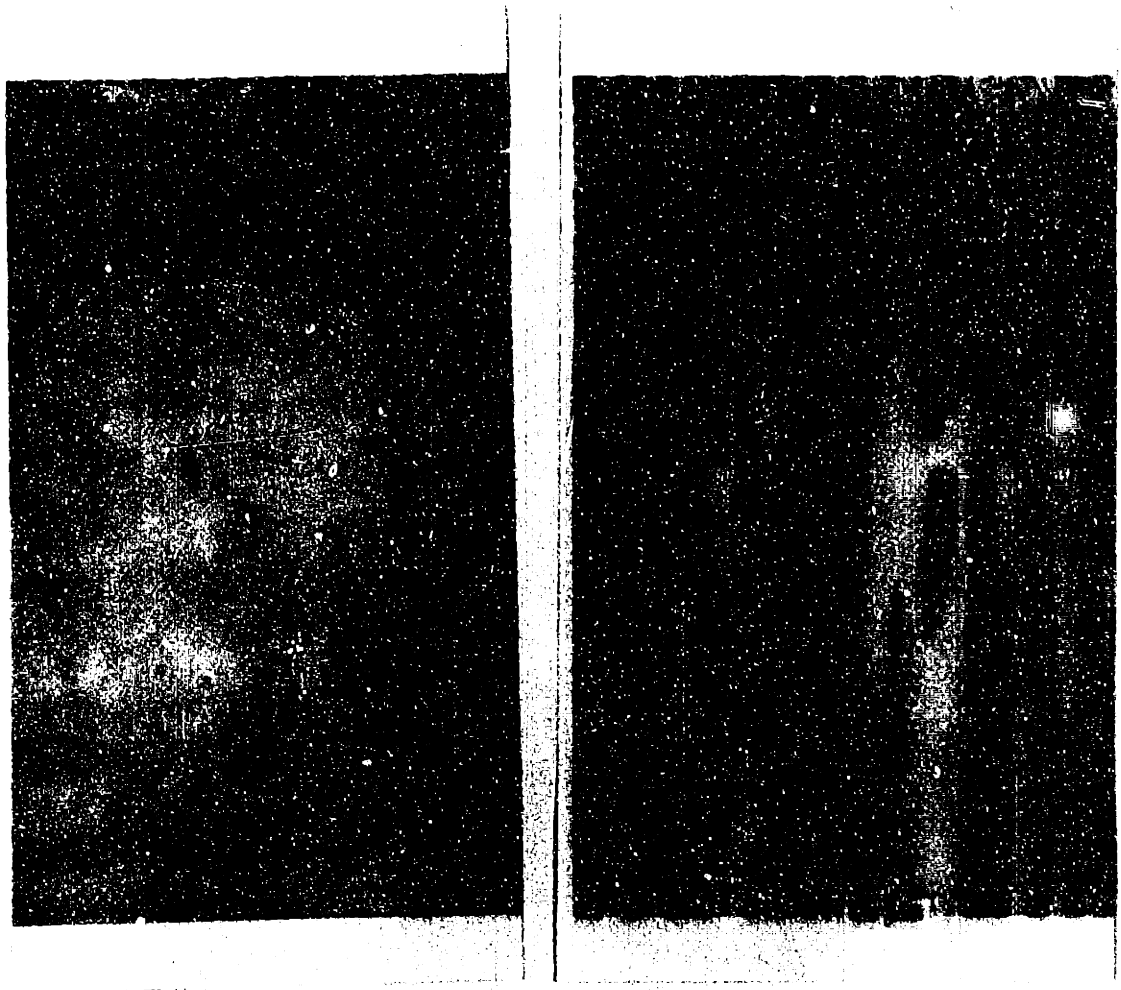

Figure 5.13 Longitudinal section through quenched liquid-solid interface of sample 401, G = 15000 K/m, V = 5.3 μm/s, Al - 1.0wt% Cu. a). unreinforced region, which exhibits a cellular interface morphology. b) composite. Note that composite interface morphology is similar to that in Figure 5.12.

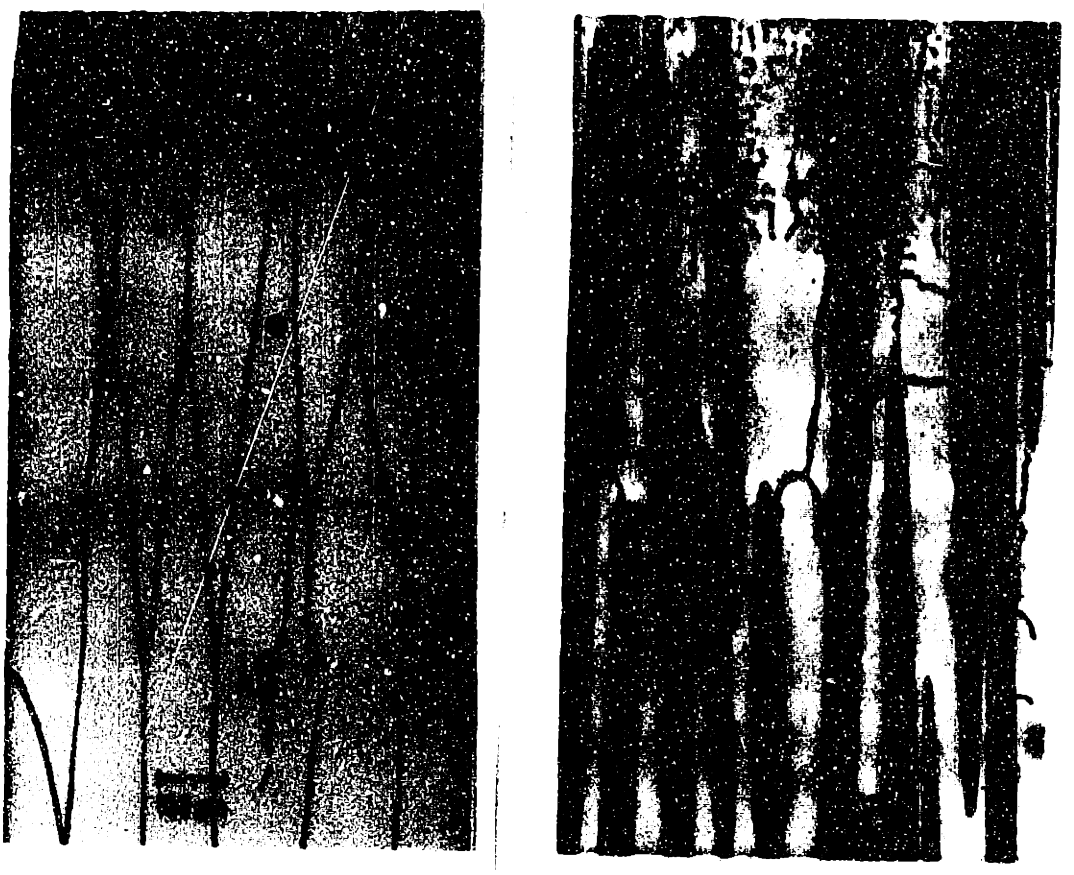

Figure 5.14 Longitudinal section through quenched liquid-solid interface of sample 411. G = 6000 K/m, V = 12.0 μm/s, Al - 1.0wt% Cu. a). unreinforced gion, which exhibits a cellular interface morphology. b). composite. Note that interface character in the composite has changed from figure 5.13, while the unreinforced morphologies are similar in character.

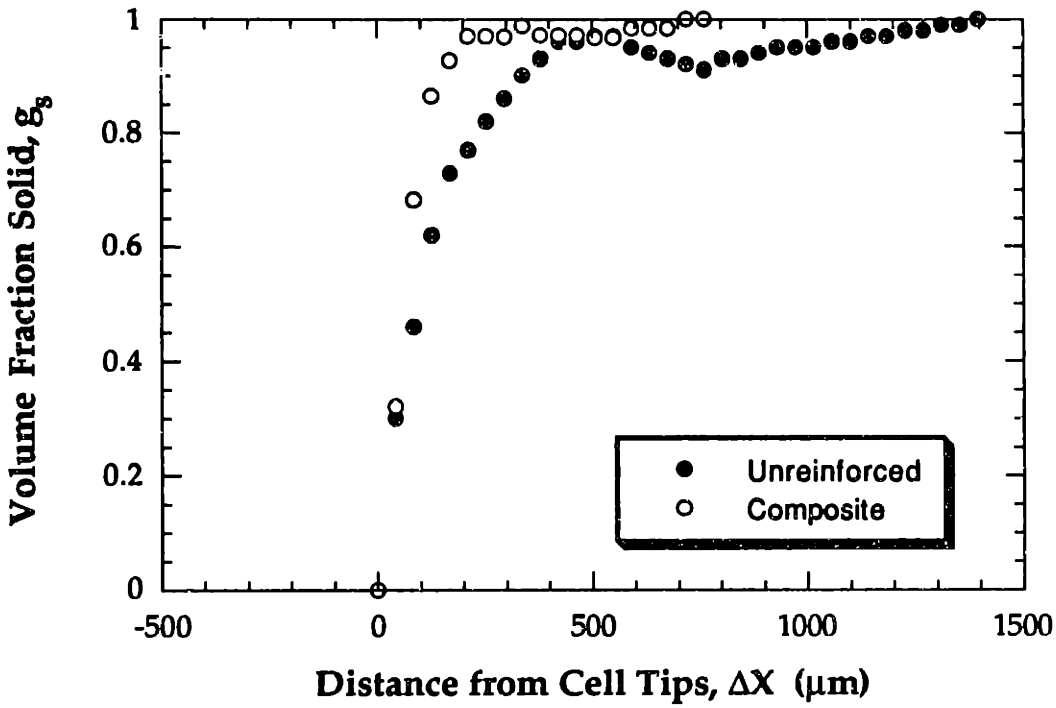

Figure 5.15 Volume fraction primary solid versus distance from liquid-solid interface. Unreinforced and composite data are superimposed. Sample 404, G = 12600 K/m, V = 7.9 μm/s, λ_{cell} = 92 μm.

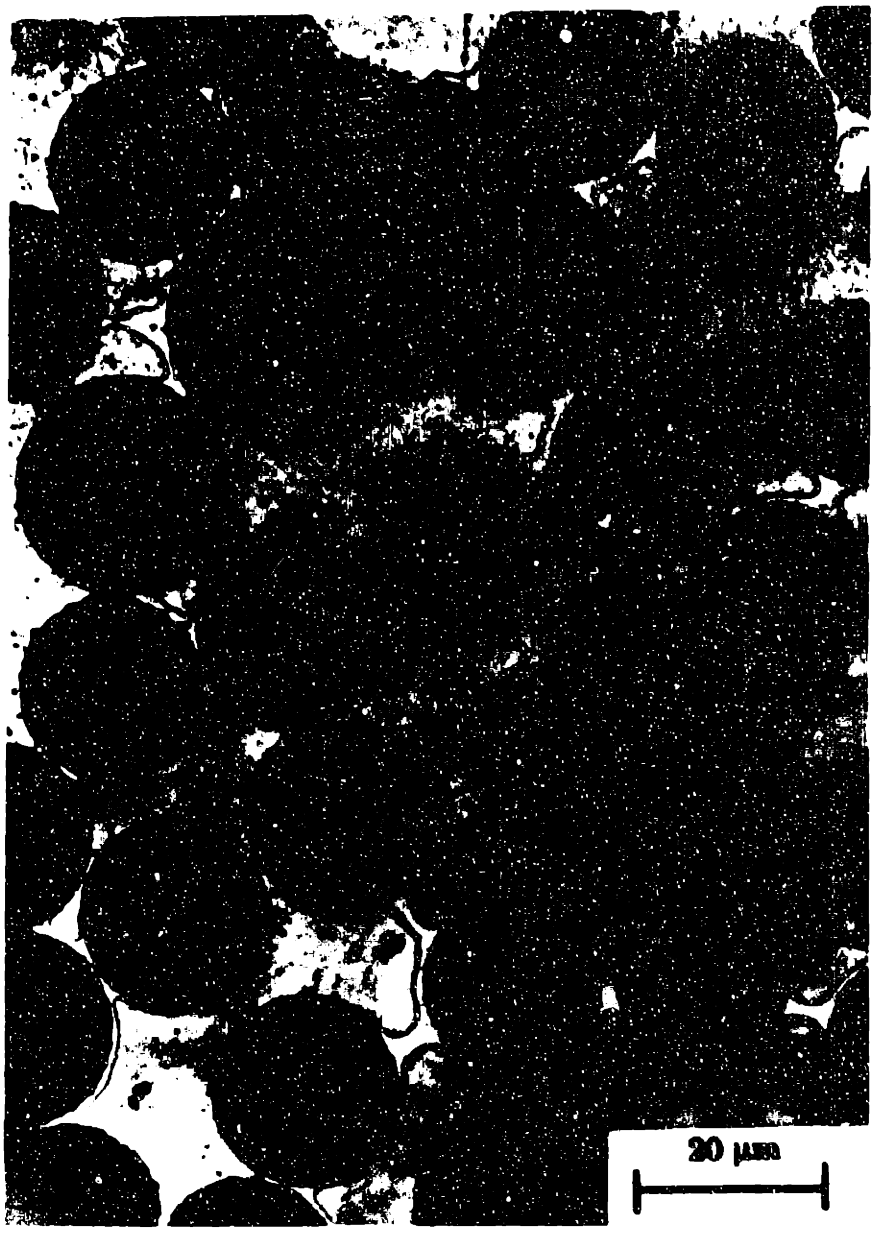

Figure 5.16 Transverse section through partially solidified Al - 4.5 wt% Cu/ Fiber FP™ composite, used to characterize average interstice diameter. Cells are delineated by a ring of liquid, which is light in color, or fiber surface. $KMnO_4$ and NaOH etchant. Sample 210.

Chapter 6

Discussion

It should be noted that unreinforced cell diameters, or spacings, listed in Table 5.1 are significantly larger than the average interstice diameter calculated in Table 5.3. As the unconstrained cell cannot be placed within an average interstice, the reinforcement geometrically constrains solidification of the composite matrix. The manifestation of this constraint on the solidification microstructure is the focus of this thesis. First, the solidification of the unreinforced material will be examined, and compared to conventional microstructure-processing relations. Then the effect of geometric constraint on matrix microsegregation and liquid-solid interface morphology will be examined.

6.1 Unreinforced Solidification

6.1.1 Interface Morphology

In characterizing interface morphologies in the unreinforced sections, a clear transition from planar to cellular solidification was observed: interfaces exhibiting corrugations, characteristic of cellular solidification fronts, were clearly discernible from plane fronts, which were completely devoid of corrugations. Figures 6.1 and 6.2 map observed interface morphologies of unreinforced sections in Al - 4.5% Cu and Al -1.0% Cu, respectively, as a function of G and V. From a best fit line separating planar and cellular growth conditions in aluminum 4.5% copper, plane front breakdown occurs at $G/V = 1.4 \times 10^{10}$ Ks/m^2 . Using thermophysical data given in Appendix B and the constitutional supercooling criterion, equation 2.3, this corresponds

to a liquid solute diffusion coefficient, $D_L = 5.1 \times 10^{-9}$ m²/s. In the aluminum - 1.0% copper alloy, the planar to cellular transition occurred at a $G/V = 2.9 \times 10^9$ Ks/m² , which corresponds to a liquid solute diffusion coefficient, $D_L = 5.5 \times 10^{-9}$ m²/s. These values are in general agreement with reported diffusion coefficients (Appendix B), and are used in subsequent calculations.

6.1.2 Cell Height

Table 6.1 compares values of cell height, ΔX, for aluminum 4.5% copper samples to calculated heights assuming the cell tips are at the temperature predicted by Bower, Brody and Flemings [54], (equation 2.13). In those samples which were fully solid prior to the eutectic temperature, the predicted cell root temperature was calculated with the numerical model developed in Chapter 3, which initially set cell tips at the BBF temperature. There is reasonable agreement between measured and calculated cell heights.

6.1.3 Volume Fraction Eutectic

A comparison of the measured volume fraction eutectic with that predicted by the cellular solidification model developed in Chapter 3, is given in Table 6.2. With the exception of sample 209 (possible sources of experimental error include uncertainty in the measurement of cell diameter or fraction eutectic since only a few cells were observed, and uncertainty in G. V and C_0), there is good agreement between the model predictions and experimental measurements. The fraction eutectic predicted by the finite difference model with no convection (i.e., assuming liquid and solid densities are equal) is also given in Table 6.2, showing that the calculated influence of intercellular liquid flow on microsegregation in cellular growth of Al-Cu is small. Comparison with the fraction eutectic predicted by the Bower-Brody-

Flemings equation shows that solid state diffusion, on the other hand, exerts a strong influence on microsegregation in the unreinforced material.

Table 6.1

Experimentally measured and calculated cell heights for unreinforced Aluminum 4.5 wt% Copper

Sample	T_{tip} (°C) BBF - calculated	G (K/m)	ΔX (μm) calculated	ΔX (μm) measured
201	570.7	14000	0	0
202	579.8	14000	800	0
203	601.8	13300	3000	2500*
204	570.7	17600	0	300*
205	604.0	16500	3400	1700*
207	611.7	17400	3660	3500
209	612.8	21300	3040	4000
210	621.4	19000	3860	4500
211	614.2	17000	3900	3900
212	611.6	9800	6400	5300
214	624.2	6500	11700	13200
215	623.8	8000	9500	11000
216	630.8	6800	12200	14400
217	618.2	13000	5400	6500
218	629.5	6200	13000	12500
219	624.7	8600	9000	11200

* theta phase disappears, eutectic front not reached.

Table 6.2

Comparison of Observed and Predicted Volume Fraction Eutectic in Unreinforced Al - 4.5wt% Cu

Sample	$g_{eutectic}$ experimental	$g_{eutectic}$ model	$g_{eutectic}$ model no conv	$g_{eutectic}$ BBF
201	0	0	0	0
202	0	0	0	0.033
203	0	0	0	0.068
204	0	0	0	0.003
205	0	0.007	0.010	0.070
207	0.029	0.027	0.033	0.076
209	0.019	0.020	0.025	0.076
210	0.060	0.024	0.030	0.081
211	0.038	0.037	0.045	0.077
212	0.038	0.036	0.043	0.076
214	0.021	0.018	0.021	0.083
215	0.020	0.019	0.023	0.083
216	0.011	0.011	0.049	0.086
217	0.014	0.015	0.020	0.080
218	0.005	0.004	0.005	0.082
219	0.004	0.003	0.004	0.083

6.2 Composite Solidification

6.2.1 Microsegregation

The finite-difference model predicts a nearly homogeneous matrix (the lowest minimum matrix copper predicted was $0.93C_o$) which is free of eutectic. Because the calculated effect of intercellular convection is small and because cell tip undercooling will reduce microsegregation in the matrix, this

result is in agreement with previous calculations of microsegregation in Al-4.5 wt pct Cu [74], which predicted that if $\Delta T^{-1} \cdot G \cdot V \cdot r^2 < 10^{-13}\ m^2 \cdot s^{-1}$, which was the case in all present experiments, a matrix free of microsegregation is obtained.

Theory is in agreement with experimental data in that (i) no eutectic was observed in any of the fully solidified composites, (ii) segregation profiles measured using the electron microprobe across interstices in Samples 209 and 218 showed a uniform matrix composition, and (iii) no coring patterns could be revealed after etching samples with the $KMnO_4$ - NaOH solution. It can be reasonably concluded that within the composite, equilibrium solidification is approached.

6.2.2 Interface Curvature Near the Reinforcement

Figure 5.16 shows the location of the primary solid phase of the matrix, removed from the fibers, and the location of the liquid phase near the fibers, which agrees with studies of dendritic solidification of Al-4.5 wt pct Cu matrix composites [74, 82, 83, 90]. The observation that the contact angle, θ of the solid metal on the fiber in the presence of the liquid metal (defined in Fig. 5.9) is greater than 90° implies that the fiber/liquid metal interfacial energy, σ_{FL}, is smaller than the fiber/solid metal interfacial energy, σ_{FS}. This is also in agreement with observations that toward the end of solidification, liquid metal concentrates in the form of pendular rings at contacting fibers, and that alumina does not catalyze heterogeneous nucleation in Al-Cu alloys [81-83, 90, 91].

As discussed in the literature review, a material with closely spaced reinforcements cannot exhibit a truly planar interface morphology unless the liquid-solid-reinforcement contact angle is 90°. Quenched solidification front

profiles suggest that the alloys of this study have contact angles greater than 90°. At high G/V, solidification conditions which result in a planar interface in unreinforced metal, the liquid-solid interface within a narrow interstice exhibits a degree of curvature, and thus an interface deflection, ΔX.

6.2.3 Limits on Predicted Cell Heights

To avoid subjectivity in characterizing liquid-solid interface morphology within the fiber reinforced composite, where due to the finite contact angle, all inerfaces exhibited a degree of curvature, a quantitative measure of cell height, namely $\Delta X_{0.95}$ defined previously, was used. $\Delta X_{0.95}$ also has the advantage of being simply related to solidification conditions according both to the Bower Brody and Flemings [54] (BBF) solute distribution equation for no solid state diffusion, and the corresponding equation for equilibrium cellular solidification, equation 3.16.

Consider again the Bower Brody and Flemings solute distribution equation (2.13 in this thesis), which can be rearranged to give the local temperature T for a given fraction solid, f_s:

$$T = m_L C_0 \left[\frac{a}{k-1} + \left(1 - \frac{ak}{k-1}\right) (1 - f_s)^{(k-1)} \right] \quad . \qquad (6.1)$$

Subtracting this temperature from the BBF tip temperature, given in equation (2.13), and rearranging, gives a difference in temperature, ΔT_{fs}, between the cell tips and the local temperature associated with a fixed fraction solid, f_s:

$$\Delta T_{fs} = m_L C_0 \left(1 - (1 - f_s)^{(k-1)}\right) \left[1 - \frac{ak}{k-1}\right] \quad . \qquad (6.2)$$

where a is the BBF parameter, defined in equation (2.14).

Similarly, for equilibrium cellular solidification, (equation 3.16), ΔT_{fs} is:

$$\Delta T_{fs} = \frac{m_L C_0 f_s (k-1)}{1 - f_s (1-k)} \left[1 - \frac{ak}{k-1}\right] \quad . \tag{6.3}$$

A cell height, or distance from the cell tips at which a given fraction solid f_s is reached, ΔX_{fs}, is given by:

$$\Delta X_{fs} = \frac{\Delta T_{fs}}{G} \quad . \tag{6.4}$$

As a measure of deviation of solidification conditions from plane front breakdown, we define ΔV, the velocity offset from constitutional supercooling (shown schematically in Figure 6.3):

$$\Delta V = V - \left(\frac{V}{G}\right)_{cs} \cdot G \, , \tag{6.5}$$

where V and G are experimental values of velocity and temperature gradient and $(V/G)_{cs}$ is the critical ratio for plane front stability according to the constitutional supercooling criterion, equation 2.3. Substituting for $(V/G)_{cs}$ yields:

$$\Delta V = V - \frac{D_L k}{m_L C_0 (k-1)} G \quad , \tag{6.6}$$

or, after rearrangement:

$$\Delta V = V \left[1 - \frac{ak}{k-1}\right] \quad . \tag{6.7}$$

ΔX_{fs} can then be directly related to ΔV. For no solid state diffusion:

$$\Delta X_{fs,BBF}\ G\ V = m_L\ C_0 \left(1 - (1 - f_s)^{(k-1)}\right) \Delta V \quad . \tag{6.8}$$

While for equilibrium solidification:

$$\Delta X_{fs,equilibrium}\ G\ V = \frac{m_L C_0\ f_s\ (k-1)}{1 - f_s\ (1-k)} \Delta V \quad . \tag{6.9}$$

Since densities of the solid and liquid phases are assumed equal and independent of composition in the above equations, weight fraction solid, f_s, is equivalent to volume fraction solid, g_s, and hence $\Delta X_{fs} = \Delta X_{gs}$.

6.2.4 Comparison of Cell Height in Unreinforced and Composite Sections

In Figure 6.4, $\Delta X_{0.95} \cdot G \cdot V$ is plotted versus the deviation from plane front stability, ΔV, for the unreinforced and composite sections of Al - 4.5% Cu. Similar plots for Al - 1.0% Cu are shown in Figure 6.5.

This analysis is in good agreement with data for the unreinforced material: unreinforced cell heights are zero (corresponding to a planar front) when $\Delta V < 0$, and experimental values of $\Delta X_{0.95} \cdot GV$ in unreinforced samples fall between the limits of the BBF equation (no diffusion) and equilibrium solidification, when $\Delta V > 0$. The greater scatter in data for unreinforced Al - 1.0% Cu compared to Al - 4.5% Cu could be a result of two factors: the automated image processing used in data acquisition for Al-4.5 wt pct Cu had a better resolution, and that in Al - 1.0% Cu, $g_3 = 0.95$ is closer to

the cell tips, where some assumptions in the BBF approach may become invalid.

Cell height data for the composite, on the other hand, are in disagreement with this analysis in three respects. First, starting from $\Delta V < 0$, the composite exhibits low, but nonzero cell heights, consistent with the obtuse liquid-solid-fiber contact angle, θ. This plateau of low values for $\Delta X_{0.95} \cdot G \cdot V$ continues as ΔV increases past zero, however, before increasing in an approximately linear fashion, a point we define a psuedo-planar to cellular transition. This transition is offset from the constitutional supercooling criterion, $\Delta V = 0$. Evidence of this effect can be seen in Figures 5.1 and 5.2, where the composite's liquid-solid interface morphology remains fairly flat as the unreinforced solidification front undergoes a clear transition from a planar to cellular morphology.

The location of the psuedo-planar to cellular transition during geometrically constrained solidification is roughly predicted by linear stability analysis, as shown in equation 3.9:

$$\Delta V = \Delta V_{geom} = - \frac{2\pi^2 T_M \Gamma D_L k}{\lambda^2 m_L C_0 (1-k)} , \qquad (6.10)$$

where λ is the constrained maximum wavelength (interstice diameter, measured to be 25μm) and $m_L < 0$, giving a positive deviation from constitutional supercooling.

For Al - 4.5 % Cu the pseudo-planar to cellular transition is predicted to occur at $\Delta V = 0.6$ μm/s, while for Al - 1.0 % Cu the transition is predicted to be at $\Delta V = 2.8$ μm/s. These values, indicated on Figures 6.4 and 6.5, are in overall agreement with experimental data, indicating that the offset in the

breakdown of pseudo-plane front solidification is a result of capillarity, which stabilizes a plane front against small wavelength perturbations in accordance with Mullins and Sekerka's linear stability analysis. In summary, capillary effects are responsible for a loss of planarity in the solidification front at low ΔV, and for an increase in the critical ΔV for development of a cellular solidification front which entails large deviations from planarity.

This result is in disagreement with the generalized interface morphology map given by Trivedi, et al [78], Figure 2.3, since a planar interface is stabilized, not destabilized, by the fiber interstices. When the liquid-solid-reinforcement contact angle θ, is near 90°, the destabilizing effects of curvature are weak and plane front stability arising from geometric wavelength exclusion is expected to predominate. If contact angles are significantly larger than 90°, the calculations of Ungar and Brown [47] show that a planar front will tend to be destabilized in the presence of geometric constraints.

The third discrepancy in the $\Delta X_{0.95}$ G V vs ΔV plots for composite solidification is the prediction of interface deflection, or cell heights when a cellular interface morphology exists. Because they exhibit essentially no microsegregation, composites with cellular interface morphologies should approach equilibrium cellular solidification, described by equations 6.9 and 3.16. It is seen in Figures 6.4 and 6.5 that experimental values, including a "worst-case" estimate of the error in measurement of $\Delta X_{0.95}$, fall below the equilibrium solidification limit for BBF tip temperatures. Since in the absence of composition gradients in the solid the cell root must be at the alloy solidus temperature, a smaller cell height indicates that the cell tip undercooling is greater than predicted by the BBF model.

This is reinforced by reconsidering the plots of measured fraction solid versus distance from cell tips for the composite. We can assume the composites solidify in an equilibrium manner, which implies the volume fraction solid will be the maximum possible at a given temperature or distance from the cell tips. The actual liquid-solid interface prior to the quench may not coincide with the apparent liquid-solid interface on a metallographic section however, if the cell grew during the quench. Microstructural features counted as liquid were verified, with scanning electron microscopy, to have a fine lamellar structure and thus should correspond to material with the eutectic phase, or possibly eutectic with additional included primary phase. If we assume that all the primary phase is divorced from the eutectic during the quench and instead nucleates and grows on the existing primary solid, the apparent volume fraction solid (on a metallographic section) will be larger than the actual volume fraction solid prior to the quench. Figures 6.6 and 6.7 compare measured volume fraction solid (actually a measurement of volume fraction of primary alpha phase) to the volume fractions solid predicted by equilibrium cellular solidification (equation 3.16) and equilibrium cellular solidification with additional primary phase deposited on the cell during the quench. Solidification during the quench assumed to follow the Scheil equation (equation 2.15). Assuming there is no difficulty in nucleating the eutectic phase, this last line represents and upper bound on the volume fraction of primary phase if the cell tips are at the Bower-Brody-Flemings temperature.

In figure 6.6, the experimental points lie slightly above the predicted upper bound. This sample, 209, had a relativley small unreinforced cell spacing, so geometric constraint was not as severe. Measured and predicted volume fraction solid for another sample, which had a much larger unreinforced cell

spacing, and thus greater degree of geometric constraint in the composite, are shown in figure 6.7. The experimental points lie far above the predicted upper bound. These higher than predicted volume fraction solid are consistent with a lower cell tips temperature. The cell tip undercooling appears to be larger when the degree of geometric constraint is larger, which is again consistent with previous calculations. Unfortunately, the lack of a reference temperature, such as a eutectic front or a thermocouple embedded in the composite, prevented composite cell tip temperatures from being directly measured.

A large increase in cell tip undercooling within the composite is unlikely to result from the Gibbs-Thomson effect since cell tip radii of curvature are much larger than 1μm (a tip radius of 1 μm would induce a tip undercooling of only 0.25 K) [92]. Fibers may alter temperature distributions in the matrix near the solidification front, serving as a sink for the latent heat released by the solidifying metal. Calculations of Ungar, Bennett and Brown [48] suggest that this effect is negligible, however, if we assimilate the effect of the fibers to an increase in the apparent heat capacity of the solidifying metal. An increase in cell tip undercooling in the composite would therefore be best explained as a combined result of diffusive and capillary effects, in qualitative agreement with calculations of McCartney and Hunt [50 , 51, 53] and calculations and observations of Trivedi, Han and Sekhar [78], who predict that cell tip undercoolings will increase when cell diameters decrease significantly below their unconstrained values.

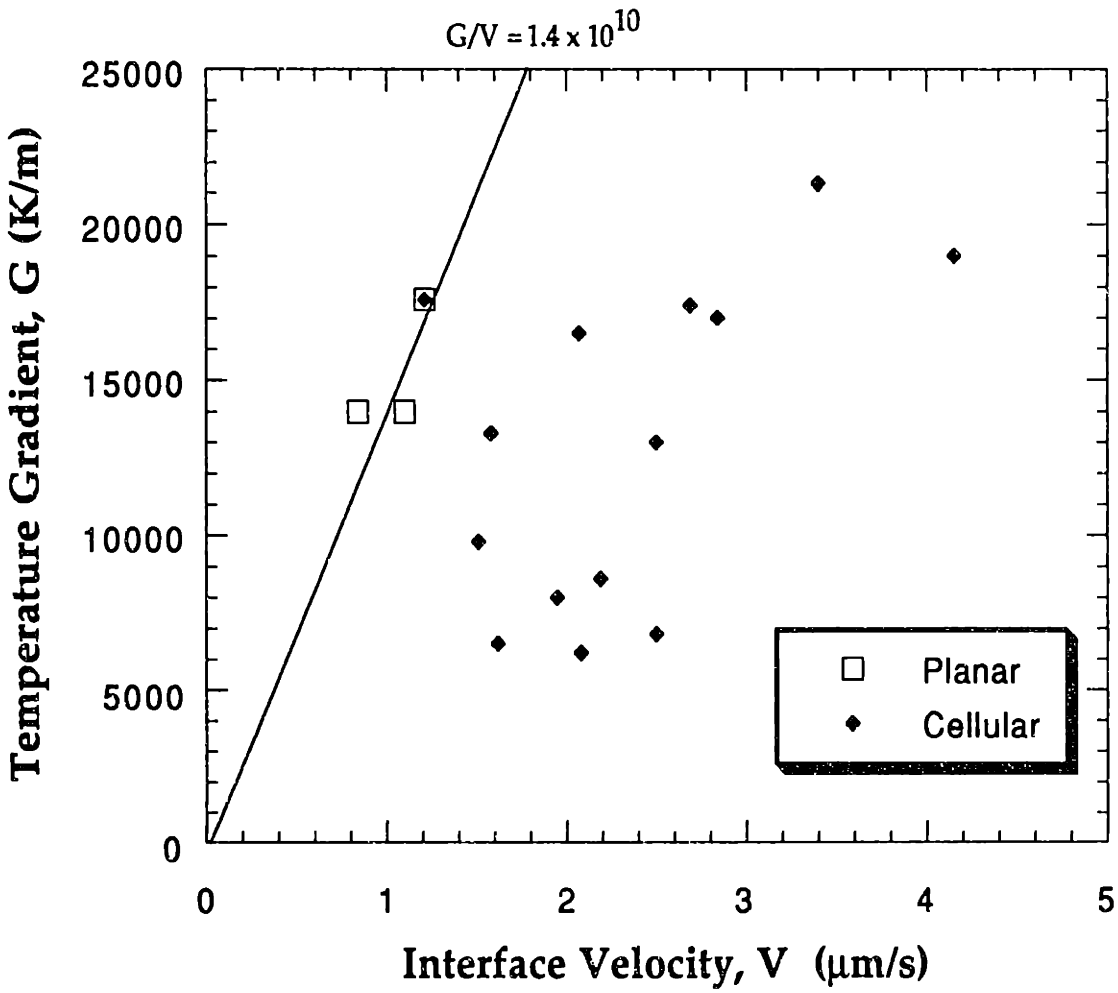

Figure 6.1 Interface morphology as a function of temperature gradient, G, and interface velocity, V in Al - 4.5 wt% Cu. A best fit line through the data yields a critical G/V ratio of 1.4×10^{10} Ks/m^2 for plane front stability.

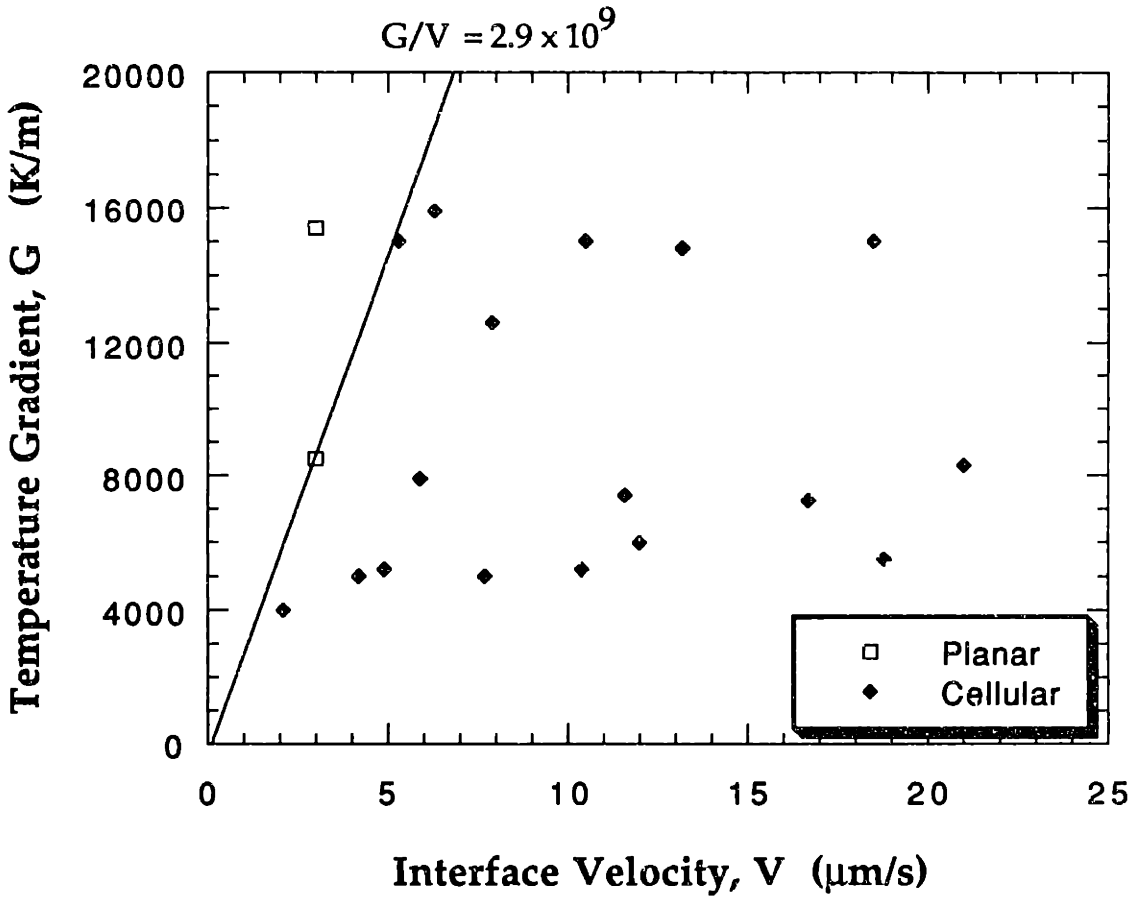

Figure 6.2 Interface morphology as a function of temperature gradient, G, and interface velocity, V in Al - 1.0wt% Cu. A best fit line through the data yields a critical G/V ratio of 2.9 x 10^9 Ks/m^2 for plane front stability.

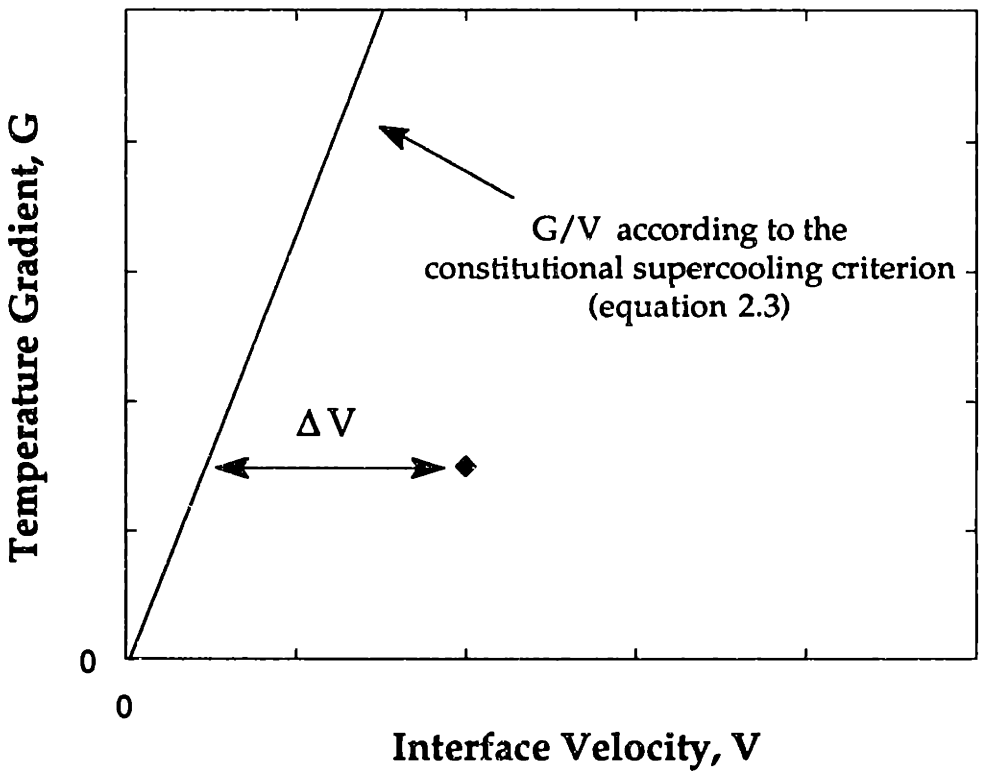

Figure 6.3 Definition of ΔV, the deviation in interface velocity from plane front stability solidification conditions. $\Delta V < 0$ indicates a plane front is stable.

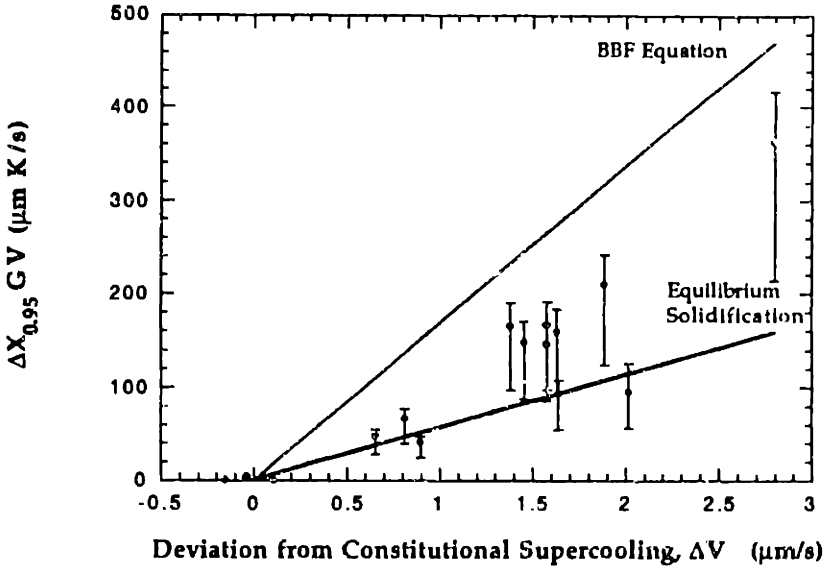

(a)

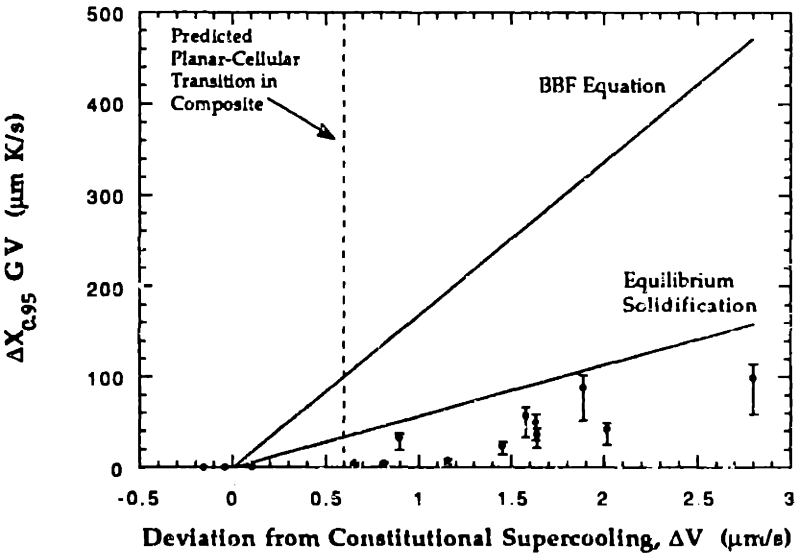

(b)

Figure 6.4 Plot of cell height parameter, $\Delta X_{0.95} \cdot G \cdot V$, as a function of the deviation from plane front instability, ΔV, for Al - 4.5wt% Cu. Limits which correspond to the Bower, Brody and Flemings cellular solidification model (no diffusion in solid during solidification) and equilibrium cellular solidification (complete diffusion in solid) are also given. a) unreinforced metal. b) composite. The location of the predicted pseudo-planar to cellular transition in the composite, is also shown.

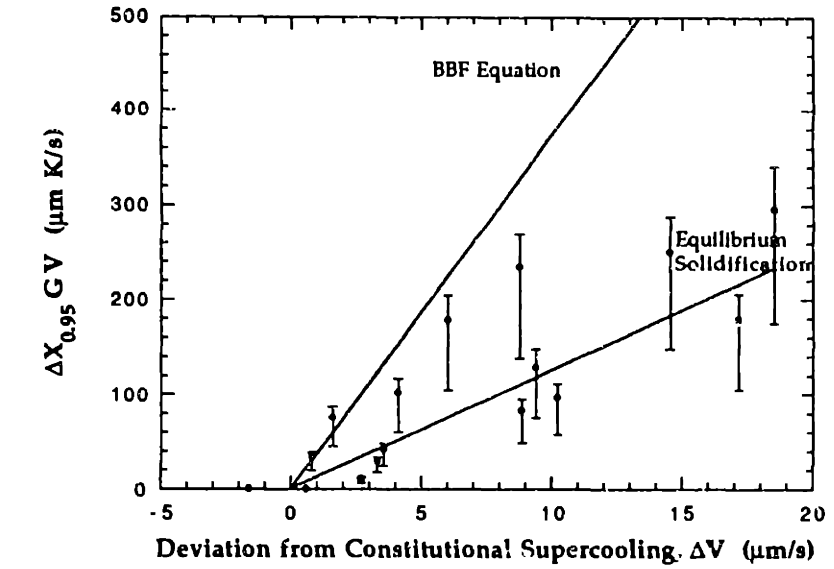

(a)

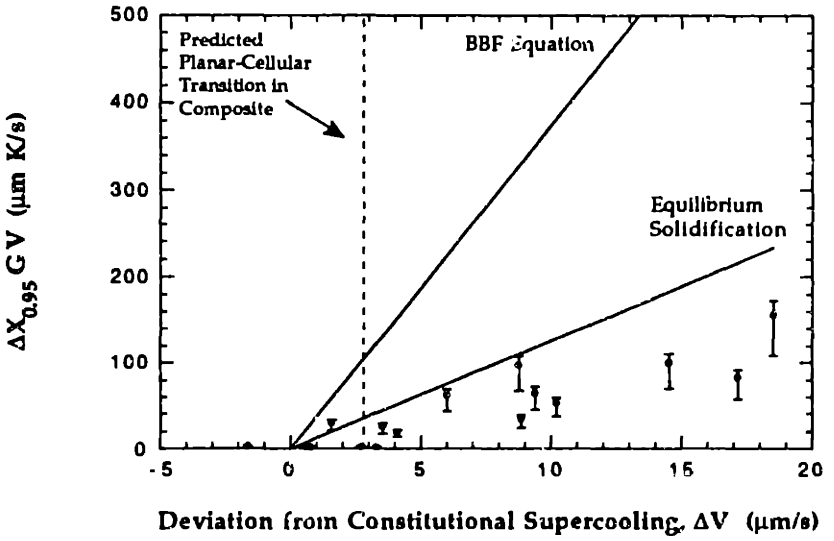

(b)

Figure 6.5 Plot of cell height parameter, $\Delta X_{0.95} \cdot G \cdot V$, as a function of the deviation from plane front instability, ΔV, for Al - 1.0wt% Cu. Limits which correspond to the Bower, Brody and Flemings cellular solidification model (no diffusion in solid) and equilibrium cellular solidification (complete diffusion) are also given. a) unreinforced metal. b) composite. The location of the predicted pseudo-planar to cellular transition is also shown.

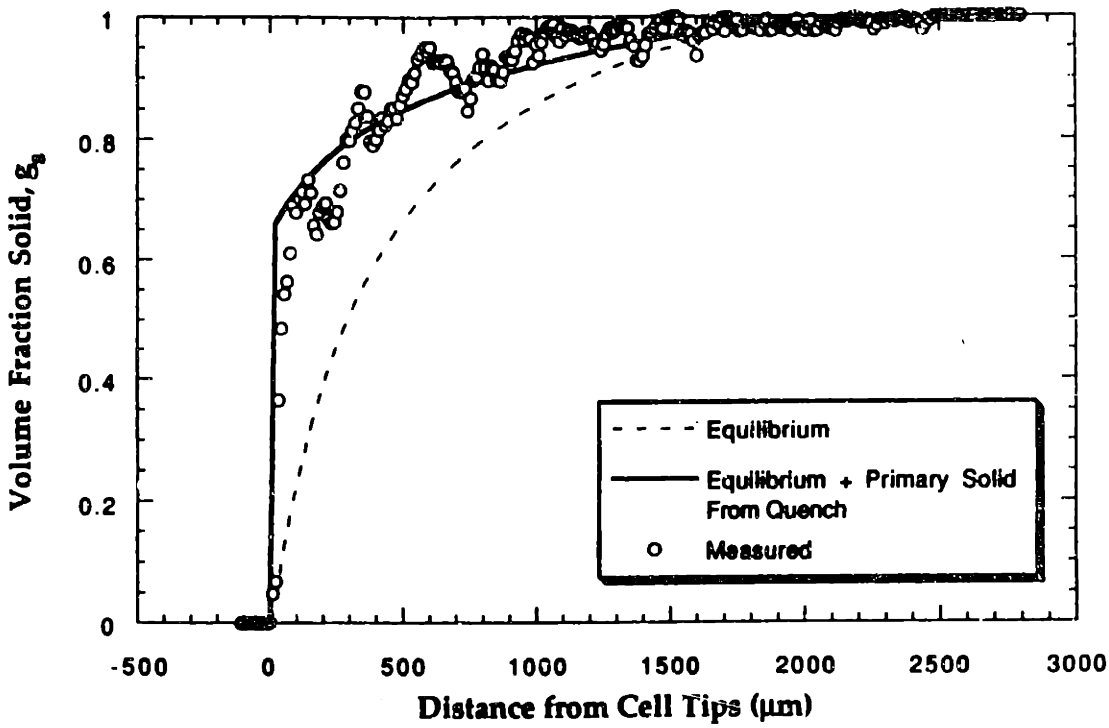

Figure 6.6 Measured and predicted volume fraction solid for equilibrium solidification and equilibrium solidification with growth of the solidifying metal during the quench. Experimental points lie above the predicted maximum volume fraction of primary solid, indicating the cell tips were undercooled below the Bower-Brody-Flemings temperature. Sample 209.

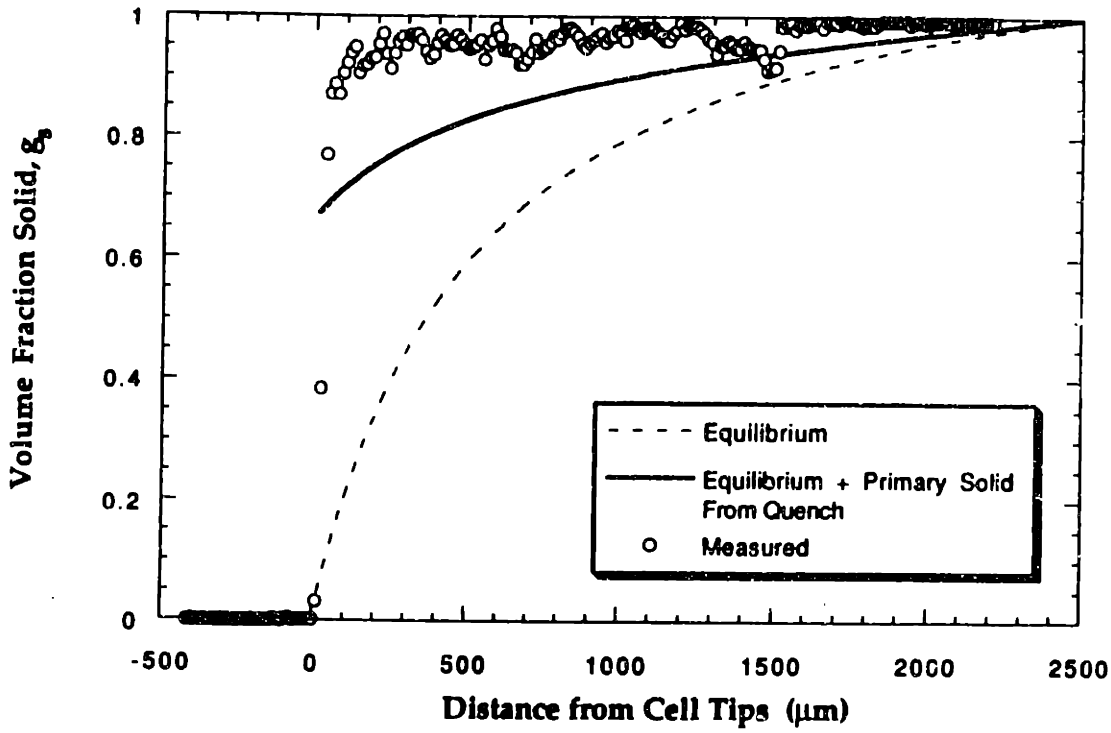

Figure 6.7 Measured and predicted volume fraction solid for equilibrium solidification and equilibrium solidification with growth of the solidifying metal during the quench. Experimental points lie above the predicted maximum volume fraction of primary solid, indicating the cell tips were undercooled below the Bower-Brody-Flemings temperature. Note the discrepancy between experimental and predicted volume gfraction primary solid is greater than the previous figure, indicating the effect of the geometric constraint was larger. Sample 211.

Chapter 7
Conclusions

- Measured solidification parameters for the transition from plane front to cellular solidification of unreinforced Al-1 wt pct and Al-4.5 wt pct Cu agree with the constitutional supercooling criterion using a diffusion coefficient in the liquid $D_L = 5 \cdot 10^{-9}\ m^2 \cdot s^{-1}$. Cell heights are consistent with cell tip undercoolings predicted by the Bower, Brody and Flemings cellular solidification model.

- Microsegregation resulting from solidification of cylindrically symmetric cells is predicted using a finite difference model assuming a cell tip undercooling given by the Bower-Brody-Flemings equation. Model predictions agree with experimental measurements of fraction eutectic in the unreinforced metal.

- In the presence of parallel alumina fibers, fully solidified Al-1 wt pct and Al-4.5 wt pct Cu are essentially free of microsegregation, in agreement with theory which predicts that the fibers limit the scale of microstructural features in the matrix, allowing solid state diffusion to erase microsegregation during solidification.

- The shape of the liquid/solid metal interface near the fibers indicates a lower fiber/liquid metal interfacial energy compared to the fiber/solid metal interfacial energy.

- Liquid-solid metal interfaces in the composite feature a pseudo-planar morphology for high ratios of temperature gradient to growth velocity. A transition to cellular solidification, at which interface deflection increases rapidly, is observed beyond the onset of plane front instability in the unreinforced metal. The location of this transition agrees with a direct application of linear morphological stability theory, indicating that the greater stability of plane fronts in the composite results from the influence of finite liquid/solid metal interfacial energy.

- Composite cell heights are significantly smaller than is predicted when cell tip undercooling is as given by the Bower, Brody and Flemings equation, indicating that geometrical constraint by the fibers increases cell tip undercooling.

Chapter 8
Suggestions for Future Work

1). A smaller fiber diameter, or higher volume fraction fiber would lead to narrower interstices and may produce a much greater stabilization of the pseudo-planar liquid-solid interface in a metal matrix composite. Although solute redistribution within the composites in this study was nearly complete, a narrower interstice should produce the same effect over a larger range of cooling rates.

2). A reference temperature in the composite would allow a direct measurement of cell tip temperature to be made. The most straight-forward way to accomplish this would be to incorporate a thermocouple within the composite. "Three-dimensional" metallography techniques could also be used to estimate the effect of interstice size on cell tip temperature, since the inhomogeneous fiber distribution produces a range of interstice sizes, and hence geometrically constrained cell sizes. Material removal during polishing would have to be done in small increments to ensure catching the cell tip position and true interstice size.

3). The effect of a reinforcement on a more complicated solidification system, such as a eutectic or monotectic system where cooperative growth of two phases occurs, would be interesting. The reinforcement could be expected to alter the equilibrium spacing of the material, or perhaps produce a nonsteady-state structure.

4). The contact angle at the liquid- solid-reinforcement triple line could be varied to examine meniscus effects on the planar interface stability. The most straightforward method of investigating this effect would be to change the chemical nature of the reinforcement while maintaining matrix composition(s). Each fiber/matrix combination should be chemically inert, however, due to the long times at high temperature characteristic of steady state plane front solidification.

5). The solidification behavior with other reinforcement geometries should be investigated. Solidification perpendicular to a fiber axis, solidification within nonaligned fiber interstices, within a tightly packed particulate preform, or within a foam would be inherently nonsteady-state and therefore more complex, but of greater practical interest. Similarly, nonsteady-state solidification conditions could be explored because they are of greater practical interest to the production of engineering materials.

Appendix A Definition of Variables

Variable	Definition	Units
A	Dimensionless Stability parameter, given by Eq 2.9	
a	Cellular solidification parameter, given by Eq. 2.14	
C_0	Nominal composition	wt%
C_E	Eutectic composition	wt%
C_{SE}	Eutectic solid composition	wt%
C_L	Liquid composition	wt%
C_L^*	Liquid composition at the interface	wt%
C_p	Specific Heat	cal/°C
C_s	Solid composition	wt%
C_s^*	Solid composition at interface	wt%
C_t	Liquid composition at cell tips	wt%
d	Channel spacing, or fiber interstice width	m
D_L	Diffusivity in liquid	m^2/s
D_S	Diffusivity in solid	m^2/s
f_E	Weight fraction eutectic	
f_l	Weight fraction liquid	
f_s	Weight fraction solid	
g_E	Volume fraction eutectic	
g_s	Volume fraction solid	

G_L	Thermal gradient in liquid	K/m
G_c	Solute gradient in liquid	wt%/m
G_s	Thermal gradient in solid	K/m
$\mathcal{G}_l, \mathcal{G}_s$	Conductivity weighted thermal gradients	K/m
G*	Conductivity weighted average thermal gradient	K/m
H	Finite difference parameter = $\delta t/(\delta \rho)^2$	
i	Radial position counter in computer model	
i*	Node before interface in computer model	
j	Time counter in computer model	
K_L	Thermal Conductivity of liquid	W/mK
K_s	Thermal conductivity of solid	W/mK
k	Equilibrium partition ratio = C_s^*/C_L^*	
k_t	Partition ratio for cell tips	
L	Latent Heat of Fusion	J/g
m_L	Liquidus slope on phase diagram	K/wt%
m_s	Solidus slope on phase diagram	K/wt%
p	1 - k (equilibrium partition ratio)	
r	cell radial position	m
r*	Location of liquid solid interface in cell	m
r_T	cell radius	m
S	Sekerka's stability function	
S_t	Stefan number	
T	Temperature	K
T_E	Eutectic temperature	K

T_L	Liquidus temperature	K
T_M	Melting temperature of pure solvent	K
T_S	Solidus temperature	K
T_t	Cell tip temperature	K
ΔT_{fs}	Temperature difference between cell tips and given fs	K
$\Delta T_{0.95}$	Temperature difference between cell tips and fs = 0.95	K
t	time	s
V	Interface movement rate	m/sec
V_c	Critical velocity for onset of plane front instability	m/sec
V_f	Volume fraction fiber	
ΔV	Deviation from plane front stability, defined in Fig 6.3	m/sec
ΔX	Distance from cell tips to fs = 1	m
ΔX_{fs}	Distance from cell tips to a given fs	m
$\Delta X_{0.95}$	Distance from cell tips to fs = 0.95	m
z	distance from interface	m
Γ	Gibbs-Thomson coefficient	K m
δ	perturbation height	m
$\dot{\delta}$	perturbation growth rate	m/s
θ	contact angle	°
κ	interface curvature	m^{-1}
λ	perturbation or cell wavelength	m
ϑ_L	intercellular liquid velocity	m/s
ρ_L	Liquid density	g/cm^3
ρ_S	Solid density	g/cm^3

ϕ	radial position in finite difference model	
$\Delta\phi$	radial increment in finite difference model	
ψ	fraction of radial increment last portion of solid in model	
ω	perturbation wavenumber = $2\pi/\lambda$	m^{-1}
ω_c	critical wavenumber at the onset of instability	m^{-1}
ω^*	adjusted perturbation wavenumber	m^{-1}

Appendix B

Thermophysical Properties for Al- Cu alloys

B.1 Phase Diagram

The aluminum rich corner of the aluminum-copper phase diagram is given in Figure B.1. The melting point of pure aluminum is 660.45 °C. A eutectic reaction occurs at 548 °C, where the composition of the liquid and primary aluminum are 33.0 wt% copper and 5.65 wt % copper, respectively. Average values of the liquidus slope and partition ratios were obtained by approximating the phase diagram liquidus and solidus as straight lines. Thus,

$$m_L = \frac{548°C - 660°C}{33.0 \text{ wt \%}} = -3.393 \text{ K/wt\%} , \qquad (B.1)$$

and

$$k = \frac{5.65 \text{ wt\%}}{33.0 \text{ wt\%}} = 0.172 . \qquad (B.2)$$

B.2 Diffusion Coefficients

For diffusion of copper in solid, primary aluminum, the chemical diffusion coefficient determined by Murphy [93] is used:

$$D_S = 0.29\, e^{-15662/T} \times 10^{-4} \text{ m}^2/\text{s} . \qquad (B.3)$$

It is assumed that diffusivity is independent of solute concentration. Murphy showed this to be the case for dilute alloys, from 0 to 0.5 wt% copper. Other researchers [94 , 95] have reported similar values.

In the liquid phase, the diffusivity of copper in aluminum is assumed to be independent of temperature as well as composition within ranges of interest. As this temperature range is not very large, this assumption should be valid. Several values of diffusion coefficients are reported in the literature. Watson and Hunt [96], using a temperature gradient zone melting technique, consistently obtained a value of 3.51×10^{-9} m^2/s. Sato and Ohira [31] and Ejima, et al., [97] both report values of 5.0×10^{-9} m^2/s.

B.3 Densities

Values for the density of various aluminum copper alloys at the liquidus and solidus temperatures have been reported by Sergeev [98] and compiled from the work of many researchers [99]. A quadratic equation was used to model the variation in reported liquid and solid densities with their respective compositions. Figure B.2 shows the reported data and the best fit curve, which had an R-squared value of 0.999. In the computer model, the value chosen for the primary solid density was that of the average solid composition,

$$\rho_{s,\,primary} = 2.66\ g/cm^3\ . \qquad (B.4)$$

For the the liquid, and the eutectic solid, the following equations were used for the density at the solidus, or liquidus temperatures:

$$\rho_L = 2.395 + 1.698\times10^{-2}\ C_L + 2.689\times10^{-4}\ C_L^2\ , \qquad (B.5)$$

$$\rho_{s,\,eutectic} = 2.577 + 1.74\times10^{-2}\ C_{SE} + 2.241\times10^{-4}\ C_{SE}^2\ . \qquad (B.6)$$

B.4 Gibbs-Thomson constant

Recently, Gündüz and Hunt [85] experimentally determined the Gibbs-Thomson constant for primary aluminum in contact with an aluminum-copper melt by measuring the shape of grain boundary cusps at the liquid-solid interface. Their value is:

$$\Gamma = \frac{\sigma_{SL}}{\Delta S_f} = 2.41 \times 10\text{-}7 \quad \mathrm{K\,m}\ . \qquad (B.7)$$

B.5 Thermal Conductivities and Heat of Fusion

The heat of fusion for pure aluminum, 388.1 J/g [100], is used. Gündüz and Hunt, in determining the Gibbs-Thomson constant [85] , measured the thermal conductivity of solid aluminum- 5.7 wt% copper directly and the ratio of solid and liquid thermal conductivities by a unidirectional growth technique. They obtained values of:

$$K_S = 135.9 \quad \mathrm{W/mK}\ , \qquad (B.8)$$

$$R = \frac{K_L}{K_S} = 0.428\ , \qquad (B.9)$$

which imply that

$$K_L = 58.2\ \mathrm{W/mK}\ . \qquad (B.10)$$

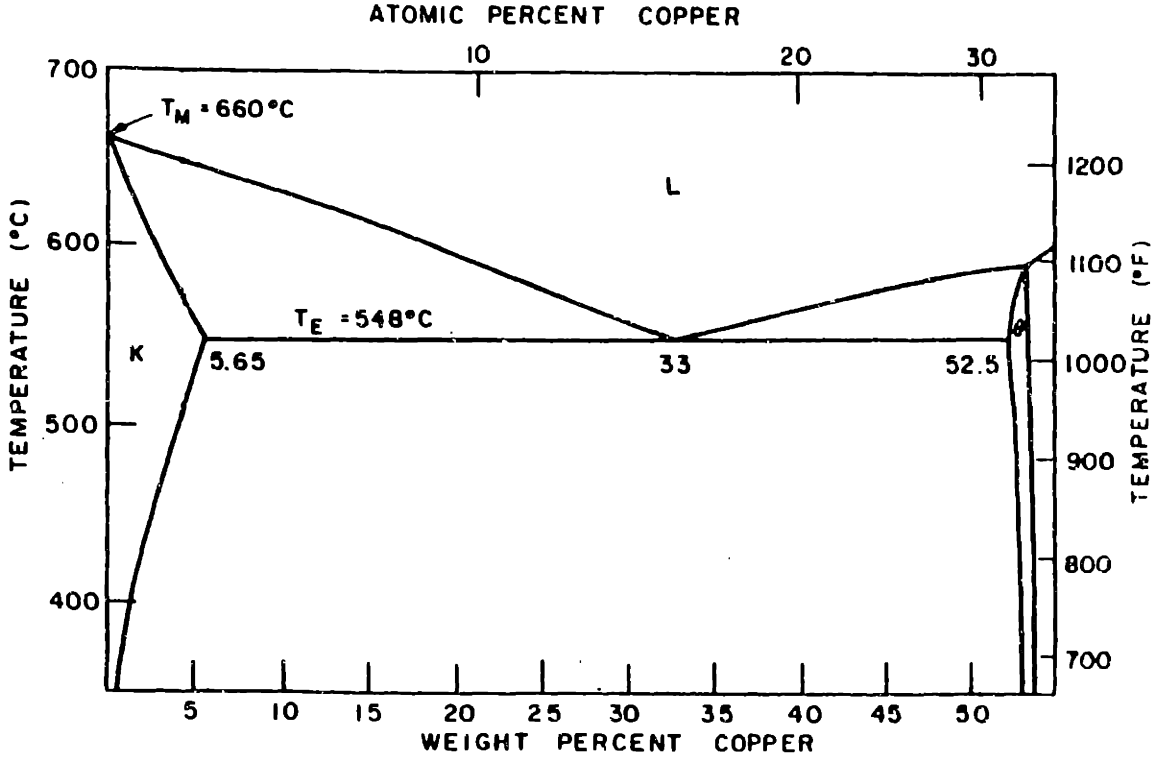

Figure B.1 Aluminum rich end of the Aluminum - Copper phase diagram. [101]

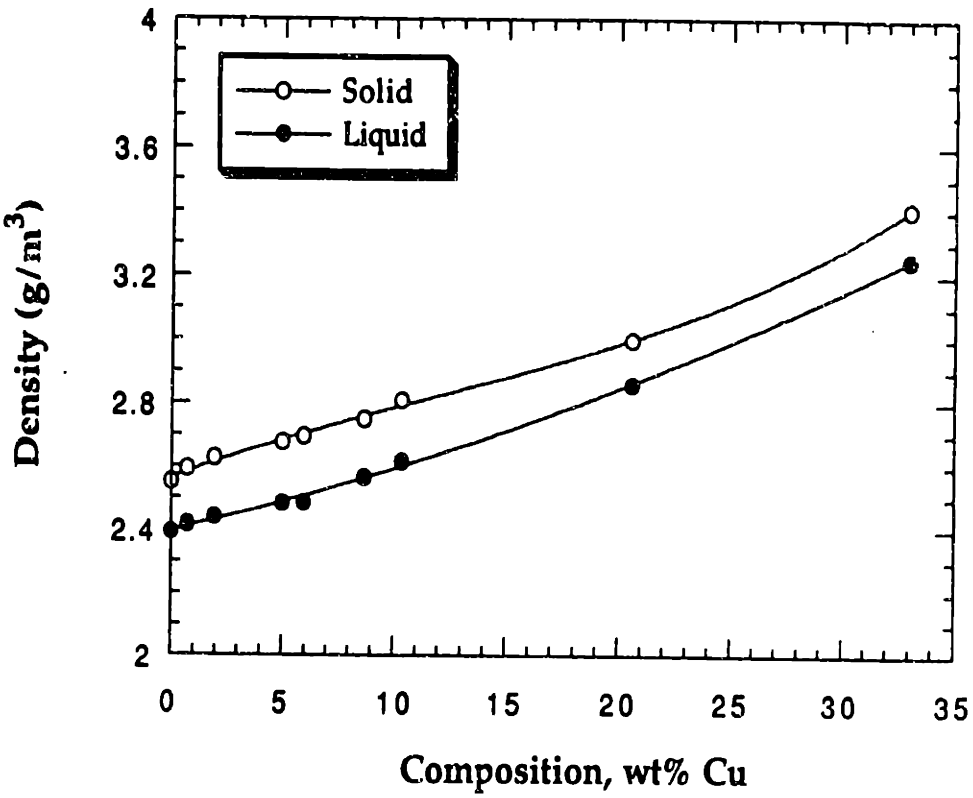

Figure B.2 Density of aluminum-copper alloys at their solidus and liquidus. Data points are from Sergeev [98] and Mondolfo [99].

Appendix C Computer Solidification Model

C.1 General Approach

The cellular solidification free boundary problem outlined in chapter 3 (equations 3.21 to 3.36) was solved using a finite difference method. Solid metal was assumed to be growing with circular cross-section within a cylinder of radius r_T. Because of this symmetry, a radial slice was considered, within which distances are normalized by r_T. The cylinder radius was divided into an adjustable number of increments, N. Mesh size, or radial increment, $\Delta\phi$, defined by:

$$\Delta\phi = \frac{\phi}{N} \quad , \tag{C.1}$$

was therefore easily varied to refine the accuracy of the solution.

Composition, normalized with respect to average composition C_0, was calculated at each node, or mesh point. The position of the liquid-solid interface within this radial slice was traced as a function of local solidification time. Following the approach of Mortensen [88], the liquid-solid interface is allowed to float between node points so that its position, ϕ^*, is:

$$\phi^* = i^*\Delta\phi + \delta\phi^* \quad , \tag{C.2}$$

where i^* is the last solid node and $\delta\phi^*$ is the distance between i^* and the interface. Temperature decreases, according to an assumed constant cooling rate, as solidification time increases. Tracing the liquid-solid interface position after successive time steps gives a discretized cell shape or fraction

solid versus temperature relation. A schematic illustration of this, providing a definition of above variables, is given in Figure C.1.

During each time increment, solid state diffusion and growth of the solid both take place. These processes are decoupled in the program so that solid state diffusion occurs, then the new liquid-solid interface position is determined and finally variables are updated in preparation for the next step. A flow chart for the program is given in Figure C.2.

C.2 Initialization of Program

At the cell tips, temperature and liquid composition are initialized to appropriate values and a bulk liquid flow velocity is estimated. A small amount of material, corresponding to two radial increments (0.0004 fraction solid when a 100 increment mesh is used), is solidified according to the Bower, Brody Flemings equation (2.13). Ignoring solid state diffusion during solidification in this initialization step does not have a significant effect on final compositions. Since the liquid is assumed to be completely mixed, all liquid node points have an average liquid composition.

C.3 Solid State Diffusion

The finite difference form of Fick's second law for solid state diffusion, after simplification of equation 3.20, becomes:

$$i = 0 \qquad C_{0,j+1} = C_{0,j} + 4H\{C_{1,j} - C_{0,j}\}, \tag{C.3}$$

$$0 < i < i^* \qquad C_{i,j+1} = C_{i,j} + \frac{H}{2i}\{(2i+1)C_{i+1,j} - 4i\,C_{i,j} + (2i-1)C_{i-1,j}\}, \tag{C.4}$$

in explicit finite difference form [102], where $C_{i,j}$ represents composition at node i for time step j. H is a finite difference stability parameter defined as:

$$H = \frac{D_s \Delta t}{\Delta \phi^2} \quad , \tag{C.5}$$

and Δt is the time increment. At the node nearest the interface, i*, there is generally not a symmetric mesh spacing ($\Delta\phi \neq \delta\phi^*$), so a modified version of equation (C.3) must be used [103]:

$$i = i^* \quad C_{i^*,j+1} = C_{i^*,j} + \frac{H}{i^*}\left\{ k C_L \frac{2i^*+1}{\psi(\psi+1)} - C_{i^*,j}\frac{2i^*+1-\psi}{\psi} + C_{i^*-1,j}\frac{2i^*-\psi}{\psi+1} \right\} \tag{C.6}$$

where ψ is $\delta\phi^*/\Delta\phi$.

As solid diffusivity varies strongly with temperature, Δt also varies and must be calculated during each iteration. The time interval Δt and cooling rate are used to update local temperature T, from which new equilibrium liquid and interfacial solid compositions are determined from discretized forms of equations 3.18, 3.27 and 3.22:

$$T_{j+1} = T_j - G\,V\,\Delta t_j \quad , \tag{C.7}$$

$$C_{L,j+1} = \frac{T_{j+1} - T_M}{m_L} \quad , \tag{C.8}$$

$$C_s^* = k\,C_{L,j+1} \quad . \tag{C.9}$$

C.4 Solidification

Incremental growth of the solid occurs by an amount determined by a mass balance in the liquid portion of the volume element, given in differential form by equation 3.33. A schematic drawing of two successive radial slices through a cell, illustrating terminology used in the discretized form of this mass balance, is shown in Figure C.3.

First, consider a mass of solute in the liquid at $t = t_n$. For convenience, units are given as gram wt% solute. At $t = t_n$, there is a total mass of solute, M_n,

$$M_n \text{ (g wt\%)} = (\pi (R_T^2 - R_N^2) \, V \, \Delta t) \, \rho_{L,n} \, C_{L,n} \quad , \qquad \text{(C.10)}$$

where $\rho_{L,n}$ and $C_{L,n}$ are liquid density and composition at $t = t_n$, R_T is the radius of the volume element and R_n is the radius of the liquid at $t = t_n$. $\rho_{L,n}$ is allowed to vary with composition and temperature as given in Appendix B.

Solute incorporated by diffusion into the solid, Δm_{diff}, is determined by integrating the change in solid composition:

$$\Delta m_{diff} \text{ (g wt\%)} = \{ 2 \pi \int_0^{R_n} \rho_s \, R \, (C_{i,j+1} - C_{i,j}) \, dR \} \, V \, \Delta t \quad , \qquad \text{(C.11)}$$

where ρ_s is density of the primary solid, assumed to be independent of composition and temperature, and R is radial position. This integral is computed using the trapezoidal rule with end corrections [104]:

$$\int_a^b y \, dx = h \left[\tfrac{1}{2} y_0 + y_1 + y_2 + y_3 + \ldots + y_{n-1} + \tfrac{1}{2} y_n \right] + \frac{h^2}{12} \left[y_0' - y_n' \right] \quad , \qquad \text{(C.12)}$$

where:

$$y_1 = \text{function integrated} = 2\pi R (C_{i,j+1} - C_{i,j}) \rho_s \quad , \qquad (C.13)$$

and

$$h = \frac{b - a}{n} = \text{interval size} = \Delta\phi \, . \qquad (C.14)$$

The mathematical error in this integration is of order h^4. An additional term, representing the solute incorporated between i* and the interface, calculated with a linear interpolation, is added to the above integral:

$$\pi \, \Delta\phi \, \partial\phi^* \, i^* (C_{i,j+1} - C_{i,j}). \qquad (C.15)$$

The mass flux, W_z through the volume element due to longitudinal diffusion in the liquid is given by:

$$W_z = - D_L \, \rho_{L,n} \frac{dC_L}{dz} \quad . \qquad (C.16)$$

This results in a difference in mass flow rate at steps $t = t_n$ and t_{n+1}, Δm_{long}, given in finite difference form by:

$$\Delta m_{long} \, (g \, wt\%) = - \frac{D_L G_L}{m_L} \, [\rho_{L,n} \, \pi (R_T^2 - R_N^2) - \rho_{L,n+1} \, \pi (R_T^2 - R_{N+1}^2)] \, \Delta t \quad . \qquad (C.17)$$

As there is a difference in the density of the liquid and solid phases, as well as a variation in liquid density with composition and temperature, intercellular liquid flows to feed shrinkage (or expansion) along the cell. The

mass that accumulates in (or leaves) a volume element to compensate for volume changes is:

$$\Delta m_{conv}\ (g\ wt\%) = \pi\ \Delta t\ [(R_T^2 - R_n^2)(\rho_{L,n} C_{L,n} \vartheta_n) - (R_T^2 - R_{n+1}^2)(\rho_{L,n+1} C_{L,n+1} \vartheta_{n+1})] \quad (C.18)$$

Finally, at step $t = t_{n+1}$ there is a total mass of solute, M_{n+1}:

$$M_{n+1} = [\ \pi\ (R_T^2 - R_{n+1}^2)\ \rho_{L,n+1}\ C_{L,n+1}\ + \pi\ (R_{n+1}^2 - R_n^2)\ \rho_S\ k\ C_{L,n+1}\ ]\ V\ \Delta t\ . \quad (C.19)$$

A solute mass balance gives:

$$M_n - \Delta m_{diff} - \Delta m_{long} - \Delta m_{conv} - M_{n+1} = 0\ . \quad (C.20)$$

This equation contains two unknowns, R_{n+1} and ϑ_{n+1}. A second relationship between these variables is obtained by performing a global mass balance over the volume element:

$$\pi\ V\ \Delta t\ [\ (R_T^2 - R_n^2)\rho_{L,n} - (R_T^2 - R_{n+1}^2)\rho_{L,n+1} - (R_{n+1}^2 - R_n^2)\ \rho_S\ ]$$

$$- \pi\ \Delta t\ [(R_T^2 - R_n^2)\rho_{L,n}\vartheta_n - (R_T^2 - R_{n+1}^2)\rho_{L,n+1}\vartheta_{n+1}\ ] = 0\ . \quad (C.21)$$

Both mass balance equations are nonlinear in the unknown variables, R_{n+1} and ϑ_{n+1}. A Newton-Raphson iteration, using the Jacobian matrix for the mass balance equations, is used to solve for R_{n+1} and ϑ_{n+1} [104 , 105] [104 , 105].

New solid node compositions are calculated utilizing a three point Newton's interpolation formula with divided differences [104] for the previous node point, last interface position and current interface position.

The primary solidification portion of this program terminates when the volume element is fully solid, or when the eutectic temperature is reached. At the eutectic temperature, any remaining liquid is solidified with an average solid composition composition C_{SE} given by:

$$C_{SE} = C_E + a\, C_0 \quad , \tag{C.22}$$

where C_E is the eutectic composition and a is the Bower, Brody and Flemings [54] cellular solidification parameter, defined in equation 2.13. The fraction eutectic formed is recorded, and the calculated intercellular liquid velocity, ϑ, at the cell root is compared to the physically necessary velocity. If this difference is greater than a preset tolerance, the estimate of liquid velocity at the tip is refined, and the program performs another iteration. When the intercellular liquid velocity at the root respects conservation of matter as given by equation 3.32, the average solid composition is calculated and compared to the nominal composition. If the discrepancy is greater than a defined tolerance, the tip temperature is adjusted, and the calculation reiterated.

C.5 Results

This model was tested by considering whether its behavior is appropriate in several limiting cases. With no diffusion in the solid, the model gives results that very closely approach the BBF equation [54], differing from analytical results by one part in 10^8 for composition. Computed result

accuracy improves as mesh size decreases. Growth conditions for cellular solidification and complete diffusion in the solid give model results that approach the analytical expression developed for equilibrium cellular solidification, equation 3.16.

Finite difference constants used in this analysis were varied to determine their effects on numerical results. A summary of these variations is given in Table C1. The test case used corresponds to unreinforced solidification conditions for Sample 209, where G = 21300 K/m, V = 3.14 μm/s and r_T = 47 μm. The program was tested with 50, 100 and 200 radial increments. There was a 3.5% difference in the magnitude of computed eutectic fraction for 50 and 100 increment runs. The 100 and 200 increment runs showed less than one percent difference in computed eutectic fraction. The results presented in this thesis used 100 radial increments. X, the finite difference time step parameter, was varied from 0.05 to 0.5. Between 0.5 and 0.2, there was no significant difference in results. Above X = 0.25, the program was found to become unstable, as expected from the form of equation (C.3). The value for X used in this work was 0.1.

An adjustable offset associated with $\delta\rho^*$ is maintained, allowing the last increment to range from 0 to 1 radial increments when no offset is specified to 0.5 to 1.5 radial increments, for example, if a value of 0.5 is chosen. The offset for $\delta\rho^*$ was varied and no significant differences were noted between 0.15 and 0.5. Below $\delta\rho^* = 0.1$, $\alpha = \delta\rho^*/\Delta\rho$ may be very small, and coefficients in equation (C.6) very large, leading to instabilities in the solution. An offset value of 0.2 was chosen to eliminate this problem.

The Newton-Raphson iteration used to find new interface positions converged very rapidly to correct values. Making the tolerance for successive iterations two orders of magnitude more restrictive had no effect on the first eight significant figures of computed final concentration. Similarly, the tolerance on

intercellular liquid velocity was varied by two orders of magnitude, with little effect on final results. For both tolerances a value of 10^{-10} was used.

The program was written in the C programming language, and run on an HP/Apollo 12000DN multiprocessor workstation. Execution times for a single run were on the order of several minutes to several hours, and depended strongly on specified cooling rate and cell radius.

The program listing follows. All variables are defined as they are declared. An attempt was made to give the functions names representative of the tasks which they perform. A description of what each function does is present at its beginning.

Table C1

Effect of Program Parameters on Final Results

Mesh Points	X	$\delta\rho^*$	$g_{eutectic}$	C_{max}/C_{min}
100	0.1	0.2	0.031917	13.00046
200	0.1	0.2	0.031688	13.00876
50	0.1	0.2	0.033034	12.96709
100	0.2	0.2	0.032129	12.98997
100	0.05	0.2	0.031769	13.00413
100	0.1	0.1	0.031910	13.00042
100	0.1	0.5	0.032014	13.00069

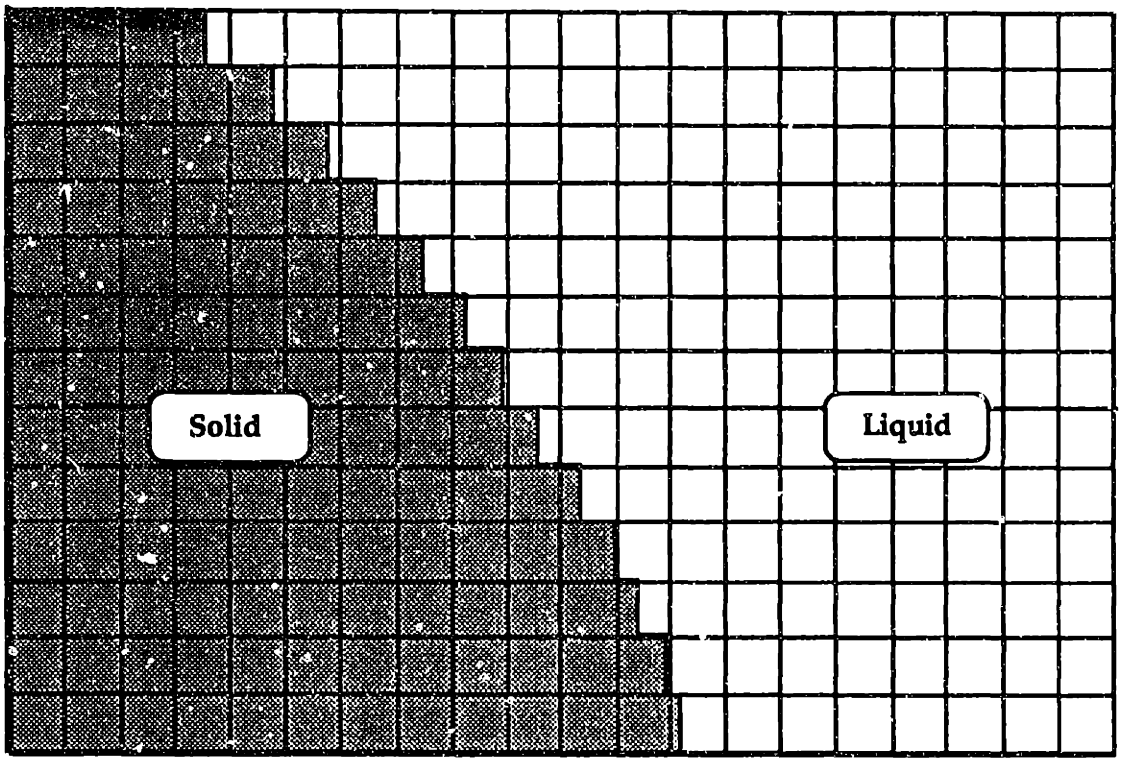

(a)

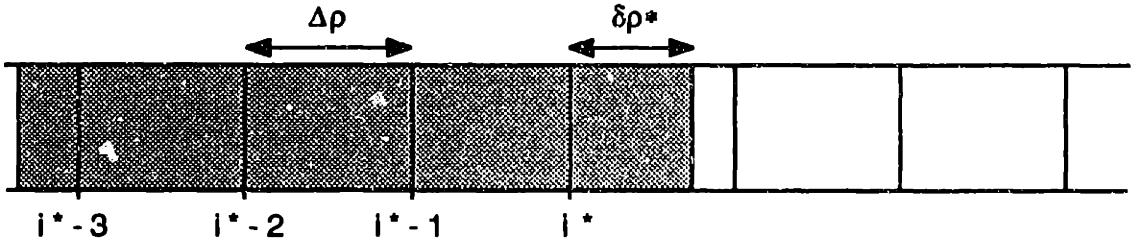

(b)

Figure C.1 (a) Discretization of cell shape in finite difference program. (b) Magnification of volume element for one iteration showing location of the interface and definition of mesh labels, i^*, and radial increments $\Delta\phi$ and $\delta\phi^*$.

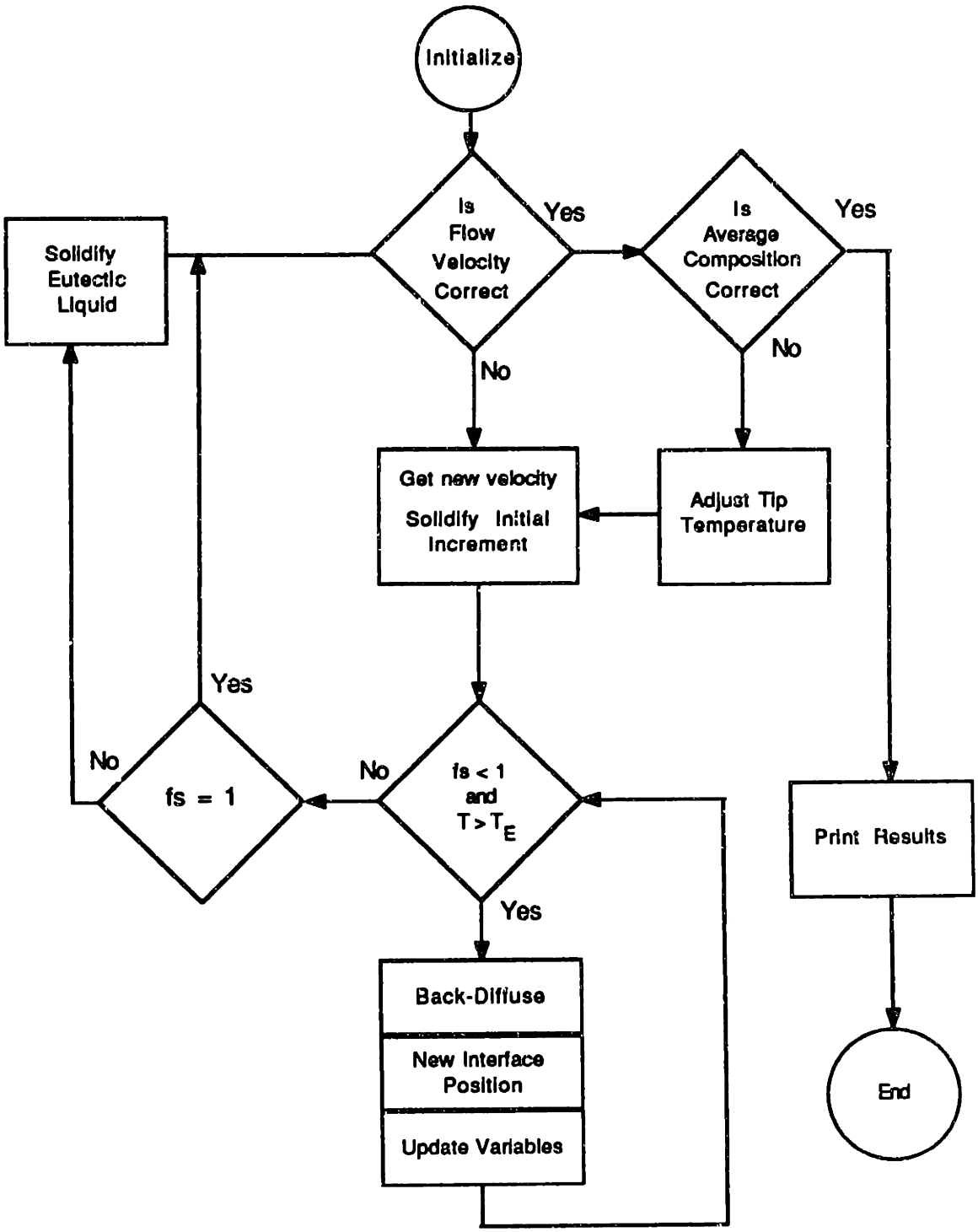

Figure C.2 General flow chart for finite difference program

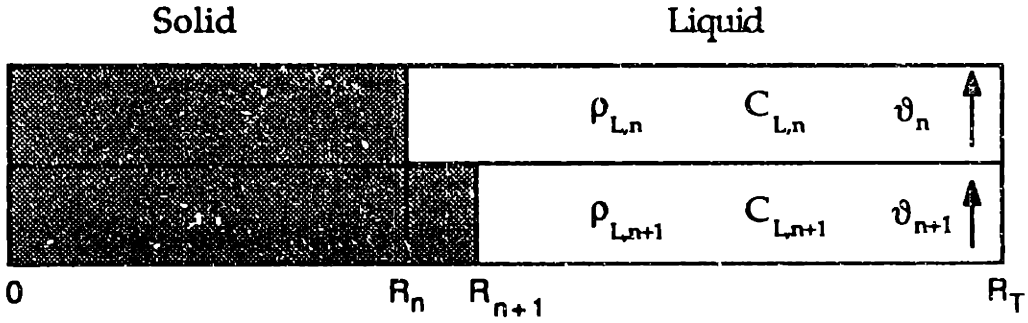

(a)

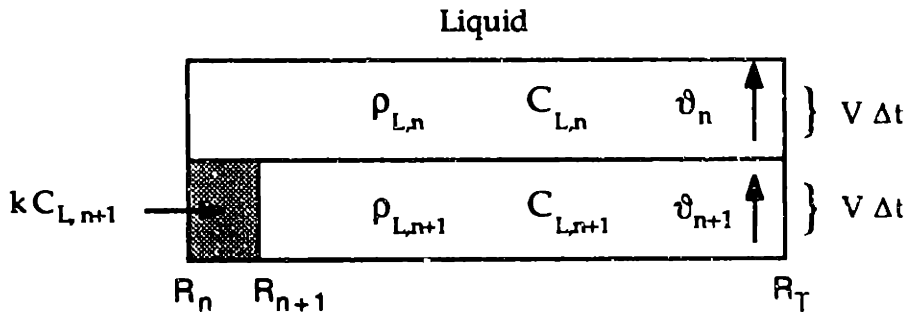

(b)

$\rho_{L,n}$, $\rho_{L,n+1}$ = Density of Liquid

$C_{L,n}$, $C_{L,n+1}$ = Composition of Liquid

ϑ_n, ϑ_{n+1} = Flow Velocity of Liquid

R_n = Radius of Solid Before Incremental Solidification

R_{n+1} = Radius of Solid After Incremental Solidification

R_T = Radius of Volume Element

Figure C.3 Successive volume elements showing variables used for mass balances.

```
/************************    cellsolid.c    ***************************/
/* This program is designed to cacluate the steady state              */
/* solidification shape for cells (or average shape for               */
/* dendrites). Solid state diffusion is considered. The               */
/* concentration profiles at any point in the solidification          */
/* process are also determined.                                       */
/*                                                                    */
/* Nancy Dean,   August, 1991                                         */

#include <stdio.h>
#include <math.h>
 double pow();
 double sqrt();

/******************** Material Constants **********************/

#define c0 4.5                          /*  Average Composition, wt%     */
#define tm 660.0                        /*  Melting Temp of pure solvent */
#define eutect_temp 548.0               /*  Eutectic temperature, K      */
#define eutectic_comp 33.0              /*  Eutectic Composition         */
#define gradient 21300.0                /*  Thermal gradient  K/m        */
#define growth_rate 3.4e-6              /*  Growth rate, m/s             */
#define diffl 5.0e-9                    /*  Liquid diffusivity, m2/sec   */
#define radius 42.5e-6                  /*  radius of cell, m            */
#define sample 209                      /*   sample number               */

/******************* Finite Difference Constants ***************/

#define RSTEPS  101                     /*  number of radial increments   */
#define PRINT_INTERVAL 40000000         /*  cycles to skip before printing */
#define MAXCYCLE 3e9                    /* maximum finite difference cycles*/
#define MAXJCYCLE 200                   /*  maximum Jacobian iterations  */
#define MAXSCYCLE 50                    /*  maximum solute consv. cycles */
#define X  1.0e-1                       /*  del T/ (del R)2 in finite diff */
#define DEL_CRIT 0.00                   /*  used in calculating new inter.
pos.*/
#define pi 3.1415926535
#define OFFSET 0.2                  /*  fraction mesh interval del_rho starts
at*/
#define TRUE 1
#define FALSE 0

#define TIP 0                           /*  array index for tip velocity   */
#define ROOT 1                          /*  array index for root velocity */
#define TTEMP 2                         /*  array index for tip temperature*/
#define R_TOLERANCE 1e-9                /*  on Rn for Jacobian iteration  */
```

```
#define FLOW_TOLERANCE 1e-10          /* on Vn for Jaco iteration      */
#define SOLUTE_TOLERANCE 0.002        /* on average comp.              */
#define RT 1.00000                    /*  Normalized cell radius       */

/************************  Functions  ***************************/
void print_results();
void print_temps();
void back_diffuse();
int still_liquid();
void grow();
double new_interface_position();
void update_variables();
double interpolation();
double integrated();
void solidify_all();
void reset_variables();
void initialize();
void solidify_initial_increment();
double new_v_tip();
int inconsistent_flow();
double integrated_solute_profile();

/************************  Variables  ***************************/
double
 comp[RSTEPS],                        /*  array of solid compositions   */
 comp_diff[RSTEPS],                   /*  difference between iterations */
 mass_diff[RSTEPS],
 old_cl,                              /*  uniform composition in liquid
                                      */
 c,                                   /*  dimensionless composition     */
 average_comp,                        /*  in fully solid slice          */
 diff_solid,                          /*  diffusivity  m2/sec  f(T)     */
 change_comp,                         /*  during solid-state diffusion  */
 temperature,                         /*  interface temperature, C      */
 inter_temp[RSTEPS],          /*  array of temp when a new node is made
*/
 tip_temp,                            /*  temperature at the cell tip   */
 temp95,                              /*  temperature at which fs =0.95 */
 a,                                   /*  cell undercooling parameter   */
 fs,                                  /*  fraction solid                */
 fs_eutect,                           /*  fraction of eutectic          */
 time,                                /*  local time during soldification
step */
 rho,                                 /*  interface position, rad
increments */
 new_vliq,                            /*  velocity of liquid at n+1 step  */
```

```
 old_vliq,                          /*  velocity of liquid at n step     */
 v_tip,                             /*  velocity of liquid at cell tips  */
 v_root_calc,                       /*  calculated flow vel. in last
element*/
 v_root_actual,                     /*  physical flow vel. inlast
element
                                    */
 v_eutectic,                        /*  liquid ve. at eutectic root      */
 vliqs[RSTEPS],                     /*  array of liquid velocities       */
 upper_bound[3],                    /*  of intercellular liquid velocity*/
 lower_bound[3],                    /*  of intercellular liquid velocity*/
 rad_inc,                           /*  reciprocal of number of radial
steps */
 del_rho,                           /*  position of interface beyond     */
                                    /*  istar * rad_inc.  < rad_inc      */
 del_offset,                        /*  actaul offset distance           */
 delta_ti,                          /*  time increment                   */
 delta_temp,                        /*  temperature drop during
delta_ti */
 delta_mdiff,                       /*  solute absorbed during
diffusion
                                    */
 new_cl,                            /*  new liquid composition, wt%*/
 cs,                                /*  solid composition, wt% Cu        */
 cs_eutectic,                       /*  eutectic solid composition       */
 ml,                                /*  liquidus slope, K/wt%            */
 b,                                 /*  distance interface moves
during*/
                                    /*  growth for each step             */
 ps,                                /*  density in solid, g/cm3          */
 ps_eutect,                         /*  density of eutectic solid        */
 pl,                                /*  density in liquid, g/cm3         */
 pl_new,                            /*  density in liquid, n+1 step      */
 pl_eutect,                         /*  density of eutectic liquid       */
  total_solute,                     /*   integration of solute profile   */
 k;                                 /*  partition ratio  = cs/cl         */

int
 i_init,                            /*  nodes initially solidified       */
 istar,                             /*  node before liquid-solid
interface*/
 old_istar,                         /*  node before eutectic solid       */
 cycle,                             /*  cycle number in finite diff      */
 vcycle,                            /*  tip velocity iterations          */
 scycle,                            /*  tip temperature cycle            */
  make_new_temp,                    /*  when to add a new element to
                                    */
                                    /*  interface temperature array      */
```

```
  solute_not_conserved,                    /*  solute concentration = Co ?   */
  first_time_through;                      /*  if initial time through loop  */

/*********************  print_results  ***********************/
/*  Print the composition profile at a given time                */

void print_results()
{ int i;
    printf("time = %12.8f  cycle = %5d\n", time, cycle);
    printf("liquid compositon/(c0) = %10.8f     temperature = %9.5f\n",
                                                 new_cl, temperature);
    printf("interface position = %10.8f  fraction solid = %10.6f\n\n", rho, fs);
    printf("  i \t radial position(microns) \tcomposition/(c0)       \n");
    for (i = 0; i <= istar; i++)
       printf("%3d \t %14.5f \t %20.8f\n", i, i*rad_inc*radius*1e6, comp[i]);
     printf("interface     %9.5f\t\t\t %12.8f\n",rho*radius*1e6,k*new_cl);
     printf("\n\n\n\n\n\n");

}  /*  print_results   */

/*********************  print_temps     ***********************/
/*   Print the interface temperature for various fraction solids      */

void print_temps()
{ int i;
   printf(" i \tfraction solid          temperature \n");
   for (i = 0; i < RSTEPS; i++)
      printf("%3d\t%12.9f \t \t %12.5f \n", i, i*i*rad_inc*rad_inc,
                    inter_temp[i]);
    printf("\n\n");

   printf(" i \tfraction solid          liquid velocity \n");
   for (i = 0; i < RSTEPS; i++)
     printf("%3d\t%12.9f \t \t %12.5e \n", i, i*i*rad_inc*rad_inc, vliqs[i]);
    printf("\n\n");

    printf("Sample %4d\n", sample);
    printf("Thermal Gradient = %8.0f  K/m\n", gradient);
    printf("Growth Rate = %6.4f  micrometers/sec\n", growth_rate*1e6);
    printf("Cell Radius = %6.4f  micrometers\n", radius*1e6);
    printf("Composition = %6.4f  liquid diffusivity = %5.4e\n", c0, diffl);
    printf("Eutectic solid comp = %12.6f\n\n", cs_eutectic);
    printf("Liquid flow velocity at tip = %8.4e\n", v_tip);
    printf("Liquid flow velocity at root = %8.4e\n", v_root_calc);
   printf("cycle = %12d   v cycle = %12d\n", cycle, vcycle);
    printf("solute conservation cycles = %5d\n\n", scycle);
```

```
    printf("X = %6.3f  Increments = %8d\n", X, RSTEPS-1);
    printf("offset = %8.4f\n", OFFSET);
    printf("radius tolerance = %6.3e    flow toler. = %6.3e\n\n",
                        R_TOLERANCE, FLOW_TOLERANCE);
    printf("tip temperature = %12.8f\n", tip_temp);
    printf("average composition/c0 = %12.8f\n", total_solute/ps);
    printf("final temperature = %10.5f\n", temperature);
    printf("Temperature for 0.95 fraction solid =  %10.5f\n", temp95);

    printf("fraction eutectic =%12.8f\n", fs_eutect);
    printf("composition ratio = %12.8f \n\n", comp[0]/comp[RSTEPS - 1]);
    printf("-------------------------------------------------------\n\n\n");

}   /* print_temps */

/*********************  back_diffuse  ***************************/
/* Finite difference scheme for diffusion in the solid.          */
/* Standard finite difference equation for radial diffusion in   */
/* a cylinder are used for all points but the one nearest the    */
/* interface, (i*).  Since there is not an equidistant array     */
/* point on the other side of i*, a special case must be used.   */

void back_diffuse(z)
int z;        /*  z = istar  */
{ double
     old_comp[RSTEPS],
     theta;                  /* fraction of radial increment del_rho is */
  int i;

    theta = del_rho/rad_inc;

    for (i= 0; i<= z; i++)              /* change current comps to old comps */
     old_comp[i] = comp[i];

    /* explicit finite difference for cylinder */

     comp[0] = old_comp[0] + 4 * X * (old_comp[1] - old_comp[0]);
     for (i = 1; i < z; i++)
         comp[i] = old_comp[i] + (X/(2*i)) * ((2*i + 1) * old_comp[i+1]
                          - 4 * i * old_comp[i]  +  (2*i - 1) * old_comp[i-1]);

    /*  special case for istar  */
     comp[z] = old_comp[z] +  X * (1.0/z) *
                          ((k * new_cl) * (2*z + 1)/(theta *(theta + 1.0))
                               - old_comp[z] * ((2*z +1.0 - theta)/theta)
                                 + old_comp[z-1] * ((2*z -theta)/(theta + 1.0)));
```

```
    for (i = 0; i <= z; i++) {
      comp_diff[i] = comp[i] - old_comp[i];
      mass_diff[i] = ps * comp_diff[i];     }

                                        /* integrate change in composition profile */
    delta_mdiff = integrated(mass_diff, z);

  }   /* back_diffuse */

/********************  still_liquid  ***************************/
/* Determines if there is still some liquid left by checking      */
/* that the fraction solid is less than one and that the liquid   */
/* composition has not reached the eutectic composition.          */

int still_liquid()

{ return  ((fs < 1.0) && (old_cl < eutectic_comp/c0));}

   /*still_liquid */

/*****************************  grow  ************************/
/* Advances the interface by an amount determined by a mass   */
/* balance in the liquid volume element, accounting for solute  */
/* lost to diffusion in the solid, composition increase in liquid  */
/* as temp drops and longitudinal diffusion in the liquid.        */
/*                                                                */
/*  The liquid composition is updated                             */

void grow()

{ double new_rho;          /* new interface position  */
  int  n;

/* Get time increment for this step.  Use it to update time and   */
/* calculate a new delta liquid composition.  Delta T, the        */
/* dimensionless time, is constant.  However. T depends on Dsolid*/
/* and time so the time for each interval increases as the         */
/* diffusivity decreases.                                         */

  delta_ti = (X/diff_solid) * (pow((rad_inc * radius) , 2.0));
  delta_temp = gradient * growth_rate * delta_ti;

  update_variables();

/* get new liquid composition based on the temperature.  also   */
```

```
/* will determine new values for densities and k.                    */

  new_rho = new_interface_position();
 if ((new_rho > 0.95) && (rho < 0.95))      temp95 = temperature;

 b = new_rho - rho;                    /* amount interface moves      */
 fs = new_rho * new_rho;                 /* new fraction solid        */
rho = new_rho;                        /* assign new interface position */

/*  Interface must be advanced an amount consistent with             */
/*  compositional changes.  Mass balance on pages 3-6 done in        */
/*  new_interface_position.   b = amount interface advances.         */

/*  Adjust del_rho.  If necessary create new node points with        */
/*  compositions based on divided differences interpolation.         */
/*  The following formula will work even if b is more than one       */
/*  radial increment,  useful if growth jumps can be large           */
/*  relative to the radial increment.                                */

    n = 0;
    while (n < (floor ((del_rho + b - del_offset)/rad_inc)))     {
          /*  This kicks in when a new solid node needs to be formed */
         n = n+1;
          comp[istar + n] = interpolation(n*rad_inc);
          make_new_temp = TRUE;         }

    del_rho = del_rho + b - n * rad_inc;      /* change del_rho if n not 0 */
   istar = istar + n;                    /* change istar if new node created*/

     /*  This next block corrects for new solid nodes not forming until the */
     /*  the offset del_rho is passed.  Temperature is recorded when the     */
     /* interface passes a node point, not when a new node is created        */

     if ((make_new_temp) && ((del_rho + b) > rad_inc))  {
           inter_temp[istar + 1] = temperature;
           vliqs[istar+1] = new_vliq;
            make_new_temp = FALSE;
          while (n > 0) {
                n = n - 1;
                 inter_temp[istar + 1 - n] = temperature;
                 vliqs[istar + 1 - n] = new_vliq;       }      }

}   /* grow  */

/******************  new_interface_position     *****************/
/* Calculate the new interface position, based on a balance of       */
```

```
/* copper and total mass at the interface. The balance gives a      */
/* set of nonlinear equations in the new interface position and     */
/* the bulk liquid velocity between the cells. The series of        */
/* nonlinear equations are solved by a Newton-Raphson method */
/* using the Jacobian matrix.                                       */

double new_interface_position()
{ double
   f1,                  /* function representing Cu mass balance  */
   f2,                  /* function for overall mass balance      */
   j11,                 /* df1/dr2, element of jacobian matrix    */
   j12,                 /* df1/dv, element of jacobian matrix     */
   j21,                 /* df2/dr2, element of jacobian matrix    */
   j22,                 /* df2/dv, element of jacobian matrix     */
   determ,              /* determinant of jacobian matrix         */
   a1,b1,c1,d1,         /* coefficients of ax + bxy + cy + d =0 for f1 */
   a2,b2,c2,d2,         /* coefficients of ax + bxy + cy + d =0 for f2 */
   deltarsqd,           /* change in guess for r(n+!) squared     */
   deltav,              /* change in guess for bulk vliq(n+1)     */
   new_rsqd,            /* new value for R(n+1) squared           */
   new_r;               /* new value for R(n+1), value is returned */

int jcycle;

/* coefficients a1, b1, c1, d1, a2, b2, c2, d2 are from mass balance  */
/* derivations are in lab notebook                                    */

  a1 = diffl*gradient/(ml* growth_rate * c0) * pl_new
                                + new_cl* (pl_new - ps*k);
  b1 = - new_cl * pl_new/growth_rate;
  c1 = RT*RT * new_cl * pl_new/growth_rate;

  d1 = (RT*RT - rho*rho)*pl*old_cl - delta_mdiff/pi
    +  diffl*gradient/(ml*growth_rate * c0)*((RT*RT - rho*rho)*pl -
                          RT*RT*pl_new)
    - (pl * old_cl * old_vliq/growth_rate) * (RT*RT - rho*rho)
    - RT*RT * pl_new * new_cl + rho*rho * ps * k * new_cl;

  a2 = growth_rate * (pl_new - ps);
  b2 = - pl_new;
  c2 = RT*RT*pl_new;
  d2 = - (RT*RT - rho*rho)*pl*old_vliq + RT*RT*growth_rate*(pl-pl_new)
     - rho*rho*growth_rate*(pl-ps);

/* let initial guesses for R(n+1) and velocity of liquid be the       */
/* values determined for time step n. These estimates should be*/
```

```
/* very close to    ual values. That is, they shouldn't change     */
/* too quickly.                                                    */

 new_rsqd = rho * rho;
 new_vliq = old_vliq;

/* until solution is within specified tolerances repeat the        */
/* Newton-Raphson iteration                                        */
 jcycle = 0;

while (jcycle < MAXJCYCLE)  {
    /* calculate function values and derivatives using the estimated values */

   f1 = a1*new_rsqd + b1*new_rsqd*new_vliq + c1*new_vliq + d1;
   f2 = a2*new_rsqd + b2*new_rsqd*new_vliq + c2*new_vliq + d2;

   j11 = a1 + b1*new_vliq;
   j12 = b1*new_rsqd + c1;
   j21 = a2 + b2*new_vliq;
   j22 = b2*new_rsqd + c2;

   determ = j11*j22 - j12*j21;                  /* determinant of Jacobian matrix */
   if (determ == 0.000000)  break;

   deltarsqd = (j22*f1 - j12*f2)/determ;    /* calculate the "error" in estimate */
   deltav = (j11*f2 - j21*f1)/determ;

   new_rsqd = new_rsqd - deltarsqd;             /* update estimate */
   new_vliq = new_vliq - deltav;                /* update estimate */

   if ((fabs(deltarsqd) < R_TOLERANCE) && (fabs(deltav) < R_TOLERANCE))
     break;      /* stop iterations if solution is within tolerance */

   if ((jcycle>20) && (new_rsqd > 0.9999)) {     /* if too many cycles */
     new_rsqd = 1.0;                          /* and fs is stuck near one */
     new_vliq = old_vliq;                        /*  let fs = 1             */
    break; }

  jcycle++;                                      /* increment counter */
 }    /* while loop */

 if ((new_rsqd > 1.0) | | (jcycle >= MAXJCYCLE))  {
   new_rsqd = 1.00;
    new_vliq = old_vliq;
   comp[RSTEPS - 1] = k * new_cl;        }
```

```
 new_vliq = new_vliq;
 new_r = sqrt(new_rsqd);                    /* assign new values */

 return new_r;                    /* return new interface position */

} /* new_interface_position */

/********************** update variables **********************/
/* update temperature, time, liquid composition,densities       */

void update_variables()
{ time = time + delta_ti;
  temperature = temperature - delta_temp;
  diff_solid = 0.29e-4 * exp(-15700.0/(temperature + 273.13));

  old_cl = new_cl;
  new_cl = (temperature - tm)/(ml*c0);
  cs = k * new_cl;

   pl = pl_new;
   ps = 2.660;
    pl_new = 2.39504101 + 0.016953298*c0*new_cl +
                          0.000270592*new_cl*new_cl*c0*c0;

     old_vliq = new_vliq;

}    /*update_variables */

/************************** interpolation  ********************/
/* When a new solid node composition is needed, the function  */
/* will use a three point LaGrange interpolation. The points are*/
/* the last known node concentration, the old interface, and the */
/* new interface. If the old interface was too close to the last  */
/* known node, c[i*], then only two points are used for the       */
/* interpolation. The value at a distance x from the last known  */
/* node point is returned.                                        */

double interpolation(x)
double x;                    /* distance from the first point used in*/
{                            /* interpolation, comp[istar].          */
 double
   w,                        /* coefficient of x squared in interpolation */
   f;                        /* interpolated composition at distance x  */

  if (del_rho > DEL_CRIT)
   {  w = ((k*new_cl - k*old_cl)/b - (k*old_cl - comp[istar])/del_rho)/
```

```
                                        (del_rho + b);
    f = w * x * x  +  ((k * old_cl - comp[istar])/del_rho - del_rho* w) * x
                                        + comp[istar];      }
 else
   f = comp[istar]  +   ((k*new_cl - comp[istar])/(del_rho + b)) * x;

 return f;                      /*  new node point composition */

}  /* interpolation */

/*************************  solidify_all  ********************/
/* The remainder of the sample is solidified, with all          */
/* unassigned nodes set equal to the eutectic solid concentration.*/
/* The location of the interface for this last step is also printed.  */

void solidify_all()
{  int i;

 cs_eutectic = (eutectic_comp + a * c0)/c0;      /* set eutectic comp        */
 fs_eutect = 1 - fs;                             /* calc fraction eutectic   */
 for (i =(istar +1); i < RSTEPS ; i++)   {
  comp[i] = cs_eutectic;                         /* set node points to Cse   */
  inter_temp[i] = eutect_temp;  }                /* set temps to Teutect     */

 old_istar = istar;                              /*  change finite difference*/
 istar = RSTEPS -1 ;                             /* variables                */
 fs = 1.000;
 del_rho = 0;

 }  /* solidify_all  */

/*************************  integrated  ***************************/
/* Integrates a function, represented by array passed in, between     */
/* zero and the end point. Trapezoid rule with end correction         */
/* is used. The error in this formula is of O(h4), where h is the     */
/* interval size. If del_rho is not zero, an extra term is added on   */
/* Note this function is used to calculate the solute absorbed        */
/* during diffusion as well as to check the overall composition.      */

double integrated(f, w)
double  f[RSTEPS];                      /* function to be integrated */
int  w;                                 /* end point for integration */

{ double
   trapezoid,                  /* Value for trapeziodal rule + corrections*/
   end_correct,                        /* End correction term          */
```

```
  del_correct,              /* Correction due to del_rho not being zero*/
  sum;                      /* summation in body of trapeziod rule  */
 int i;

 sum = 0.0;                                              /* summation */
 sum = sum + 0.5 * 2.0 * pi * 0 * rad_inc * f[0];        /* initial term */
 for (i=1; i < w ; i++)
        sum = sum + 2 * pi * i * rad_inc  * f[i];
 sum = sum + 0.5 * 2 * pi * w * rad_inc * f[w];          /* final term */
 sum = sum * rad_inc;

 end_correct = (rad_inc*rad_inc/12) *          /* derivatives at ends */
                2*pi *(f[0] - f[w] -  (w * (f[w] - f[w-1])));
 del_correct = pi * rad_inc * del_rho * w * f[w];

 trapezoid = sum + end_correct + del_correct;

 return trapezoid;          /* value of integral using trapezoid rule */

} /* integrated */

/*********************  reset_variables  *********************/
/* reset variables for next iteration of solidification with      */
/* different flow velocity at the tip.                            */

void reset_variables()
{ int i;
/*  set up variables related to processing conditions, and initialize */
/*  other variables.                                  */

   new_cl = 1 - a;
   istar =i_init - 1;
   time = 0;
   rho = 0.0;
   fs_eutect = 0.0;

   for (i = 0; i < RSTEPS; i++)  {
    comp[i] = 0.0;
     inter_temp[i] = 0.0;
    vliqs[i] = 0.0;  }

  cycle = 0;
    make_new_temp = TRUE;
    new_vliq = old_vliq = v_tip;

} /* set_up */
```

```
/********************  initialize  ***************************/
/*  set up variables for main part of program.                */

void initialize()    {

/*   set up variables related to processing comditions, and initialize */
/*   other variables.                                          */

   ml = -3.39393939;
   k = 0.17121212;
    a = diffl * gradient / (c0 * growth_rate * ml);
    tip_temp = tm +(1 - a)*c0 * ml;
   c = c0/c0;

   scycle = 0;
    i_init = 3;
   rad_inc = 1.0/(RSTEPS - 1.0);
    del_offset = OFFSET * rad_inc;
    cs_eutectic = (eutectic_comp + a*c0)/c0;
   ps = 2.660;

   temp95 = eutect_temp;                          /* default value */
    v_tip = 0.0;

    pl_eutect = 3.2481721;
    ps_eutect = 2.577 + 1.740e-2 * cs_eutectic*c0
              + 2.241e-4 * cs_eutectic*cs_eutectic*c0*c0;
     v_eutectic = growth_rate* (pl_eutect - ps_eutect)/pl_eutect;

    upper_bound[TIP] = upper_bound[ROOT] = growth_rate;
    lower_bound[TIP] = lower_bound[ROOT] = -growth_rate;

   upper_bound[TTEMP] = tm + ml*c0;                 /* liquidus  */
   lower_bound[TTEMP] = tm + ml*c0/k;               /* solidus   */

     solute_not_conserved = TRUE;
     first_time_through  = TRUE;
     v_root_actual = v_eutectic;
     v_root_calc = growth_rate;

}  /* initialize */

/***************  solidify_initial_increment  ****************/
/*   Solidify first increment to allow finite difference to be used.  */
/*   amount solidified can be varied by changing i_init, the          */
/*   number of elements to be solidified.                             */
```

```
void  solidify_initial_increment()
{   int i;

    a = 1 - (tip_temp - tm)/(ml*c0);      /*  set an effective a for the BBF */
                                           /* equation to allow for convective*/
    for (i= 0; i< i_init; i++)  {          /* undercoolings. Solidify according */
     fs = i*rad_inc * (i*rad_inc);                                  /* to BBF */
     comp[i] = k*c * (a/(k-1) + (1-a*k/(k-1))*(pow((1-fs),(k-1))));
      inter_temp[i] = tip_temp;
     vliqs[i] = v_tip;                    }

/*   Update values of variables corresponding to the amount initially */
/*  solidified.                                  */

    new_cl = old_cl = comp[istar]/k;
     temperature = tm + ml * (new_cl * c0);
     time = (tip_temp - temperature)/(gradient * growth_rate);
    diff_solid = .29e-4 * exp(-15700.0/(temperature + 273.13));

/*   allow for the interface to be between the OFFSET and 1+OFFSET    */
/*   away from the last node point. Initially, there must be at least    */
/*   three nodes solidified inoreder to have two nodes left to use    */
/*   the finite difference equation for i = 0. The last composition    */
/*   is deleted from the array ( to be updated including diffusion    */
/*   later), istar is decremented and the interval beyond the last    */
/*   node point, del_rho is set to be one node spacing.    */

   comp[istar] = 0.0;
   istar = istar - 1;
    del_rho = rad_inc;

    a = diffl * gradient / (ml * c0 * growth_rate);          /* reset a */

/*   set the current interface location    */

    rho = istar*rad_inc + del_rho;
    pl_new =2.39504101 + 0.016953298*c0*new_cl
            + 0.000270592*new_cl*new_cl*c0*c0;

}  /* solidify_initial_increment */

/******************  inconsistent_flow  **********************/
/* check to see if liquid flow, or velocity at the cell tip          */
/* is what is required to account for shrinkage or expansion         */
/* of the last volume element upon solidification                    */
```

```
int inconsistent_flow()
{ return (fabs(v_root_calc - v_root_actual) > FLOW_TOLERANCE); }

/* inconsistent_flow */
/************************  new_v_tip   ************************/

double new_v_tip()
{double vstart_guess,
      slope;

 if (first_time_through)  {
    vstart_guess = v_tip;
    first_time_through = FALSE; }

 else {
   if (v_root_calc > v_root_actual)
    { upper_bound[TIP] = v_tip;
      upper_bound[ROOT] = v_root_calc; }
  else
    { lower_bound[TIP] = v_tip;
      lower_bound[ROOT] = v_root_calc; }

   slope = (upper_bound[ROOT] - lower_bound[ROOT])
         /(upper_bound[TIP] - lower_bound[TIP]);

   if ((fabs(v_root_calc/v_root_actual) > 1.5) | |
                                    (v_root_calc/v_root_actual < 0))
    vstart_guess = (lower_bound[TIP] + upper_bound[TIP])/2.0;
   else
    vstart_guess = lower_bound[TIP] +
                   (v_root_actual -lower_bound[ROOT])/slope;
      }

return vstart_guess;                  /* return new tip velocity guess */

}  /* new_v_tip */
/*****************  integrated_solute_profile  ******************/
/* check to see if the fully solid material has a composition      */
/* equal to the nominal composition.                               */

double integrated_solute_profile()  {

double a1,                                          /*  primary solid */
    a2,                                               /*  eutectic    */
    a3;                                            /*  del contribution */
```

```
  if (fs_eutect == 0.0)          /* if there is no eutectic, just integrate */
    return ( ps * integrated(comp, RSTEPS -1)/pi);
  else {
    a1 =  ps * integrated(comp, old_istar)/pi;
    a2 =    fs_eutect * cs_eutectic * ps_eutect;
     a3 = (rho*rho - old_istar*old_istar*rad_inc*rad_inc) * ps * 0.5 *
                    (comp[old_istar] + k*(eutect_temp - tm)/(ml*c0));
    return (a1 + a2 + a3); }

} /* integrated_solute_profile  */

/************************  main  ******************************/

main()
 { setbuf(stdout, NULL);

   vcycle = 0;
   initialize();                                  /* initialize variables */

    while(solute_not_conserved) {
    scycle = scycle + 1;

     while(inconsistent_flow()) {

        v_tip = new_v_tip();
       reset_variables();
       vcycle = vcycle + 1;
       solidify_initial_increment();

   /*  Main part of program. Solid state diffusion takes place          */
   /*  followed by incremental growth, which takes into account the     */
   /*  solute absorbed during diffusion. System variables are updated   */
   /*  and the process repeats until the sample is fully solidified,    */
   /*  either by reaching the eutectic temperature or if the fraction   */
   /*  solid reaches unity.                                             */

       update_variables();

       while(still_liquid() && (cycle < MAXCYCLE)){
        cycle = cycle + 1;

        back_diffuse(istar);
       grow();

        if ((cycle % PRINT_INTERVAL) == 0)
```

```
        print_results() ;                                   } /* still_liquid loop*/

      if (temperature < eutect_temp)
        v_root_actual = v_eutectic;
      else v_root_actual = growth_rate*(pl -ps)/pl;  /* values at root used */

      v_root_calc = new_vliq;        /* last value calculated in iteration */

    }       /* while inconsistent_flow loop */

    if (fs < 1.0)       solidify_all();

     total_solute = integrated_solute_profile();
     printf("\nTip Temperature = %12.8f    Total Solute =  %12.8f\n\n",
             tip_temp, total_solute);

     if ((fabs((total_solute - ps)/ps)) < SOLUTE_TOLERANCE)
        solute_not_conserved = FALSE;
        else {
        solute_not_conserved = TRUE;
        first_time_through = TRUE;
        v_tip = 0.0;
        vcycle = 0;
        v_root_calc = 1.0 + v_root_actual;     /* make flow inconsistent */

        if (((total_solute-ps)/ps) > 0) {
          lower_bound[TTEMP] = tip_temp;
          tip_temp = tip_temp + 0.5 * (fabs((total_solute - ps)/ps)) *
                        (upper_bound[TTEMP] - lower_bound[TTEMP]);     }

        else {
          upper_bound[TTEMP] = tip_temp;
          tip_temp = tip_temp - 0.5 * (fabs((total_solute - ps)/ps)) *
                          (upper_bound[TTEMP] - lower_bound[TTEMP]);    }

        lower_bound[TIP] = lower_bound[ROOT] = -growth_rate;
        upper_bound[TIP] = upper_bound[ROOT] = growth_rate;
        if (scycle > MAXSCYCLE )    break;
              }  /* else loop */

    }  /* while solute_not_conserved loop */

print_results();      /* print out results when a consistent solution is reached*/
print_temps();

  }  /* MAIN */
```

Bibliography

1. Coriell, S.R., G.B. McFadden, and R.F. Sekerka, *Cellular Solidification During Directional Solidification*. Annual Review of Materials Science, 1985. **15**: p. 119-45.

2. Smialowski, M., *Einige Beobachtungen uber die Verteilung von Beimengungen in Metallkristallen*. Zeitschrift für Metallkunde, 1937. **29**: p. 133.

3. Pond, R.B. and S.W. Kessler, *Model for Dendrite Growth Form in Metals and Alloys*. Transactions of the Metallurgical Society of the AIME, 1951. **191**: p. 1156.

4. Blaha, F., *Uber einige Wachstumsstrukturen von aus der Schmelze erstarrten Metallkristallen*. Acta Physica Austriaca, 1953. **8**: p. 141.

5. Rutter, J.W. and B. Chalmers, *Prismatic Substructure*. Canadian Journal of Physics, 1953. **31**: p. 15-39.

6. Tiller, W.A., K.A. Jackson, J.W. Rutter, and B. Chalmers, *The Redistribution of Solute Atoms During the Solidification of Metals*. Acta Metallurgica, 1953. **1**: p. 428 - 437.

7. Mullins, W.W. and R.F. Sekerka, *Stability of a Planar Interface During Solidification of a Dilute Binary Alloy*. Journal of Applied Physics, 1964. **35**(2): p. 444-451.

8. Voronkov, V.V., *Conditions for Formation of Mosaic Structure on a Crystallization Front*. Fizika Tverdogo Tela, 1964. **6**: p. 2984.

9. Sekerka, R.F., *A Stability Function for Explicit Evaluation of the Mullins-Sekerka Interface Stability Criterion*. Journal of Applied Physics, 1965. **36**(1): p. 264-268.

10. Sekerka, R.F., *Morphological Stability*, in *Crystal Growth*, H.S. Peiser, Editor. 1967, Pergamon Press: Oxford. p. 691.

11. Delves, R.T., *The Theory of the Stability of the Solid-Liquid Interface under Constitutional Supercooling (I)*. Physics Status Solidi, 1966. **16**: p. 621 - 632.

12. Coriell, S.R. and R.F. Sekerka, *Effect of Convective Flow on Morphological Stability*. PhysicoChemical Hydrodynamics, 1981. **2**(4): p. 281-293.

13. Coriell, S.R. and R.F. Sekerka, *Oscillatory Morphological Instabilities due to Non-Equilibrium Segregation*. Journal of Crystal Growth, 1983. **61**: p. 499-508.

14. Coriell, S.R., G.B. McFadden, P.W. Voorhees, and R.F. Sekerka, *Stability of a Planar Interface During Directional Solidification of a Multicomponent System*. Journal of Crystal Growth, 1987. **82**: p. 295-302.

15. Coriell, S.R. and G.B. McFadden, *Bouyancy Effects on Morphological Stability During Directional Stability*. Journal of Crystal Growth, 1989. **94**: p. 513 - 521.

16. Coriell, S.R., G.B. McFadden, A.A. Wheeler, and D.T.J. Hurle, *The Effect of an Electric Field on the Morphological Stability of the Crystal-Melt Interface of a Binary Alloy. II Joule Heating and Thermoelectric Effects*. Journal of Crystal Growth, 1989. **94**: p. 334-346.

17. Coriell, S.R., G.B. McFadden, and R.F. Sekerka, *Effect of Anisotropic Thermal Conductivity on the Morphological Stability of a Binary Alloy*. Journal of Crystal Growth, 1990. **100**: p. 459-466.

18. Coriell, S.R. and R.F. Sekerka, *Morphological Stability Near a Grain Boundary Groove in a Solid-Liquid Interface during Solidification of a Pure Substance*. Journal of Crystal Growth, 1973. **19**: p. 90.

19. Coriell, S.R. and R.F. Sekerka, *Morphological Stability Near a Grain Boundary Groove in a Solid-Liquid Interface During Solidification of a Binary Alloy*. Journal of Crystal Growth, 1973. **19**: p. 285-293.

20. Vinals, J., R.F. Sekerka, and P.P. DeBroy, *Morphological Stability Analysis of Directional Solidification in Thin Samples with Lateral Heat Transfer*. Journal of Crystal Growth, 1988. **89**: p. 405-414.

21. Nandapurkar, P. and D.R. Poirier, *Heat of Mixing and Morpological Stability*. Journal of Crystal Growth, 1988. **92**: p. 88-96.

22. Hurle, D.T.J., *The Effect of Soret Diffusion on the Morphological Stability of a Binary Alloy Crystal*. Journal of Crystal Growth, 1983. **61**: p. 463-472.

23. Caroli, B., C. Caroli, and B. Roulet, *The Mullins Sekerka Instability in Directional Solidification of Thin Samples*. Journal of Crystal Growth, 1986. **76**: p. 31-49.

24. Chalmers, B., *Principles of Solidificaton*. 1964, New York: Wiley.

25. Flemings, M.C., *Solidification Processing*. 1974, New York: McGraw-Hill. 364.

26. Tiller, W.A. and J.W. Ritter, *The Effect of Growth Conditions upon the Solidification of a Binary Alloy*. Canadian Journal of Physics, 1956. **34**: p. 96.

27. Walton, D.A., W.A. Tiller, J.W. Rutter, and W.C. Winegard, *Instability of a Smooth Solid-Liquid Interface During Solidification*. Transactions of American Institute of Mining Metallurgical and Petroleum Engineers, 1955. **203**: p. 1023.

28. Cole, G.S. and W.C. Winegard, *The Transition from Plane to Cellular Interface in Solidifying Tin-Lead-Antimony Alloys*. Canadian Journal of Physics, 1964. **92**: p. 322.

29. Plaskett, T.S. and W.C. Winegard, *Cellular Growth in Tin Alloys*. Canadian Journal of Physics, 1959. **37**: p. 1555-1557.

30. Sato, T., K. Shibata, and G. Ohira, *Interfacial Wave of Maximum Growth Velocity at the Morphological Instability of the Planar Solid-Liquid Interface in the Solidification of Alloys*. Journal of Crystal Growth, 1977. **40**: p. 69-77.

31. Sato, T. and G. Ohira, *Stability of a Planar Solid-Liquid Interface During Unidirectional Solidification of Al-0.1wt% Cu Alloy*. Journal of Crystal Growth, 1977. **40**: p. 78-89.

32. Shibata, K., T. Sato, and G. Ohira, *Morphological Stabilities of Planar Solid-Liquid Interfaces During Unidriectional Solidification of Dilute Al-Ti and Al-Cr Alloys*. Journal of Crystal Growth, 1978. **44**: p. 419-434.

33. Jamgotchian, H., B. Billia, and L. Capella, *Unidirectional Growth of Dilute Bi-Sb Alloys*. Journal of Crystal Growth, 1983. **62**: p. 539-544.

34. Ayers, J.D. and R.J. Schaefer. *Morphological Instability at a Grain-Boundary Groove*. in *Solidification and Casting of Metals*. 1979. University of Sheffield: TMS.

35. deCheveigné, S., C. Guthman, and M.M. Lebrun, *Nature of the Transition of the Solidification Front of a Binary Mixture from a Planar to a Cellular Morphology*. Journal of Crystal Growth, 1985. **73**: p. 242.

36. Wollkind, D.J. and L.A. Segel, *A Nonlinear Stability Analysis of the Freezing of a Dilute Binary Solution*. Philos. Trans. Royal Society of London, 1970. **268**: p. 351-380.

37. Tarshis, L.A., *Interface Morphology Consideration During Solidificaton*. 1967, Stanford University: Stanford, CA.

38. Caroli, B., C. Caroli, and B. Roulet, J. Phys. Paris, 1982. **43**: p. 1767-80.

39. McFadden, G.B., S.R. Coriell, and R.F. Sekerka, *Effect of Surface Tension Anisotropy on Cellular Morphologies*. Journal of Crystal Growth, 1988. (91): p. 180-198.

40. Young, G.W., S.H. Davies, and K. Brattkus, *Anisotropic Interface Kinetics and Tilted Cells in Unidirectional Solidification*. Journal of Crystal Growth, 1987. **83**: p. 560-571.

41. Langer, J.S. and L.A. Turski, *Studies in the Theory of Interfacial Stability -I. Stationary Symmetric Model*. Acta Metallurgica, 1977. **25**: p. 1113-1119.

42. Langer, J.S., *Studies in the Theory of Interfacial Stability - II. Moving Symmetric Model*. Acta Metallurgica, 1977. **25**: p. 1121-37.

43. Dee, G. and R. Mathur, *Cellular Patterns Produced by the Directional Solidification of a Binary Alloy*. Physical Reviews B, 1983. **27**: p. 7073-92.

44. Dee, G., *A Numerical Approach to Directional Solidification*. Physica, 1984. **12D**: p. 270-278.

45. McFadden, G.B. and S. Coriell, Physica, 1984. **12D**: p. 253-61.

46. Ungar, L.H. and R.A. Brown, *Cellular Interface Morphologies in Directional Solidification. The One-Sided Model*. Physical Review B, 1984. **29**(3): p. 1367-1380.

47. Ungar, L.H. and R.A. Brown, *Cellular Interface Morphologies in Directional Solidification. II. The Effect of Grain Boundary Grooves*. Physical Review B, 1984. **30**(7): p. 3993-3999.

48. Ungar, L.H., M.J. Bennett, and R.A. Brown, *Cellular interface morphologies in directional solidification. III The effects of heat transfer and solid diffusivity*. Phys. Rev. B, 1985. **31**(9): p. 5923 - 5930.

49. Ungar, L.H. and R.A. Brown, *Cellular interface morphologies in driectional solidification. IV The formation of deep cells*. Phys. Rev. B, 1985. **31**(9): p. 5931 - 5940.

50. McCartney, D.G. and J.D. Hunt, *A Numerical Finite Difference Model of Steady State Cellular and Dendritic Growth*. Metallurgical Transactions, 1984. **15A**: p. 983-994.

51. Hunt, J.D. and D.G. McCartney, *Numerical Finite Difference Model for Steady State Array Growth*. Applied Scientific Research, 1987. **44**: p. 9-26.

52. Hunt, J.D. and D.G. McCartney, *Numerical Finite Difference Model for Steady State Cellular Array Growth*. Acta Metallurgica, 1987. **35**(1): p. 89-99.

53. Hunt, J.D. *Numerical Finite Difference model for Steady State Array Growth*. in *Solidification Processing 1987*. 1987. Sheffield: The Institute of Metals, London.

54. Bower, T.F., H.D. Brody, and M.C. Flemings, *Measurements of Solute Distribution in Dendritic Solidification*. Transactions of the Metallurgical Society of A.I.M.E., 1966. **236**(5): p. 624-634.

55. Kurz, W. and D.J. Fisher, *Fundamentals of Solidification*. 3 rd ed. 1989, Switzerland: Trans Tech Publications. 63 - 92.

56. Esaka, H. and W. Kurz, *Modelling of Columnar Dendrite Growth*. Zeitschrift für Metallkunde, 1985. **76**(2): p. 127-133.

57. Burden, M.H. and J.D. Hunt, *Cellular and Dendritic Growth. I*. Journal of Crystal Growth, 1974. **22**: p. 99-108.

58. Burden, M.H. and J.D. Hunt, *Cellular and Dendritic Growth. II*. Journal of Crystal Growth, 1974. **22**: p. 109-116.

59. Miyata, Y., T. Suzuki, and J.-I. Uno, *Cellular and Dendritic Growth: Part I. Experiment*. Metallurgical Transactions, 1985. **16A**: p. 1799-1805.

60. Scheil, E., *Bemerkungen zur Schichtkristallbildung*. Zeitschrift für Metallkunde, 1942. **34**: p. 70.

61. Pfann, W.G., *Principles of Zone-Melting*. Transactions of TMS-AIME, 1958. **194**: p. 747.

62. Gulliver, G.H., *Metallic Alloys*. 1922, London: Charles Griffin & Co., Ltd. (Appendix).

63. Flemings, M.C. and G.E. Nereo, *Macrosegregation: Part I*. Transactions of the Metallurgical Society of AIME, 1967. **239**(September): p. 1449-1461.

64. Flemings, M.C., R. Mehrabian, and G.E. Nereo, *Macrosegregation: Part II*. Transactions of the Metallurgical Society of AIME, 1968. **242**(January): p. 41-55.

65. Brody, H.D. and M.C. Flemings, *Solute Redistribution in Dendritic Solidification*. Transactions of the Metallurgical Society of A.I.M.E., 1966. **236**(5): p. 615 - 624.

66. Roósz, A., E. Halder, and H.E. Exner, *Numerical Analysis of Solid and Liquid Diffusion in Microsegregation of Binary Alloys*. Materials Science and Technology, 1985. **1**(12): p. 1057-1062.

67. Roósz, A., Z. Gácshi, and E.G. Fuchs, *Solute Redistribution During Solidification and Homogenization of Binary Solid Solutions*. Acta Metallurgica, 1984. **32**(11): p. 1745-1754.

68. Kirkwood, D.H. and D.J. Evans. *Calculations on Microsegregation in Binary Alloys*. in *The Solidification of Metals*. 1967. London: The Iron and Steel Institute.

69. Clyne, T.W. and W. Kurz, *Solute Redistribution During Solidification with Rapid Solid State Diffusion*. Metallurgical Transactions, 1981. **12A**: p. 965-71.

70. Kirkwood, D.H., *Microsegregation*. Materials Science and Engineering, 1984. **65**: p. 101-109.

71. Kobayashi, S., *Solute Redistribution During Solidification with Diffusion in Solid Phase: A Theoretical Analysis*. Journal of Crystal Growth, 1988. **88**: p. 97-106.

72. Yeum, K.S., V. Laxmanan, and D.R. Poirier, *Efficient Estimation of Diffusion during Dendritic Solidification*. Metallurgical Transactions, 1989. **20**(12): p. 2847-2856.

73. Ogilivy, A.J.W. and D.H. Kirkwood, *A Model for the Numerical Computation of Microsegregation in Alloys*. Applied Scientific Research, 1987. **44**: p. 43-49.

74. Mortensen, A., J.A. Cornie, and M.C. Flemings, *Columnar Dendritic Solidification in a Metal-Matrix Composite.* Metallurgical Transactions, 1988. **19A**: p. 709-721.

75. Mortensen, A. *Solidification of Reinforced Metals.* in *Solidification of Metal Matrix Composites.* 1990. Indianapolis, IN: The Minerals, Metals & Materials Society.

76. Mortensen, A. and I. Jin, *Solidification Processing of Metal Matrix Composites.* International Materials Reviews, 1991. : p. in print.

77. Sekhar, J.A. and R. Trivedi, *Development of Solidification Microstructures in the Presence of Fibers or Channels of Finite Width.* Materials Science and Engineering, 1989. **A114**: p. 133-146.

78. Trivedi, R., S.H. Han, and J.A. Sekhar. *Microstructural Development in Interfiber Regions of Directionally Solidified Composites.* in *Solidification of Metal-Matrix Composites.* 1989. Indianapolis: TMS-AIME, Warrendale, PA.

79. Fabietti, L.M. and J.A. Sekhar. *Mushy Zone Morphologies Observed During Directional Growth of Composite Materials.* in *Nature and Properties of Semi-Solid Materials.* 1992. San Diego, CA: TMS.

80. Shangguan, D. and J.D. Hunt, *In situ Observation of nonfaceted Cellular Growth in a Narrow Channel.* Metallurgical Transactions, 1991. **22A**(7): p. 1683-1687.

81. Gungor, M.N., J.A. Cornie, and M.C. Flemings. *The Response of Microctructures of Metal Matrix Composites to Solidification Time.* in *Interfaces in Metal Matrix Composites.* 1986. New Orleans: T.M.S., Warrendale, PA.

82. Gungor, M.N., *Solidification Processing of Al-4.5%Cu / Al_2O_3 Composites.* 1986, Department of Materials Science and Engineering, Massachusetts Institute of Technology.:

83. Gungor, M.N., J.A. Cornie, and M.C.Flemings. *Solidification Processing of an Aluminum/Alumina Composite.* in *Cast Reinforced Metal Composites.* 1988. Chicago, Illinois: ASM International, Materials Park, OH.

84. Li, Q.F., D.G. McCartney, and A.M. Walker, *Development of Solidification Microstructures in a Fibre Reinforced Alloy.* Journal of Materials Science, 1991. **26**: p. 3565-3574.

85. Gündüz, M. and J.D. Hunt, *The Measurement of Solid-Liquid Surface Energies in the Al-Cu, Al-Si and Pb-Sn Systems*. Acta Metallurgica, 1985. **33**(9): p. 1651-1672.

86. Isaacs, J.A., F. Taricco, V.J. Michaud, and A. Mortensen, *Chemical Stability of Zirconia-Stabilized Alumina Fibers During Pressure Infiltration by Aluminum*. Metallurgical Transactions, 1991. **22A**: p. 2855-2862.

87. Flemings, M.C., *Solidification Processing*. 1974, New York: McGraw-Hill. p 38.

88. Mortensen, A., *Solidification of Al-4.5wt%Cu in the Presence of SiC Fibers*. 1986, Department of Materials Science and Engineering, Massachusetts Institute of Technology.:

89. Underwood, E.E., *Quantitative Stereology*. 1st ed. Metallurgy and Materials, ed. M. Cohen. 1970, Reading., MA: Addison-Wesley Publishing Company. 274.

90. Mortensen, A., M.N. Gungor, J.A. Cornie, and M.C. Flemings, *Alloy Microstructures in Cast Metal Matrix Composites*. Journal of Metals, 1986. **38**(3): p. 30-35.

91. Michaud, V.J. and A. Mortensen, *Infiltration of Fiber Preforms by a Binary Alloy. Part II: Further theory and Experiments*. Metallurgical Transactions A, 1991. **submitted**.

92. Kurz, W. and D.J. Fisher, *Fundamentals of Solidification*. 3 rd ed. 1989, Switzerland: Trans Tech Publications. 204 - 207.

93. Murphy, J.B., *Interdiffusion in Dilute Aluminum-Copper Solid Solutions*. Acta Metallurgica, 1961. **9**: p. 563-569.

94. Cahoon, J.R., *The Use of Phase Boundary Motion to Determine Interdiffusion Coefficients*. Metallurgical Transactions, 1972. **3**: p. 1324-1326.

95. Anand, M.S., S.P. Murarka, and R.P. Agarwala, *Diffusion of Copper in Nickel and Aluminum*. Journal of Applied Physics, 1965. **36**(12): p. 3860-3862.

96. Watson, M.P. and J.D. Hunt, *The Measurement of Liquid Diffusion Coefficients in the Al - Cu System Using Temperature Gradient Zone Melting*. Metallurgical Transactions, 1977. **8A**: p. 1793.

97. Ejima, T., T. Yamamura, N. Uchida, Y. Matsuzaki, and M. Nikaido, Journal of the Japan Institute of Metals, 1980. 44: p. 316-323.

98. Sergeev, S.V., Physicochemical Properties of Liquid Metals, 1952. Oborongiz: p. 53, 83.

99. Mondolfo, L.F., *Aluminum Alloys: Structure and Properties.* 1st ed. 1976, London: Butterworths. 971.

100. Brandes, E.A., ed. *Smithells Metals Reference Book.* Sixth ed. 1983, Butterworths: London.

101. *Metals Handbook.* 8th ed. 1948, Metals Park, OH.: American Society for Metals.

102. Crank, J., *The Mathematics of Diffusion.* 2nd ed. 1975, New York: Oxford University Press.

103. Smith, G.D., *Numerical Solutions of Partial Differential Equations.* 1965, London: Oxford University Press. 179.

104. Froberg, C.-E., *Numerical Mathematics: Theory and Computer Applications.* 1st ed. 1985, Reading: Addison-Wesley Publishing Company.

105. Press, W.H., B.P. Flannery, S.A. Teukolsky, and W.T. Vetterling, *Numerical Recipes: The Art of Scientific Computing (Fortran version).* 1989, New York: Cambridge University Press. 702.